12-2010

Measurement system for high pressure characterizations of materials

Matthew K. Jacobsen
University of Nevada, Las Vegas

MEASUREMENT SYSTEM FOR HIGH PRESSURE CHARACTERIZATIONS OF MATERIALS

by

Matthew K. Jacobsen

Bachelor of Science
Oregon State University
2004

Masters of Science
University of Nevada, Las Vegas
2007

A thesis submitted in partial fulfillment
of the requirements for the

Doctor of Philosophy Degree in Physics
Department of Physics and Astronomy
College of Sciences

Graduate College
University of Nevada, Las Vegas
December 2010

UNIVERSITY OF NEVADA LAS VEGAS

THE GRADUATE COLLEGE

We recommend the dissertation prepared under our supervision by

Matthew K. Jacobsen

entitled

Measurement System for High Pressure Characterizations of Materials

be accepted in partial fulfillment of the requirements for the degree of

Doctor of Philosophy in Physics
Physics and Astronomy

Andrew Cornelius, Committee Chair

Lon Spight, Committee Member

Tao Pang, Committee Member

Clemens Heske, Graduate Faculty Representative

Ronald Smith, Ph. D., Vice President for Research and Graduate Studies
and Dean of the Graduate College

December 2010

ABSTRACT

MEASUREMENT SYSTEM FOR HIGH PRESSURE CHARACTERIZATIONS OF MATERIALS

by

Matthew K. Jacobsen

Dr. Andrew Cornelius, Examination Committee Chair
Associate Professor of Physics and Astronomy
University of Nevada, Las Vegas

Thermoelectric materials have long been investigated for possible use as power sources. This application was recently put to use in the Voyager space program, powering the deep space probes. Despite the usefulness of these materials, the use of pressure to investigate the material properties has only recently become interesting. As such, the work in this document was to developing a system for concurrently measuring the necessary properties. This system is capable of measuring the electrical resistivity, thermal conductivity, and Seebeck coefficient in the pressure range from 0 - 10 GPa. The results for zinc, almandine garnet, and nickel are presented and demonstrate the capabilities of the system. In addition, results are presented for selected established (Bi_2Te_3, $Sb2Te_3$, $BiSbTe_3$) and potential (GaTe, InTe, and $InGaTe_2$) thermoelectric materials. The measurements have been made with pressure up to 10 GPa (transport properties, except heat capacity) or 20 GPa (structure). From these measured properties, it is possible to evaluate how pressure effects the interactions.

ACKNOWLEDGMENTS

I would like to acknowledge the assistance and support of the following in this project:

1. Dr. Andrew Cornelius, for putting up with my repeated questions and for advice on many things.

2. Dr. Ravhi Kumar and the members of Dr. Cornelius's lab, for their assistance.

3. Dr. Lon Spight, Dr. Tao Pang, and Dr. Clemens Heske, my committee.

4. Amadeo Sanchez, James Norton, and Bill O'Donnell, for their wonderful technical toys.

5. The staff of HPCAT at Argonne National Laboratory, for their assistance in the x-ray experiments.

Acknowledged Funding and Support Agencies:

Work at UNLV is supported by DOE Cooperative Agreement DE-FC52-06NA27684. Portions of this work were performed at the High Pressure Collaborative Access Team (HPCAT, Sector 16), Advanced Photon Source (APS), Argonne National Laboratory. HPCAT is a collaboration among the UNLV High Pressure Science and Engineering Center, the Geophysical Laboratory of the Carnegie Institution of Washington, Lawrence Livermore National Laboratory, and the Carnegie/DOE Alliance Center. HPCAT is supported by DOE-BES, DOE-NNSA, NSF, and the W.M. Keck Foundation. Use of the Advanced Photon Source at Argonne National Laboratory was supported by the U. S. Department of Energy, Office of Science, Office of Basic Energy Sciences, under Contract No. DE-AC02-06CH11357.

TABLE OF CONTENTS

LIST OF FIGURES

LIST OF TABLES

CHAPTER 1

INTRODUCTION

For the better part of the past 200 years, there have been studies into the unique properties of materials capable of converting energy to heat. As one will find in any of the works on this type of material, the research on this topic is in the improvement of the conversion efficiency of these materials. However, thermoelectric materials have many factors important to the properties that govern this conversion efficiency. The fundamental parameter of interest for studies of these materials is the thermoelectric figure of merit, represented by Z, or the dimensionless figure of merit, represented by Z T, with T being the temperature in Kelvin. This parameter is defined as

$$ZT = \frac{\alpha^2 \sigma T}{\lambda} \tag{1.1}$$

with α being the Seebeck coefficient of the material, and σ and λ being the electrical and thermal conductivities, respectively.

Upon inspection of the previous equation, it can be determined that the best case for the Z T parameter is to have a minimum thermal conductivity and a maximum electrical conductivity and Seebeck coefficient. The simplicity of this statement belies the inherent difficulty in actually optimizing a material to an effective level for Z T (typically between 2-3 or higher). This is due to the interdependence of all three properties. As an example of this, metallic substances are characterized by electron domination of the transport properties. The electrical conductivity is directly affected by changes in electron density and mobility, whereas the thermal conductivity is also strongly dependent on the concentration of electrons present, as they conduct the majority of the heat through the material. The net result is that an improvement in the electron concentration or mobility would also increase the thermal conductivity through the sample, making the effort itself a rather moot

point. In addition to this, the Seebeck coefficient, which is a measure of the ability ot support an internal electric field, depends on the material's ability to separate charge. If the electrical conductivity increases, the magnitude of the Seebeck coefficient decreases.

The first real attempt at a theory regarding the transport properties of metals was made by P. Drude in the early 1900's. It considers the system as a grouping of ions (with core electrons) that have given up their outermost electrons to form a conduction electron gas inside the material. Further, the ions and electrons are considered to be solid spheres (ions are considered stationary), in the classical sense, that are allowed to undergo brief collisions with each other, but cannot interact other than that. As such, there are no forces acting on either the ions or the electrons unless a collisional process is underway. In this manner, Drude created a simplified solid that has the desired macroscopic property of being electrially neutral, while allowing for the possibility of electrical conduction through the system.

Although the theory regarding transport properties has come further than the initial attempt by Drude in the early 1900's, the theory's basic tennants have remained in place. The classical theory developed in an attempt to describe the electrical resistance properties of materials was the first to consider a material as a grouping of bound ions with a cloud of free electrons around it. This picture has since been disregarded, as the interactions involved are far more complicated than this simple picture could ever have described, the ideas it started with have been modified to create the theories currently used to describe the transport phenomena of materials. In conjunction with this, the development of new ways of investigating the properties of materials has been consistently under development during much of the same time period.

The most common method of investigating properties of materials has and still remains to be chemical substitution. However, there are new methods that can

help to better understand how transport phenomena evolve in a system as the physical properties change. A few of these include the use of nanocrystallites, pressure induced structural changes, and pressure induced non-structural changes. It is well known that the properties of a bulk material differ, in many cases strongly, from the properties of the corresponding nanocrystal material [9]. In addition to this, several groups have turned to the use of pressure to test different structures of certain elements[10]. The application of pressure causing a phase transition has been reported to improve the thermoelectric performance of many materials. Beyond just structural transitions, there are reports dealing with topological transitions ([11], [12]) in materials, as will be dicussed in Chapter 3. Based upon this, the use of pressure to study thermoelectric materials could result in the discovery of new, more useful materials.

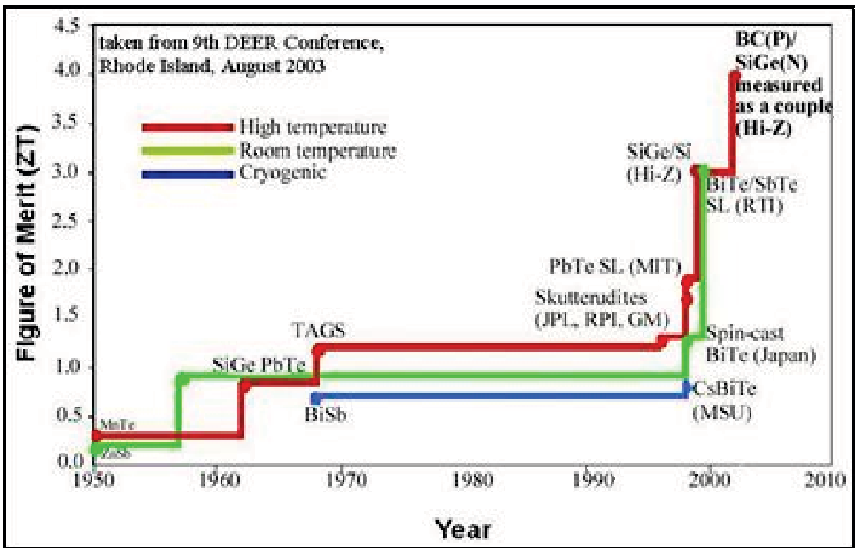

Figure 1 Improvement of maximal ZT value versus time [1]

Despite this, the improvement of the properties of thermoelectric materials have steadily progressed over the last fifty years or so, as is shown in Figure 1,

with a rapid increase in the last decade. The investigations performed on thermoelectrics have ranged from general sample studies under ambient conditions ([13],[14]) to the more comprehensive studies at varying conditions [15]. It is these investigations, coupled with the lack of a comprehensive theory regarding these properties, which makes studies of these materials interesting.

In this document, it is assumed that the reader has a general knowledge of transport phenomena and solid state physics, as reference to ideas and concepts from these areas will be referred to without detailed presentation of the ideas. The rest of the document is organized as follows: Chapters 2-4 will deal with discussions of the background theory regarding transport properties. Following this, Chapters 5 and 6 will deal with the experimental setup, process, and data analysis procedures, along with calibration results. Chapters 7-12 will present sample results. Finally, Chapter 13 will draw some conclusions on the system operation and on the data collected for the samples.

CHAPTER 2

THERMAL CONDUCTION IN MATERIALS

This chapter will deal with the thermal conduction properties of materials, with specific focus on the ability to conduct heat. The important parameters will be defined and the kinetics presented for the primary carriers. Emphasis will be placed on results that are important to this work.

Thermal Conductivity

The essential parameter for determining a materials ability to conduct heat is the thermal conductivity, defined as

$$\lambda = \frac{1}{3} C_v \overline{\nu} l \tag{2.1}$$

and is determined by the heat capacity (C_v), the mean velocity of the energy carrier ($\overline{\nu}$), and the mean free path of that carrier (l). For solid materials, it is well understood that the energy carriers for the system are comprised of electrons and phonons. As the system can be described through these carriers, it is possible to separate the components of the thermal conductivity and write

$$\lambda = \lambda_e + \lambda_p + \lambda_{other} \tag{2.2}$$

with the subscripts referring to the electrons, phonons, and other contributions (defects, boundaries, impurities) that are usually small temperature independent contributions and are generally ignored.

Anharmonic Effects

The introductory theory of the crystalline lattice, as presented in Kittel [16] and Ashcroft [17], is incredibly useful as a starting point. However, it is based on two

assumptions, one of which is a source of problems. In the model perfect crystal, the potential used to describe the interatomic interactions is assumed to be harmonic. If this were true of a real crystal, it would be unable to expand with temperature or to impede the flow of a heat current through the lattice. This assumption results in an infinite relaxation time, as the carriers never interact, resulting in an infinite thermal conductivity.

To remedy this, it is necessary to modify the interatomic potential to become

$$U_{int-atm} = U_0 + U_{harm} + U_{anharm} \tag{2.3}$$

with the first two terms being the usual harmonic approximation. From this formalism, it becomes possible for the energy carriers to interact, limiting the value of the thermal conductivity.

One of the immediate consequences of such a change is in the heat capacity. Since the system is now capable of altering its shape through expansion, it is reasonable to presume that this will have an effect of the Debye temperature of the system. From derivations in several texts ([17],[16]), the rate of change of the Debye temperature with volume is defined as the Gruneisen parameter, represented as

$$\gamma = -\frac{\partial ln(\theta_d)}{\partial ln(V)} \tag{2.4}$$

and can be used to computer the volumetric thermal expansion coefficient as

$$\beta = \frac{\gamma C_v}{3B_0} \tag{2.5}$$

where B_0 is the isothermal bulk modulus. A typical value for the Gruneisen parameter for phonons is 1.

Although the system is now allowed to be anharmonic, it is still subject to the

conservation rules regarding momentum for the phonons, electrons, or interactions between the two. In the case of a crystal, this is referred to as the conservation of crystal momentum and is described by

$$k - k^{'} \pm q = G \tag{2.6}$$

with k, k$^{'}$, and q being wavevectors of the lattice. The initial and final state of the system are represented by k and k$^{'}$, with q being the momentum absorbed or released through the interaction. G is a reciprocal lattice vector that can take on any interger value. It is this G that distinguishes the types of interactions that can occur in materials. If G is zero, the interaction process is a normal or N process. In this case, all of the energy of the interaction returns to the system. If G is non-zero, the interaction is a Umklapp or U process. In this case, a portion of the energy, equivalent to the value of G, is used by the interaction to move the resulting wavevector to a new Brillouin zone of the material.

When talking about the temperature dependence of a property, it is the distiction between these processes that help to explain what occus. N processes, for example, are all lower energy processes and can be expected to be present at all temperatures, but will likely only dominate in lower temperature regimes. U processes, on the other hand, are going to require a certain amount of thermal energy to occur. The higher the value of G, the higher the thermal energy required, suggesting that these processes will become dominant in the system as the temperature is raised. These processes are described in several texts ([18], [19], [20], [2]) and produce forms for the transport phenomena in the different temperature regimes. The discussion of the theoretical predictions for transport properties will be divided into these different temperature regimes and also by the electrical class of the material (i.e. Insulator, Semiconductor, Metal, Semimetal), where there is an existing theory.

Electrical Insulators (Phonon-Phonon Interactions)

For an electronic insulator, the dominant carrier is the lattice, so the phonon contribution to the thermal conductivity should be the primary component. As such, interactions between phonons will determine the mean free path for the system. At low temperatures, the N processes will dominate, except these processes don't result in any significant scattering of phonons. So, the low temperature limit is dominated by boundary scattering, which is proportional to T^3 [2]. As the temperature is raised, the U processes begin to affect the system. In this regime, it was derived, by Leibfried and Scholmann, as mentioned in Ziman [2], that the thermal conductivity would take the form

$$\lambda_p = a(\frac{T}{\theta_d})^n e^{\frac{\theta_d}{bT}} \tag{2.7}$$

with constants a, b, and n determined from measurements.

As the temperature is moved into the high temperature regime, the distinction between the processes becomes unimportant, due to the limiting behavior of the phonon occupation number, which goes as

$$n_s = \frac{1}{e^{\frac{\hbar\omega_s}{k_b T}} - 1} \approx \frac{k_b T}{\hbar\omega_s} \tag{2.8}$$

for state s with frequency ω_s. From this, it is seen that the number of phonons present is expected to increase linearly with temperature. This suggests that the interations become more frequent, leading to a reduction in the heat flow. Thus, the thermal conductivity in this regime would decrease inversely as T ($\lambda_p \propto T^{-x}$). It has been shown by Ziman [2] that the power for this proportionality is one. Further, he mentions other work from Leibfried and Scholmann regarding the high temperature form for the thermal conductivity with a more specific result. Their work derived that

$$\lambda_p \propto \frac{D\overline{\nu}^3 a}{\gamma^2 T} \tag{2.9}$$

for an insulating material of density D, lattice spacing a, and average sound velocity $\overline{\nu}$.

Electronic Conduction in Insulators (Electron-Phonon Interactions)

Although the discussion has dealt with only the interaction between phonons, it is also possible for the phonon spectrum to interact with the electron spectrum. In electric insulators, this contribution is usually small, but should be considered regardless. It can be shown that the electronic contribution at low temperature is proportional to T, with the absolute form being related to the low temperature heat capacity. In the high temperature limit, the result is, as presented in Ziman [2]

$$\lambda_e = \frac{2.5\overline{\nu}^3 Da}{\theta_d} \tag{2.10}$$

with the parameters as previously defined. The value for this can easily be calculated and results in a value nearly one tenth of the intraphonon processes. This demonstrates clearly that, for insulating materials, phononic conduction is the primary source of heat transfer across the sample.

Electrical Conductors (Electron-Defect Interactions)

In contrast to the electronic component for insulators, metals show the dominant presence of electronic conduction. The derivation of the Drude model results in an equation relating the electronic heat conduction to the electronic charge conduction as

$$L_0 = \frac{\lambda_e}{\sigma T} \tag{2.11}$$

with σ being the electrical conductivity and L_0 being the Lorentz number. In this form, the Lorentz number is a constant defined as $L_0 = \frac{\pi^2 k_b^2}{3e^2}$, with e being the fundamental charge. It should be noted that, for Drude's theory, the derivation of this constant relation was made under the high temperature assumption and is only true in that limit.

Of interest, phonons do affect and interact with the electrons, but do not change the form of 2.11 at all. This is because the heat conducted by the electrons will rise in direct proportion to the increase in phonons in the system. As such, the system's state remains balanced, resulting in 2.11 remaining a valid description of the system.

In the low temperature regime, a form for the electronic contribution is derived by Ziman [2], with the form

$$\lambda_e = \frac{T}{A + BT^3} \tag{2.12}$$

with A and B being constants. In particular, the B constant is determined from lattice interactions and is suggested to have the form

$$B = \frac{12 J_5(\infty) R^2 \rho_\theta}{\pi^2 Q^2 L_0 \theta_d^3} \tag{2.13}$$

with R, Q, and ρ_θ being constants and $J_5(\infty)$ being the fifth order Bessel function. This complicated form should be recognized as merely a qualitative representation that works well.

Semiconductors

A form similar to 2.11 can be derived for semiconductors and semimetals under the assumption that the Fermi energy is in the energy gap between bands and not near either edge. For one type of carrier (either electrons or holes), this can be

found, as done by Goldsmid and Nolas [18], to result in

$$L = (\frac{k_b}{e})^2(r + 5/2) \tag{2.14}$$

with r representing the power of the energy that the relaxation time is dependent on. This form is only true in the non-degenerate approximation for the carriers, resulting in a semiconductor. The previous form of 2.11 is again the result if the degenerate solution is derived, suggesting that the semimetals can be expected to display more metallic like behavior.

If the system is allowed to conduct both types of carrier, the situation becomes more complicated. A derivation of this is shown in [18]. This results in

$$\lambda_e = \lambda_{e,1} + \lambda_{e,2} + \frac{\sigma_1\sigma_2}{\sigma_1 + \sigma_2}(\alpha_2 - \alpha_1)^2 T \tag{2.15}$$

with the subscripts relating to the carrier. As this shows, allowing the presence of both of the electrical carriers makes the thermal conductivity dependent on both of the other two transport properties discussed in this work.

High Pressure Effects

Electronic Component

To describe what is theoretically predicted to happen to the thermal conductivity with regards to changes in the system volume, it is useful again to consider a separated system. So, for the electronic component of the thermal conductivity, 2.11 can be used to determine the pressure dependence of the system. This can be done as

$$\frac{\partial ln(\lambda_e)}{\partial ln(V)} = \begin{cases} -2\gamma & T > \theta_d \\ 6\gamma & T < \theta_d \end{cases} \tag{2.16}$$

if the assumptions of Ziman [2], as described in his text, are used. If Lawson's [21] theory is used instead, this derivative can be expected to be

$$\frac{\partial ln(\lambda_e)}{\partial ln(V)} = -(2 + (\frac{\theta_d}{T})^2\gamma) \begin{cases} -4/3\gamma & T > \theta_d \\ 2/3\gamma & T < \theta_d \end{cases} \tag{2.17}$$

with the parameters as previously defined.

Lattice Component

For the lattice component, there are several models used. The theoretical basis of the forms presented here is contained in Hofmeister's [22] paper. The starting point for all of the models is the equation

$$\lambda_p = \frac{\rho}{3ZM} \sum_{j=1}^{3} \sum_{i=1} 3NZc_{ij}u_{ij}^2\tau_i \tag{2.18}$$

with c_{ij} being the Einstein heat capacity, u_{ij} being the group velocity, τ_i being the mean free lifetime, Z being the number of formula units per unit cell, N being the number of atoms, and M being the molar formula weight. From this starting point, four models (Acoustic, Dimensional Analysis, Bulk Sound, and Optic) have been developed. The main difference between these models being the treatment of the mean free lifetime.

For the Acoustic and Dimensional Analysis models, this lifetime was assumed to go with an inverse T relationship, when above the Debye temperature. This assumption yields a form of

$$\lambda_p = \frac{B}{T} \tag{2.19}$$

with B being a constant (that may be volume dependent). In the acoustic model, Julien, presented in [22], derived B to have the form

$$B = \frac{24}{20}\frac{4^{1/3}}{\gamma^2}(\frac{k_b\theta_d}{h})^3 ZMa \tag{2.20}$$

with h being the Planck constant and everything else as previously defined. Roufosse and Klemens [23] also arrived at a similar form as this, but with $1/7$ the value of B.

From the Dimensional Analysis model, Dugdale and MacDonald [24] arrived at

$$\lambda_p = \frac{VK_Tua}{3\gamma^2 T} \tag{2.21}$$

with K_T being the isothermal compressibility. In this form, it was assumed the unit cell is cubic. From both models, Hofmeister derives a pressure effect of,

$$\frac{\partial ln(\lambda_p)}{\partial P} \approx \frac{6}{K_T}. \tag{2.22}$$

The remaining two models, both derived by Hofmeister in various papers ([25],[22]), result in nearly identical pressure effects with the numercial value changing from six to four. Unfortunantely, no discussion is given regarding low temperature forms for the pressure dependence. It is possible to derive a form for the low temperature expectations using the intermediate temperature equation in equation 2.7[2]. If this is done, the result is

$$\frac{\partial ln(\lambda_p)}{\partial ln(V)} = \frac{\partial ln(\lambda_p)}{\partial ln(\theta_d)}\frac{\partial ln(\theta_d)}{\partial ln(V)} = (\frac{\theta_d}{bT} - n)\gamma \tag{2.23}$$

with the parameters as previously defined.

CHAPTER 3

ELECTRICAL CONDUCTION IN MATERIALS

As was discussed in the previous chapter, the study of transport properties of materials requires additional terms for the interatomic potential to be included. This is particularly true for electron transport, as the first picture one might consider is an electron passing through a lattice, with static lattice points. Similar to the phonons, this picture results in a system with no electrical resistance whatsoever. As such, this chapter will present the consequences of the anharmonic contribution to the electrical resistance.

Electronic Conduction in Metals

Lattice Resistivity (Electron-Phonon Interactions)

In conjunction with the thermal conductivity, allowing interactions between the lattice and the electrons creates a component of the overall resistance due to the lattice. Further, as this interaction can be expected to depend strongly on the temperature, it is important to gain an understading of this contribution. This discussion is easiest to begin in the high temperature regime, where the quantization of the phonons is unimportant.

In this limit, the scattering of electrons by phonons should be related to the amplitude of the thermal vibration of the atoms. Thus, it should be expected that the lattice contribution to the resistivity should behave as

$$\rho_p \propto T \tag{3.1}$$

with ρ_p being the lattice resistivity. If the system is considered to be in the low temperature limit, the situation becomes considerably more complicated. This is due to the quantization of the phonon states, which plays a much larger part as

the temperature is lowered. This coupled with the lower energy of the phonons present, would result in only small angle scattering occuring in the system.

From classical scattering theory, it is possible to show, as done by Ziman [2], that the scattering angle will exhibit a squared dependence on temperature. This, coupled with the cubic dependence from the Debye model, results in a low temperature limit expected to be proportional to the fifth power of the temeprature. As such, the temperature dependences of this contribution can be presented as

$$\rho_p = \begin{cases} 4(\frac{T}{\theta_d})^5 D_5(\theta_d/T)\rho_\theta & T < \theta_d \\ \frac{T}{\theta_d}\rho_\theta & T > \theta_d \end{cases} \tag{3.2}$$

with ρ_θ being a temperature independent constant and the D function being a Debye integral defined by

$$D_n(x) = \int_0^x \frac{z^n e^z}{(e^z - 1)^2} dz. \tag{3.3}$$

With a typical Debye integral, the x would be the Debye temperature parameter divided by the sample temperature, and the z parameter is proportional to the sample temperature, as can be seen in Kittel [16].

Electron-Electron Interactions

It is also reasonble to expect that the electrons in the system could interact with each other. This possible interation is specifically addressed by Ziman, with the derivation details presented in section 9.14 of his text [2]. The derivation results in a form for this contribution of

$$\rho_{ee} \approx \frac{\pi^2 z' e^2 G^2 g R (k_b T)^2}{32 v_f E_f^2 q^2} \tag{3.4}$$

with G being an interference factor and g, R, and q being constants.

Despite the compactness of the results, Ziman mentions that no effect has ever been observed for resistance with a squared power dependence of temperature. This suggests that this contribution is either much smaller in magnitude that reasonable values for the parameters would suggest or that this effect is non-existent. Either result allows this effect to be disregarded.

Electronic Conduction in Semiconductors

The electrical conduction properties of semimaterials are slightly more complicated that those of metals due to the presence of holes and the far smaller concentrations of free electrons present in them. As a result of the addition of another carier, it is necessary to modify the initial equation governing the conduction of electrons to include holes. As a result, the equation for the conductivity of a semiconductor is

$$\sigma = n_h e \mu_h + n_e e \mu_e \tag{3.5}$$

where the n's are the carrier concentrations and the μ's are the mobility of that carrier. As the carriers can have different masses and collision times, the mobility factor is different for each of the carriers. It is futher metioned by Ziman [2] that the collision/relaxation time is proportional to some power of the energy ($\tau \propto E^{\chi}$), which makes the mobility dependent on the same power of T. Thus, the general expectations of a semiconductor system can be written as

$$\sigma \propto (T^{\chi_e} + T^{\chi_h}). \tag{3.6}$$

Lattice Scattering

The lattice scattering component for semiconductors deviates significantly from the previous form from the metals section. This is due to the fact that interactions

in semimaterials can take place in the normal manner, through the acoustic modes of the system. However, they can also take place through the optical modes of the system. This contribution does not show up significantly in metals due to the symmetry of the lattice, as mentioned in the work by Kamal [26]. Dealing with the acoustic contribution first, the mobility can be represented as

$$\mu_{l,acou} = \frac{2^{3/2}\pi D s^2 \hbar^4}{3E_1^2 (m^*)^{5/2}(kT)^{3/2}} \tag{3.7}$$

where E_1 is the deformation potential caused by dilatation of the phonon wave, D is the mass density, and s is the velocity of sound in the solid. As a note, this particular formula, derived in [2], was produced under the assumption of spherical bands. This is not the case in general, for which no analytical solution exists.

The optical modes of the system can contribute to the overall lattice component in two ways, depending on the type of crystal under study. If the crystal is polar in nature (has a natural separation of charge with no field present), then the derivation results in a form for the mobility represented as $\mu = \frac{1}{ne}\sum_{n,n'} J_n (P^{-1})_{n,n'} J_{n'}$, which is horribly complicated and cannot be simplified for a general temperature. As such, at high temperatures, the matrix for the mobility can be simplified to just one element, resulting in a form for polar crystals of

$$\mu_{l,op,p,ht} \approx \frac{3\gamma(\hbar\omega)^2}{\pi^{1/2} 2^{9/2} e (m^*)^{3/2}(kT)^{1/2}}. \tag{3.8}$$

Whereas, at lower temperatures, the mobility becomes

$$\mu_{l,op,p,lt} = A(e^{\hbar\omega/kT} - 1) \tag{3.9}$$

where A is a constant composed of terms invariant under pressure and temperature.

If the crystal structure is covalently bonded, then the derivation becomes more complex. This is due to the fact that there is no way to know the strength of the perturbation potential, so it must be made an adjustable parameter. The derivation is presented in Ziman[2] and results in an approximate high temperature form of

$$\mu_{l,op,cov,ht} \propto \frac{DA}{(kT)^{3/2}} \tag{3.10}$$

The remarkable part of this is that the contribution due to the optical modes will simply add to the acoustic modes in a covalent crystal. As such, the temperature dependence should be the same. As was mentioned earlier, these derivations assume that the system is in the spherical band model, which is most likely untrue in any given sample. However, it is a good first attempt to describe the properties of these materials.

Insulators

In general, textbooks will refer to insulating materials as non-conductive, illustrating the theoretical concept that the insulator is incapable of conducting electrons of its own accord. This is due to the fact that insulators are composed of closed shells (i.e. no free electrons). As such, one would expect an infinite resistivity in these materials regardless of temperature.

This is in contrast with experimental evidence that shows that, although markedly small, there is some electrical conduction through insulating materials. As with both metals and semiconductors, insulating materials will have defects and impurities present. The presence of these alterations can contribute either holes or electrons to the crystalline structure and, as such, are the primary source of electrical conduction in insulating materials. Therefore, one would expect that the temperature dependence of such alterations would be descriptive of the temper-

ature dependence of the electrical resistivity of insulating materials. To describe this, the effects of Mott's rule can be referred to. This presents a T dependence for the impurities present in the structure, as well as a Z^2 dependence for valence difference between the host structure and the impurity. In this case, the host should be neutral, so Z is simply the excess charge of the impurity.

High Pressure

In addition to the temperature effect on electrical conduction, pressure can be expected to alter the resistance of a substance also. For metallic substances, as is shown in Ziman[2], it is possible to derive a form for the resistivity being proportional to e^{θ_d}. So the expected pressure effect is

$$\frac{\partial ln(\rho)}{\partial ln(V)} = \frac{\partial ln(\rho)}{\partial ln(\theta_d)} \frac{\partial ln(\theta_d)}{\partial ln(V)} = \begin{cases} 2\gamma & T > \theta_d \\ -6\gamma & T < \theta_d \end{cases} \tag{3.11}$$

where the numerical contribution comes from the power of θ_d in the resistivity.

This topic is also dealt with by Lawson [21]. In this case, to address the situation by presenting that $R = \frac{qC^2}{\theta_d^2 \alpha^2 k_b^2}$. From this he derives that

$$\frac{\partial ln(R)}{\partial ln(V)} = \frac{\partial ln(R)}{\partial ln(\theta_d)} \frac{\partial ln(\theta_d)}{\partial ln(V)} + 2\frac{\partial ln(C)}{\partial ln(V)} + 2/3 - 2\frac{\partial ln(\alpha)}{\partial ln(V)} \tag{3.12}$$

from which, he avoids Ziman's assumption that the first derivative in the first term is equal to negative two. It was mentioned that, for $\theta_d/T < 4$, this term takes on the value

$$\frac{\partial ln(R)}{\partial ln(\theta_d)} = -(2 + \frac{\theta_d^2}{9T^2}). \tag{3.13}$$

The relation is still used that the volume derivative of the Debye temperature in the first term of equation 3.12 is proportional to the negative of the Gruneisen

parameter. For free electrons, the α term is negligible. This leaves the C term in the previous equation, which is strongly dependent on the model used. The models, used by Lawson [21] and presented in other works also [27], have values for this derivative between negative one and two-thirds, which yields

$$\frac{\partial ln(R)}{\partial ln(V)} = (2 + \frac{\theta_d^2}{9T^2})\gamma \begin{cases} -4/3 & T > \theta_d \\ 2/3 & T < \theta_d \end{cases} \tag{3.14}$$

It should be remembered that this is strictly for normal metals only (Pt, Cu, Ag, Au, etc.). When the discussion moves to less normal metals (Alkali, Alkaline Earth, and Rare Earth) and the semimetals (Bi, Sb), the discussion becomes more speculation than anything else. There exists only cursory attempts to describe the pressure effects of all of these materials, with a complete lack of explanation for the semimetals.

Semiconductors

For semiconducting materials, the property that is most relevant to the change in pressure is the piezoresistance. This property refers to the change of the resistivity with volume change or application of strains/stesses. This discussion can be divided into two categories, intrinsic semiconductors and extrinsic semiconductors. For an intrinsic semiconductor, the fact that all of the carriers are constituents of the material itself makes the change only dependent on the energy gap of the material. This can be represented as

$$\frac{d\, ln(\rho)}{d\, ln(V)} \approx \frac{1}{kT}\frac{\partial E_g}{\partial \Delta} \tag{3.15}$$

with E_g being the energy gap and Δ being the volume collapse due to applied pressure. Unfortunately, no predictions can be made regarding the direction or

magnitude of the change in the resistivity, as this depends directly on what happens to the energy gap.

If the material is extrinsic instead of intrinsic (i.e. carriers due to dopants in material), then the pressure dependence of the material's resistivity is directly determined by the minority carriers through the mobility. As is mentioned by Ziman [2], the dialational coefficient of the piezoresistivity tensor in this situation is usually of small magnitude, resulting in a small change in the resistivity with pressure. Thus, the application of hydrostatic, or quasi-hydrostatic, pressure results in a small overall change in the resistivity of extrinsic semiconductors, but the exact magnitude and size of the change depends on the dopant and on the host material composition. An example of this is presented in Table 10.2 of Ziman's text, where he presents data from work by Smith regarding the coefficients of n and p doped silicon and germanium.

Overall, the effect of pressure on an extrinsic semiconductor should be rather similar to that of an insulator. This is due to the fact that the insulating material has no conduction electrons of its own, so they must be provided by a dopant. However, the concentration of such doped electrons should remain rather small and result in a much smaller effect than that present in the extrinsic semiconductor.

Structure Based Electronic Effects

In addition to the general theory pertaining to the different types of electrical conduction, it is possible for the changes due to pressure to indirectly influence the electronic properties of materials. An example of this type of effect is a phenomenon called an Electronic Topological Transition (ETT). This type of transition is not well understood at this point in time, but has become a topic of interest to several research groups around the world ([11], [12], [28], [29]). The current theory on this is that the application of pressure to a material causes a reshaping of the

Fermi surface of the material without changing the physical structure of the crystal. As such, it is different from a pressure induced structure transformation, but is still primarily looked for through structure data. This restructuring is theorized in several papers ([12], [30]) to appear in structure studies of the material, but in a more subtle way.

Normal structure studies would involve the determination of the unit cell parameters and volumes from x-ray measurements. Once this is done, the resulting volumes and pressures, along with the bulk modulus and it's pressure derivative, can be converted to a different type of equation of state, similar to a stress plot with pressure. The method of Garg *et al.* [11] uses equations of state developed by Holzapfel and Vinet to convert to this type of plot, using the equations

$$Vinet : ln(H_0) = ln(B_0) + \eta(1 - X); H_0 = \frac{PX^2}{3(1 - X)}, \eta = \frac{3(B_0^{'} - 1)}{2} \tag{3.16}$$

and

$$Holzapfel : ln(H_0) = ln(B_0) + C_2(1 - X); H_0 = \frac{PX^5}{3(1 - X)}, C_2 = \frac{3(B_0^{'} - 3)}{2} \tag{3.17}$$

with P being pressure, X = $(\frac{V}{V_0})^{1/3}$ being the fractional volume collapse, with the remainder as previously defined. If these plots cannot be fit by a single linear equation for the entire pressure range, it is considered to be evidence of this type of transition occuring the material. As this would constitute a restructuring of the Fermi surface, it is highly likely that the occurance of this type of anomaly would result in more dramatic changes in the electrical related properties of the material.

CHAPTER 4

THERMOELECTRIC PHENOMENA IN MATERIALS

One of the more interesting transport phenomena involves the interplay between the previous two forms of transport. It is this property that is the primary forcus for several studies of thermoelectric materials, as there is a lack of understanding regarding what causes a material to be a good thermoelectric material. This chapter will present the current understanding regarding this phenomena.

Seebeck Effect

The Seebeck effect, discovered in 1821, is a potential difference across the junction of two materials when a thermal gradient is present. The Seebeck coefficent is the proportionality constant between the potential difference and the temperature difference. This results in the governing equation

$$\Delta V = \alpha(T)\Delta T \tag{4.1}$$

with $\alpha(T)$ being the temperature dependent Seebeck coefficient, ΔT being the thermal gradient between the junctions, and ΔV being the potential difference.

Similar to the Peltier coefficient, the Seebeck coefficient can be positive or negative depending on the materials chosen. Also, a Seebeck coefficient can be defined for an individual material but has no real meaning without two or more materials being involved in the process. Similar to the previous effects, the Seebeck effect has a microscopic explanation also. It arises due to the fact that the charge concentration in any given material depends on the temperature. As such, a thermal gradient across the material will result in a gradient in the charge concentration. This produces an electric field in the material and results in a potential difference between its ends. However, to notice the electric field, which is working to balance

the charge separation, there needs to be two materials joined. This junction will provide a method for the charges to nullify the electric field in the center, forcing the charges on the ends of the material to conduct through an external circuit. If one material were used alone, then the charges would recombine quite rapidly, since there is nowhere for them to escape.

Thermopower of Materials

Insulators

As was previously discussed, the thermopower of any given material is defined as the ratio of the potential difference to the temperature gradient across the sample. In this manner it is easy to see that insulators are not expected to be very good thermoelectric materials. This is due to the fact that insulators are remarkably poor electrical conductors, leading to a large potential drop across the sample. In conjuntion with this, they are also poor thermal conductors (with the exception of diamond), resulting in a comparibly large temperature gradient across the sample. From the definition for the thermopower, this would result in small values for the Seebeck coefficient, making these materials ineffective. As there are no adequate presentations regarding the theory of thermopower for insulating materials, the discussion will move to more interesting materials.

Metals

The first attempt at a theory for the Seebeck effect in materials is attributed to Drude's free electron model. From Drude's first step, the leap was made to define the Seebeck coefficient as

$$\alpha = \frac{-\pi^2 k_b^2 T}{3e}\left(\frac{\partial ln(\rho(E))}{\partial E}\right)_{E=E_F} = \frac{\pi^2 k_b^2 T}{3e}\left(\frac{\partial ln(\sigma(E))}{\partial E}\right)_{E=E_F} \tag{4.2}$$

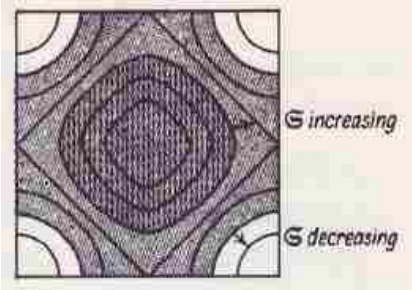

Figure 2 Schematic Diagram of the Fermi surface in the Brillouin zone[2]

with E_F being the Fermi energy of the material. This form is particularly important to general transport theory due to the fact that this is the first time a transport equation has relied on the first power of the electric charge, resulting in an intrinsic sign for the equation. The equation is defined such that the charge is for an electron, making the derivative positive for a negative Seebeck coefficient.

The main problem comes from the fact that taking the derivative is not an easy task. However, as mentioned in Ziman [2], it is possible to rewrite the derivative in a slightly easier to deal with form,

$$\frac{\partial ln(\rho(E))}{\partial E} = \frac{\partial ln(\Lambda)}{\partial E} + \frac{\partial ln(G)}{\partial E}, \tag{4.3}$$

with Λ being the electron mean free path and G being the Fermi surface area of the system. In this equation, the derivative involving the mean free path of a system should be invariably positive due to the fact that electrons with higher energy are less likely to be scattered in short distances, resulting in long mean free paths for the system. The second term, however, presents some trouble as the area of the Fermi surface can either increase or decrease with energy, depending on the energy it is at. As an example, consider the following diagram from Ziman [1].

In Figure 2, it can be seen that, as long as the surface itself is not touching the

[1]Figure reproduced with permission of publisher.

edge of the containing zone, the area will increase. However, the moment that the surface touches the edge of the zone, its area will begin to decrease. As such, the second term in the previous equation can take on either positive or negative values and, possibly, become the dominant term in the equation. This could result in a positive Seebeck coefficient for the material.

The obvious first type of metals to attempt to describe are those that behave like free electron gasses, the alkali metals. In this situation, the Fermi energy is directly proportional to the Fermi surface area. This results in

$$\alpha_F = \frac{\pi^2 k_b^2 T}{3eE_F} \tag{4.4}$$

with E_F being the Fermi energy. With this, it is possible to obtain an order of magnitude for the Seebeck coefficient in this type of system. In this system, the mean free path is large and not highly dependent on energy at all, so the first term in the previous equation is negligible in the overall scheme, making our system only dependent on the energy change of the Fermi surface, which results in the estimate for the Seebeck coefficient of $\alpha_F = -2.45 \times 10^{-2} \frac{T}{E_F} \frac{\mu V}{deg}$. At high temperatures, this results in a Seebeck coefficient predicted to be close to 3 α_F. In general, this describes the magnitude and sign of the alkali metal quite well, with the unexplained exception of Li, which has a positive value. For the noble metals, the situation becomes more interesting, as the Fermi surfaces touch the zone boundary in all of them. This results in a positive Seebeck coefficient for each with values of α/α_F between -1 and -2.

For these cases, it is assumed that the metal under study is of impeccable purity and monovalent. However, if the material is polyvalent, there is no simple form to predict their thermopowers. Despite this, Ziman [2] mentions that divalent metals seem to prefer a positive α, while trivalent metals seem to prefer negative values.

One special subset of materials is the semimetals, consisting of the elements Bi, Sb, Se, and Te. These materials are particularly interesting due to the extraordinarily high values for their Seebeck coefficients. In these materials, the presence of both holes and electrons in the band structure, in conjuntion with the relatively small effective masses and concentrations, is proposed to explain the inordinately high values. For this situation, an effective energy must be introduced, creating a representative form of

$$\alpha = \frac{\pi^2 k_b^2 T}{3eE_{eff}} \frac{m_e - m_h}{m} \tag{4.5}$$

with $E_{eff} = \frac{\hbar^2(3\pi^2 n_e)^{2/3}}{2m}$, n_e being the concentration of electrons in the system, and m being the normal mass of an electron.

Further oddness ensues upon consideration of the transition metals with their d-band contribution. In the case of these metals, the value of the Seebeck coefficient is also large and has a widely variable sign, which is considered to be caused by the scattering of s electrons into the high density of states d-band. If this occurs, an additional term to the mean free path shows up with $\Lambda \propto N_d(E)^{-1}$. This term will contribute to the Seebeck coefficient in the form

$$\frac{-\pi^2 k_b^2 T}{3e}\left(\frac{\partial ln(N_d(E))}{\partial E}\right) \tag{4.6}$$

Low Temperature The theory behind the low temperature trends for the Seebeck coefficient might be expected to be more straight forward than the high temperature results described already. However, due to quantization of the lattice waves, this is far from the case. The results of a theory at low temperature result in the expectation that the thermopower should fall linearly towards zero as the temperature does. This is not the case in even the most simple metallic system. As it turns out there is a peculiar effect that manifests in most systems referred to as phonon drag that prevents this from occuring at low temperatures.

Phonon Drag Phonon drag is physically rather similar to how it sounds. Up to this point, it has been assumed that the transport of heat and flow of electrons would be isolated circumstances. Phonon drag is an effect that requires the relaxation of this assumption. When a system is subjected to a thermal gradient, the result is an obvious flow of heat through the phonon system. In addition, the flow of electrons will frequently trade momentum with the phonons flowing in the system, causing the electrons to be "dragged" along by the phonon spectrum as it propagates.

Unfortunately, the addition of phonon drag to the system modifies all of the transport property equations. However, as is mentioned in Ziman[2], the modification to the thermal conductivity adds nothing of any consequence to the previous formulae. The addition to the resistivity results as

$$\rho = \rho_0 + \rho_L(1 - \frac{P_{1L}^2}{P_{11}P_{LL}}) \tag{4.7}$$

where the P functions are variational functions. As it turns out, if the temperature of the system is the Debye temperature, then the ratio of P's has a value presumed not greater than 0.1, making it rather negliglible in the overall state of things. As the temperature is increased, it becomes less significant to the system.

The main contribution of phonon drag is in the Seebeck coefficient. The addition of phonon drag to this theory results in an additional term from the lattice of the form

$$\alpha_L = \begin{cases} \frac{-kP_{1L}}{3n_a P_{LL}}, & T > \theta_d \\ \frac{-4\pi^4 kT^3 P_{1L}}{5en_a\theta_d P_{LL}}, & T < \theta_d \end{cases} \tag{4.8}$$

with n_a being the number of free electrons per atom. Further, Ziman suggests that

$P_{11} = P_{LL} = -P_{1L}$, so the actual forms for the previous equation become

$$\alpha_L = \begin{cases} \frac{k}{3n_a}, & T > \theta_d \\ \frac{4\pi^4 kT^3}{5en_a\theta_d}, & T < \theta_d \end{cases} \tag{4.9}$$

drastically simplifying the overall form. It is also mentioned, in Ziman's text, that the magnitude for this could be as large as 86 $\frac{\mu V}{deg}$.

Semiconductors

The main change that comes about in moving from metallic systems to semiconductors is the common presence of both holes and electrons in the system. In addition, the magnitude of the thermopower in these systems tends to be several orders of magnitude higher than that for metals. This comes about primarily due to the fact that semiconducting systems are more capable of maintaining a potential difference between the ends of the sample. To begin with, if there is only a single band present (i.e. only one type of electrical carrier), then the system produces a rather simple form for the Seebeck coefficient. This form is

$$\alpha = \frac{1}{eT}[\frac{E_e^2\tau(E_e)}{E_e\tau(E_e)} + \xi_e]. \tag{4.10}$$

At this point, a fair assumption to make would be that $\tau(E) \propto E^\nu$. If this assumption is made, then the previous equation reduces (using properties of the Γ function) to

$$\alpha = \frac{k}{e}[(\nu + 5/2) + \frac{\xi_e}{kT}]. \tag{4.11}$$

If the leading term is considered, the magnitude from this equation is a factor of E_F/kT larger than the value for metals. As Ziman [2] mentions, this puts the energy scale for semiconductors on the order of millivolts, compared with that from

metals (microvolts).

However, this previous form is only true when one type of electrical carrier is present (i.e. extrinsic semiconductor). When both are present, it is necessary to consider both electronic and hole conduction through the sample, resulting in bipolar conduction. In this case, the result is simply a superposition of the previous equation with the equivalent form for the other carrier type. This results in

$$\alpha = \frac{1}{eT}[\frac{\frac{n_e}{m_e}(E_e^2\tau_e(E_e)) - \frac{n_h}{m_h}(E_h^2\tau_h(E_h))}{\frac{n_e}{m_e}(E_e\tau_e(E_e)) - \frac{n_h}{m_h}(E_h\tau_h(E_h))} + \frac{n_e\mu_e E_{F,e} - n_h\mu_h E_{F,h}}{n_e\mu_e + n_h\mu_h}] \tag{4.12}$$

with the n's being the concentrations, μ being the mobility, and E_F being the Fermi energy for electrons (e) and holes (h). One particular consequence of this formula is the explanation of the inversion temperature for intrinsic semiconductor systems. It is a well known phenomenon that with the variation of temperature in these systems, the Seebeck coefficient may start negative and transition to a positive value as the temperature is raised. This turnaround point corresponds to a change in the dominant carrier of the system.

For these systems, there is also a contribution due to phonon drag. As this phenonmenon has already been discussed, the results of the derivation will be presented here. For semiconducting systems, a temperature dependence is also expected on the basis of the system reaching the boundary scattering condition (specimen diameter is D). In this case, the result is

$$\alpha_L \propto \begin{cases} T^{-(9-\nu)/2} & T > \theta_d \\ DT^{3/2} & T < \theta_d \end{cases} \tag{4.13}$$

In the previous case, ν is the power of the energy creating the proportionality to the relaxation time.

Pressure Dependence

For the Seebeck coefficient, it is now possible to obtain some approximate forms for the dependence with volumetric change in the system. First, since there is no real theory decribing the thermopower of insulating systems, there is nothing that can be said regarding these materials. However, there are several forms available for different types of metals. Using the equations presented previously, the pressure/volume dependence of alkali and noble metals (pure) can be expected to take a form where

$$\frac{\partial \alpha}{\partial V} \propto \frac{1}{E_F}\frac{\partial E_F}{\partial V} \propto V^{7/3}. \tag{4.14}$$

Semimetals, on the other hand, are slightly more direct, due to the direct volume dependence in the equation. Inspecting the volume dependence of this equation, it is easy to pick out that

$$\frac{\partial \alpha}{\partial V} \propto V^{-1/3}. \tag{4.15}$$

Although information was mentioned regarding the contribution of d-band effects to the thermopower of transition metals, it is impossible to gain an approximate form for the pressure dependence due to the lack of an analytical form for this contribution. A similar situation presents itself for impurity systems, as it is highly dependent on the materials contributing to this effect. However, there is a rather definite form for the contribution due to phonon drag in the system. At low temperature, this contribution will dominate and will become a linear offset at high temperatures. This form results as

$$\frac{\partial \alpha_L}{\partial V} \propto \begin{cases} Constant & T > \theta_d \\ V & T < \theta_d \end{cases} \tag{4.16}$$

The final piece to consider is the effect pressure would have on semiconducting

system. Due to the complexity of the bipolar form for the thermopower, it is rather difficult to define an analytical form for this situation also. Some insight can be gained by using the single band contribution, which results in

$$\frac{\partial \alpha}{\partial V} \propto V^{-1/3} \tag{4.17}$$

Overall, the discussion presented in this and the previous chapters gives a brief semblence of the complicated theory describing what is currently known regarding the transport properties of materials. This information will become a valuable asset later in determining what factors are of prime importance to the temperature and pressure effects in materials. The next step in discussing the work performed is to present the details regarding the experimental setup and processes for the experiments performed.

CHAPTER 5

EXPERIMENTAL DETAILS AND PROCEDURE

This chapter will deal with the experimental setups used, the measurement theories applied to the resulting data, and the sample preparation techniques for the work presented in this documnt. This begins with the preparation process used to create the samples used for this study, including a description of the process used to check the sample purity. Then, the process used for determining the heat capacity of the various samples will be presented. Following this, the discussion will move to the experimental details regarding the high pressure experiments and how the sample properties are measured.

Sample Preparation

The samples chosen for this work are of the form ATe, with A being (Ga, In, or $Ga_{0.5}In_{0.5}$), and the established thermoelectric materials Bi_2Te_3, Sb_2Te_3, and $BiSbTe_3$. The Ga and In containing compounds are of interest due to the low symmetry in the crystalline structure of the Ga and In compounds. In addition, similar compounds exhibit a markedly low lattice thermal conductivity [31]. As was discussed in the introduction chapter and the theoretical chapters, the lattice thermal conductivity is, in theory, the only property that is independent of the other properties. The Bi and Sb compounds have been relatively well studied under ambient conditions and are currently commercially applied as thermoelectric generators and coolers. As such, it was deemed interesting to investigate and see if their properties could be improved through the application of pressure.

The Bi and Sb compounds were purchased commercially, as shown in Table 1. In contrast, the Ga and In samples, as well as the solid solution of the Bi and Sb compounds needed to be prepared in lab. However, as Ga at room temperature is a liquid (T_{melt} = 29.78 °C), it is impossible to grind this elemental material into

Table 1 Elements used for sample synthesis

Element	Manufacturer	Purity(Percent)
Ga	Sigma Aldrich	99.999
In	Sigma Aldrich	99.99
Te	Spectrum Chemicals	99.5
Bi_2Te_3	Alfa Aesar	99.98
Sb_2Te_3	Sigma Aldrich	99

a powder. To accomplish the reaction, the tellurium powder was ground and pelletized in the stoichiometric amount. The raw materials and prepared compound amounts were kept refrigerated to make preparation easier and keep the prepared amounts from reacting until in the furnace. A portion of the solid gallium lumps was cleaved off and weighed in the respective stoichiometric amount. This process was repeated for the In material. These tubes were placed in a temperature controlled tube furnace at 900 °C for 3 days, followed by a 2 day period below the melting point of the sample to anneal it. The only deviation from this for the materials used in these investigations was the $BiSbTe_3$ solid solution. This deviation will be presented at the beginning of the chapter regarding this material.

After this process was complete, the sample was ground in a clean agate mortar to randomize the powder and examined using x-ray facilities available through the UNLV Geoscience department to verify composition. Some of the powder was pelletized and cleaved into a rough square shape for the heat capacity experiments described below. The remaining powder was divided, with some retained as powder for the diffraction experiments and the rest was pelletized, cut, and buffed to the appropriate size for the high pressure transport measurements.

Ambient Pressure X-Ray Characterization

For the samples used in this study, x-ray diffraction (XRD) was used to verify the crystalline structures and compositions under ambient conditions. The system used (X'pert X-Ray Diffractometer) for this analysis is setup for angle dispersive diffraction with a rotatable Cu K-α emitter and detector arms to allow a complete range of $\approx$ 120 degrees of 2θ space. The spectrum gathered was then checked using the software available with the system for composition and the structure parameters determined from MDI's Jade software package[32].

Ambient Pressure Heat Capacity Measurements

To measure the heat capacity, a Physical Property Measurement System (PPMS), developed by Quantum Design Inc., is used. The sample measurements are made through use of a small interface system, called a puck, which is imaged in Figure 3. This puck consists of a copper housing with internal wiring supporting an alumina stage for the sample.

Figure 3 Heat Capacity Puck

By using these leads, the system sends in a heat pulse to a resistive heater, allowing the temperature of the alumina stage plus sample to rise a small amount. Then, it measures the decay of the heat pulse back to the surrounding temperature. By fitting this to two-tau (with tau being a characteristic exponential decay time) response curves

$$C_{plat}\frac{dT_{plat}}{dt} = P(t) - \lambda_w(T_{plat}(t) - T_b) + \lambda_{grease}(T_{sam}(t) - T_{plat}(t)) \tag{5.1}$$

and

$$C_{sam}\frac{dT_{sam}}{dt} = -\lambda_{grease}(T_{sam}(t) - T_{plat}(t)) \tag{5.2}$$

the system can determine the heat capacity of the sample. In these equations, the subscripts sam and plat refer to the sample and the alumina platform, respectively. In addition, the symbols C, T, λ, P, and t are heat capacity, temperature, thermal conductivity, power, and time, respectively.

To perform the experiment, the sample puck is prepared with a small amount of thermal grease (either Apiezon brand H or N grease) to assist with thermal contact for the sample later. The stage and grease are run through the system separately to measure the background heat capacity for all components of the system. After measurement of this addendum, the sample is placed on the stage and put in good thermal contact with the alumina support. Then, the system is prepared and run, in the same manner as the addendum, to determine the heat capacity of just the sample. The addendum values allow for the removal of any contribution from a source other than the sample.

High Pressure X-Ray Measurements

The high pressure x-ray structure measurements are performed using a diamond anvil cell (DAC) of the Merrill-Bassett type. The pressure is applied to the sample through the use of two opposed diamond anvils, with the force provided through the use of three screws placed in the cell housing. A picture of the DAC is presented in Figure 4. Between the diamonds, a metal gasket is placed to prevent the diamonds from damaging each other through direct contact and to help retain the pressure. This is accomplished by using the diamonds to ”pre-indent” the working area of the gasket to a thickness between 50 and 100 microns thick. This thickness allows enough remaining material to have the strength to retain the pressure inside the cell.

Figure 4 Merrill Bassett type Diamond Anvil Cell (DAC)

This pre-indention is then centered under either a mechanical drill press or an electric discharge machine (EDM) to drill a hole in the middle of the pre-indent for the sample chamber. The sample chamber is then cleaned to be free of debris

and filled with a small amount of sample, a pressure transmitting medium, and a pressure marker. For the purposes of this experiment the pressure marker is a ruby sphere, as the ruby can be fluoresced using a laser of short visible wavelength (usually green or blue) providing two noticible emission peaks from the ruby, as shown in Figure 5.

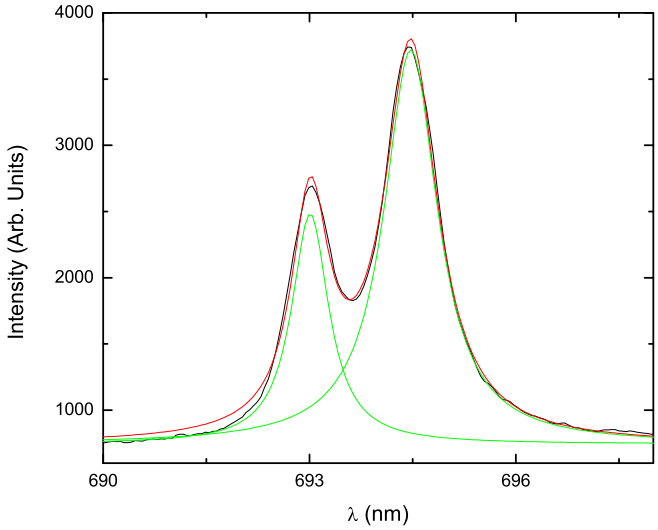

Figure 5 Ruby Fluorescence Peaks

Several studies have been performed on the ruby demonstrating the shift in these emission peaks with pressure fits a simple equation [33] of the form

$$P = \frac{A}{B}[1 + (\frac{\Delta\lambda}{\lambda_0})]^B - 1 \tag{5.3}$$

where is P is the pressure, $\Delta\lambda$ is the wavelength shift of the R1 fluorescence line, λ_0 is the initial wavelength of the R1 line at ambient pressure, and A and B are constants determined by a least squares fit. These constants have values reported by the authors of the paper as A $= 19.04$ Mbar and B $= 7.665$. With regards to the pressure transmitting medium, it is usually liquid or gas as these provide nearly

hydrostatic conditions for the sample. Typical pressure media are 4:1 by volume Methanol to Ethanol, Silicone Fluid, or gaseous Neon or Argon.

To perform a diffraction experiment, the cell is placed in the path of a beam of synchrotron x-rays focused to a spot on the sample. The sample is then exposed for a certain period of time with the data being collected by either a CCD or an image plate. The results of these exposures on a powder sample are ring patterns, as pictured in Figure 6. These figures are of little direct use, but can be converted into a more useful 2Θ versus Intensity plot, shown in Figure 7, using the program Fit2D[34], which can be imported into MDI's Jade [32] for structure determination and parameter calculation.

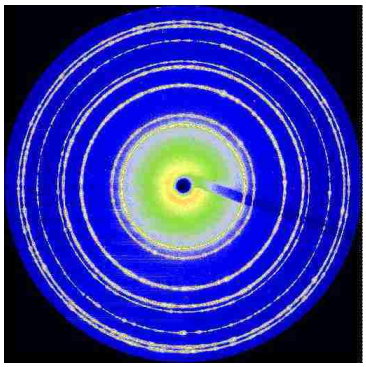

Figure 6 Image Plate Exposure of Cerium Dioxide Calibrant Sample

For this work, use was made of the relationship between the High Pressure Science and Engineering Center of UNLV (HiPSEC) and the High Pressure Collaborative Access Team (HPCAT) at Argonne National Laboratory's Advanced Photon Source (APS). This relationship provides the opportunity to make these measurements using the high intensity synchrotron souce and facilities available at the beamlines run by HPCAT. The experiments were performed at beamlines 16-ID-B (Angle Dispersive) and 16-BM-D (Energy Dispersive) at HPCAT. The experiments were performed using a wavelength of 0.41198 Å(Gallium and Indium Samples) or

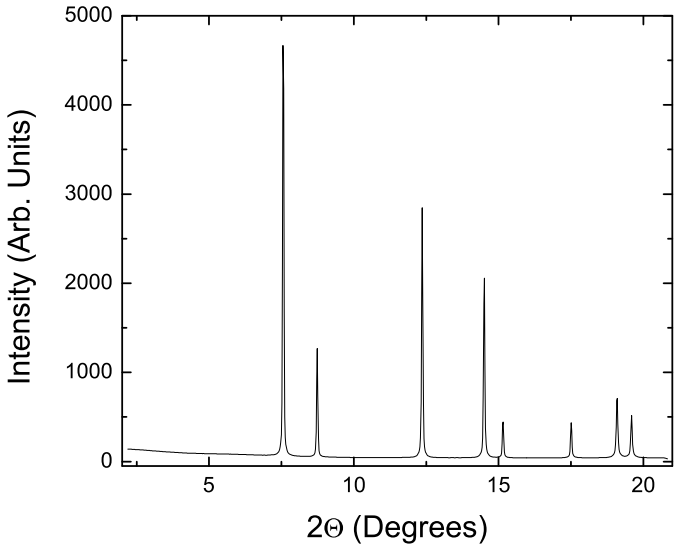

Figure 7 Integrated 2-Theta versus Intensity of Cerium Dioxide Calibrant

0.40165 Å(Bi_2Te_3, Sb_2Te_3, $BiSbTe_3$ samples) on ID-B and a detector angle of 12 degrees for BM-D. Any improtant particular details of the experiments are presented in the results chapters for the individual samples.

High Pressure Transport Measurements

Cell Setup

As there are no experiment setups available at this point for the concurrent measurement of electrical and thermal transport of materials under pressure, it was necessary to develop the setup to perform these experiments. To accomplish this task, several references were used ([35],[36],[37]) to determine the optimal sample thickness, maximal pressure, and working faces of the anvils. Through these references, it was determined that the cell should support a sample size of roughly 1.5 x 1.0 x 0.15 mm in a bar shape.

With this sample size, a split gasket setup is used, with a two mm diameter

steatite pressure transmitting disc, supported on the outside by a six mm outer diameter pyrophyllite annulus for pressure retention. These materials are commonly used for the purpose of creating high pressure environments inside opposed anvil Bridgman cells. Thus, the working face of the anvils is set to be six mm, with the pressure medium to retaining gasket ratio being determined from the references previously mentioned. The anvils were shaped, using the information presented in Yousuf's work[37], to have a ten degree taper angle. This would maximize the internal pressure of the cell, as determined by

$$P_{max} = \frac{1}{2}B^2 \frac{exp(Ba)}{exp(Ba) - Ba - 1}(a + Z_b cot(\alpha))^2 S_A \tag{5.4}$$

from Yousuf's paper, to be between 35 and 50 GPa. In this equation, a is the radius of the working face of the anvil, Z_b is the height of the tapered portion of the anvil, α is the taper angle, $B = 2\mu/h$, with μ being the coefficient of friction between the anvil and gasket and h being the critical thickness of the gasket, and S_A being the compressive strength of the anvil. Pyrophyllite makes an ideal retention gasket, as the material is an electrical and thermal insulator, which will assist in limiting the loss of heat to the surroundings from the sample and prevent electrical short circuits through the material. A schematic diagram of the cell is presented in Figure 8.

Pressure Determination

It is also important to know the internal pressure of the system. To accomplish this, it is necessary to use resistive standards to calibrate the internal pressure to an external gauge. In this case, the hydraulic press used to apply the pressure to the cell was modified to use a pressure transducer and a low-speed, high-torque stepper motor to control the pressure applied to the cell. The calibration of the internal pressure can be done using standards defined by NIST and accepted by

the high pressure community, as listed in Table 2.

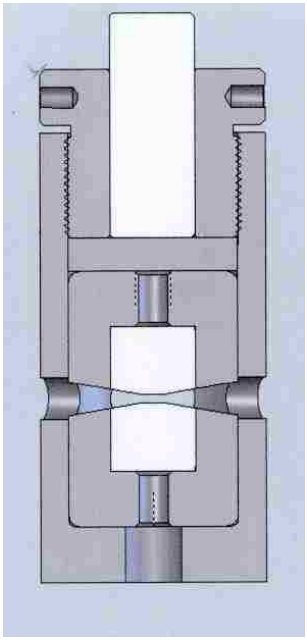

Figure 8 Schematic of Tungsten Carbide Cell

For this work, the pressure was calibrated up to 20 GPa using the Bismuth, Tin, and Lead resistive transitions. Each material was measured twice, for repeatability of the pressure transition. This was done with both copper and thermocouple electrical leads to check for consistency between the leads and test if thermocouples could be expected to produce accurate resistance results. Examples of results on the calibrants is shown in Figures 9 and 10.

In addition to the high pressure check of the thermocouple resistance measurements, ambient pressure checks were done using standard resistors with a five percent nominal error in their value. These resistors were connected through pressure contacts to the thermocouple bulb to see what resistance they measured. The results of this test are shown in Table 3.

The calibrant samples resulted in the pressure calibration curve shown in Fig-

Table 2 High Pressure Resistive Standards at 25 Celcius

Material	Pressure (GPa)
Bismuth	2.550 (6) [38]
Bismuth	2.7 [39]
Thallium	3.68 (3) [38]
Barium	5.5 (1) [38]
Bismuth	7.7 (2) [38]
Tin	9.4 (3) [38]
Barium	12.3 (5) [38]
Lead	13.4 (6) [38]
Zinc Sulphide	15.4 (7) [40]
Gallium Phosphide	22.0 (8) [40]

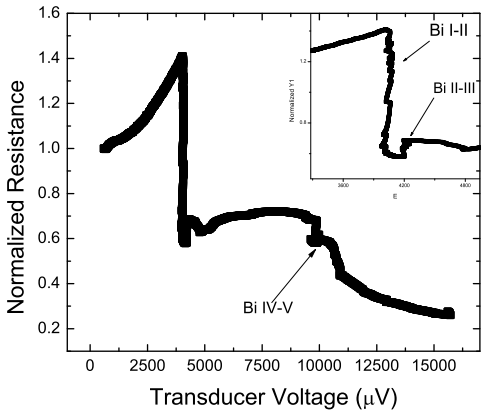

Figure 9 Bismuth Transitions

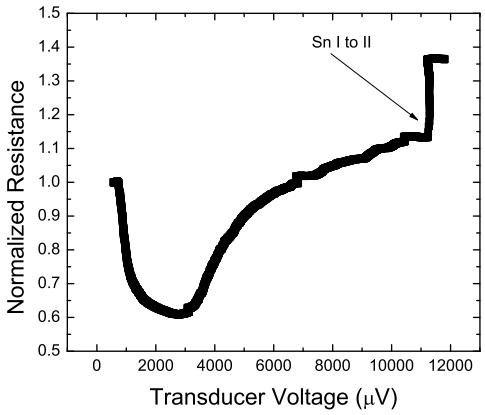

Figure 10 Tin Transition

Table 3 Resistance Bridge Test Results

Nominal Resistance (Ω)	Measured Resistance (Ω)
10	10.129
1000	990
100,000	99,210
680,000	674,400
1,000,000	975,300
5,000,000	4,855,000

ure 11. The error in the pressure of the cell is determined through experimental means, using the breadth of the resistive transition. In theory, resistive transitions should be sharply defined and instantaneous. However, the measured resistance curves show a breadth to the transition. By measuring this, a curve can be used to correlate the error in the pressure measurement to the applied pressure in the cell. This resulted in a linear relationship with the form

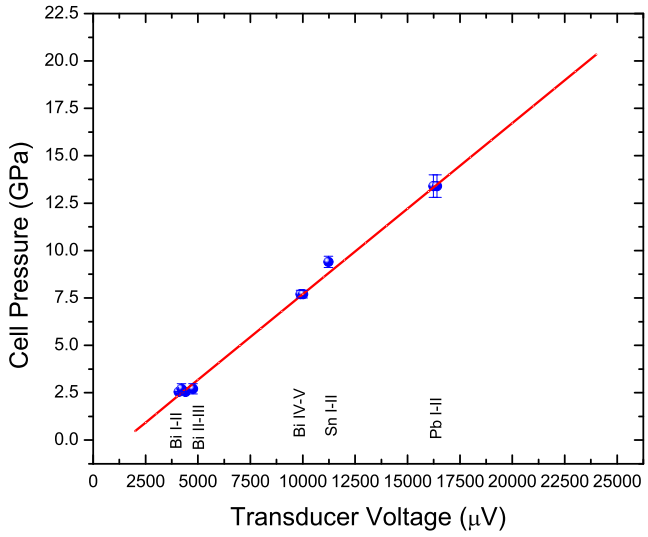

Figure 11 Pressure Calibration Curve

$$\Delta P = 0.2213(1) + 0.01296(35)P. \tag{5.5}$$

Internal Heating Setup

Temperature differences in the cell were provided by an externally controlled heating element inside the sample chamber. This heating element is constructed by spot welding a chromel wire of diameter 0.005 inches to copper wires with a diameter approximately three times larger. This setup is connected to a computer

controlled 150 watt DC power supply (10 V, 15 A) to provide the temperature differential to the sample. The copper wire was tested prior to the taking of any data to ensure it could handle the heat load required for this task. As the weld joints are too large to place inside the sample chamber, these points were coated with an electrically conducting silver epoxy and connected to aluminum foil. This arrangement allows the heating element to short the current to the chromel wire inside the sample chamber, preventing the chromel outside from overheating and becoming a fuse.

Resistance Measurements

The resistance of the sample under study was measured using a pseudo four wire probe through a Lakeshore Model 370 AC resistance bridge. The electrical leads used were thermocouples, with the similar materials used for the paired leads (i.e. chromel wires used for current leads). This device measures using an AC current, which will eliminate the thermoelectric contribution to the resistivity. From the measured resistance, the resistivity is computed using

$$\rho = \frac{RA}{L} \tag{5.6}$$

with A being the cross sectional area, L being the distance between thermocouple bulbs, and R being the measured resistance.

Error Determination in Resistivity The overall error in the system is represented by the formula

$$\sigma_\rho = \sqrt{\sigma_L^2 + \sigma_A^2 + \sigma_R^2} \tag{5.7}$$

with the σs being the respective errors in each of the measured quanities. It should be noted at this point that the error in A is also a product of errors and was treated

as such throughout these experiments. For these errors, the distances for A and L were measured using a calibrated microscope with maximal resolution of 5 μm, and the errors in the resistance were determined from the manufacturer provided calibration table and from deviations in the measured resistance value.

Thermal Conductivity Measurements

In general, the study of thermal parameters for materials presents a significant challenge to experimentalists. This is due to the inherent difficulty in the measurement and accuracy of thermal parameters. Since *any* experimental setup for the determination of these parameters will require a material with a differing thermal conductivity than the sample under study, it is important to minimize the effects such a combination will have on the system. As a result, a detailed study of literature regarding these experiments will present several accepted methods and styles of measurement.

The temperature difference can be measured and used to determine the thermal conductivity through the equation

$$\lambda = \frac{P}{A}\frac{\partial x}{\partial T} \tag{5.8}$$

with P being the power dissipated through the heater wire, A being the cross sectional area of the sample, $\frac{\partial x}{\partial T}$ being the length of the sample divided by the change in temperature.

This particular equation for the thermal conductivity illustrates the two styles of measurement typically used. In addition, the type of material and thermal profile need to be considered in the measurement style. As a result, the guarded versus unguarded style of measurement needs to be addressed also. If the material surrounding the sample is of much lower thermal conductivity ($\lambda_{sam} >> \lambda_{sur}$),

then the system is using the unguarded (or standard) heat flow style. This means that the heat flow into the sample will not appreciably flow out the sides of the sample, due to the much higher thermal conductivity. In contrast, if the thermal conductivity of the sample and surroundings are of the same order ($\lambda_{sam} \approx \lambda_{sur}$), then the system is using the guarded heat flow style. This means that the sample and surroundings have similar thermal profiles and results in a consistent thermal gradient across the sample.

For thermal experiments, the two common measurement styles are the steady-state and the transient style. This really deals with the region of the heat versus time curve used for measurement purposes. As illustrated in Figure 12, the transient heat flow method uses the thermal difference measured during the heating process and uses the parameters ΔT and time to find the thermal conductivity. This can be done in the previous equation, by replacing P with the abosrbed energy divided by the time. Thus, it would be expected to find a linear relationship with the slope being related directly to the thermal conductivity. In contrast, if the system is allowed to equilibrate, the measurement can directly use the previous equation and is called steady-state. The steady-state method will provide a much more consistent measurement of the thermal conductivity, but may have a larger error than the transient method.

As was already mentioned, the heater is brought in through the sides of the cell. The heater cannot be in direct contact with the sample due to interference in the Seebeck and temperature measurements caused by the heater current flowing through the sample. As such, care is taken in each experiment to ensure that the heaters do not contact the sample. The setup is depicted in Figure 13.

For the considerations of the model, the system is operated in steady state mode, so the power into any given portion of the sample chamber is equal to the power out of that portion. As such, the model need only consider the portion of the

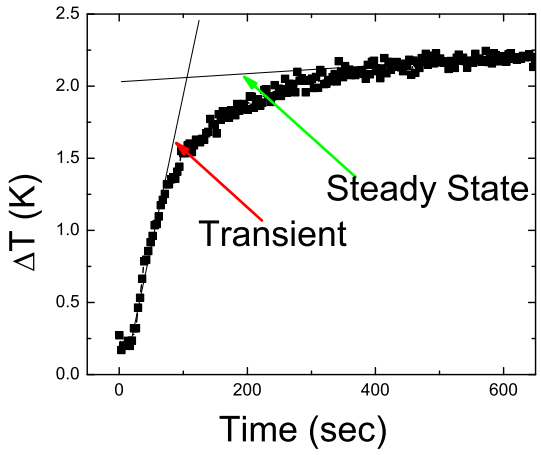

Figure 12 Heat Flow Regions in Thermal Conductivity Experiments

sample chamber containing the actual sample. In this manner, if the power used in the thermal conductivity equation is restricted to the power emitted directly into the sample, it is possible to disregard the effect of the material directly surrounding the sides of the sample. To do this, a coupling factor needs to be introduced to restrict the power to that emitted in such a way that it couples into the sample. This factor is defined as γ in the following equations and has a value determined from geometrical considerations as

$$\gamma = \frac{W_{sam}}{L_{aha}} \frac{tan(T_{sam}/(2 * D_{hs}))}{\pi} \tag{5.9}$$

with the subscript sam applying to sample dimensions, L_{aha} being the active length of the heater wire, and D_{hs} being the distance between the heater and the sample. The geometrical consideration uses the assumption that the heater wire dissipates power uniformly along its length and in all directions.

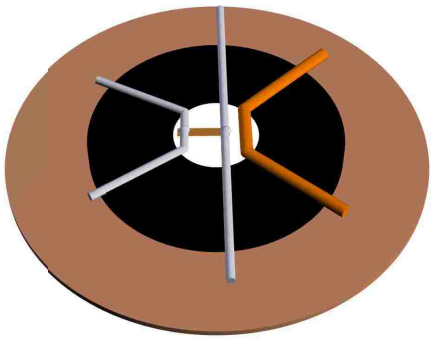

Figure 13 Setup of the High Pressure Transport Measurements

The active heater length is defined as the length of the chromel wire inside the gasket, since the remainder of the heating element will dissipate a negligible amount of energy in comparison. With this definition, the system measures the temperature difference and the sample dimensions are measured prior to the experiment using the setup previously described in the resistivity section. Then, the thermal conductivity can be determined through

$$\lambda = \frac{\gamma V I L_{sam}}{T_{sam} W_{sam} \Delta T} \tag{5.10}$$

with Δ T being the measured temperature difference, V being the voltage drop across the heater, and I being the dissipated heater current.

Error in Thermal Conductivity Measurements Similar to the errors for the high pressure resistance measurements, the equations involved in the thermal conductivity setup are products of various measured parameters. As a result, the errors for the setup is determined by

$$\sigma_\lambda = \sqrt{\sigma_L^2 + \sigma_{\Delta T}^2 + \sigma_V^2 + \sigma_I^2 + \sigma_T^2 + \sigma_W^2 + \sigma_\gamma^2} \tag{5.11}$$

with the sample dimensional errors determined in the same manner as before. The temperature and power errors are determined through statistical errors in the values and measurement errors in the Keithley multimeter recording them.

Seebeck Coefficient Measurement

The measurement process for the Seebeck coefficient is a well documented process. This process is decribed in several papers, including Polvani *et al.* [41]. By measuring the potential difference between the two matched thermocouple wires (i.e. the two alumel or chromel wires), the sample thermopower can be determined through the following line of reasoning. The thermopower of each respective contribution can be related as

$$S_s - S_{A,C} = \frac{\Delta E_{A,C}}{\Delta T} \tag{5.12}$$

with the subscripts being for samples (s), alumel (A), or chromel (C) and ΔT being the temperature difference between the two. By combining these two equations, the final sample thermopower is

$$S_s = \frac{S_A - rS_C}{1 - r} \tag{5.13}$$

with r being the ratio of the alumel potential difference to the chromel ($r = \frac{\Delta V_A}{\Delta V_C}$). In this equation, the Seebeck coefficients of the thermomaterials used is a function of the average sample temperature. As the temperature of the sample changes, the Seebeck coefficient of the thermoelements changes also. To account for this, data was taken from Bentley [42] and Wang *et al.* [43] to provide curves for the Seebeck coefficient of alumel and chromel as a function of temperature. In this manner, the computed value of the Seebeck coefficient is compensated for the change in the value for the thermocouple leads. The effect of pressure on the Seebeck coefficient of the thermocouples has been disregarded as it amounts to less than the standard

measurement error in the K type thermocouples used (K type standard error = 2.2 degrees C [42], pressure correction $\approx$ 2 degrees @ 10 GPa [44]).

Errors in Seebeck Coefficient Measurements Errors in the Seebeck Coefficient can be determined in the usual manner, through the derivative of the previous equation. By taking the derivative of this equation, the error is shown to be

$$\sigma_\alpha = (\frac{-S_C}{1-r} - \frac{S_A - r * S_C}{(1-r)^2})\sqrt{\sigma_{V_A}^2 + \sigma_{V_{A,Null}}^2 + \sigma_{V_C}^2 + \sigma_{V_{C,Null}}^2} \tag{5.14}$$

with the term in the square root being σ_r and the first term being $\frac{\partial \alpha}{\partial r}$, since r is the only variable parameter in this equation.

Setup of Measurement

To actually perform these measurements at high pressure, the following procedure was used. The gasket materials are prepared, as described previously. First, a six mm disk of the pyrophyllite is taken and, using a special gasket punch, has a two mm disc removed from the center. This annulus is centered and adhered on the working face of the anvil using superglue. Following this, one of the steatite disks is subjected to the same process, with the two mm disc used to fill in the area of the pyrophyllite disc already adhered to the anvil. This produces the lower half of the gasket.

A pellet of the sample of interest is prepared and a bar shaped segment is cut off to dimensions roughly around the design sample size for this system (1.5 (L) x 1.0 (W) x 0.15 (T) mm). A recess is carved into the steatite medium on the anvil to allow the sample to sit slightly above the surface of the bottom half gasket. Once the sample is placed inside this recess, grooves are carved in the gasket material from the sample boundary out to the edge of the gasket to allow for lead placement. These grooves are carved deep enough that the leads sit uniform with the top of

the gasket. This prevents pinching of the leads during the initial pressurization of the cell.

The leads are adhered to cut pieces of tape on the anvil surface outside the pressurization region. Following this, a pyrophyllite annulus and steatite filler are prepared in the same fashion as before. The pyrophyllite annulus's hole is centered over the sample chamber and already assembled steatite filler and adhered to the top of the lower gasket. Care is made here to ensure that superglue does not flow into the grooves carved for the leads. Once the pyrophyllite is adhered to complete the retaining gasket, the inner steatite disc is stamped into place and the experimental setup on the anvil is ready.

The anvil is then carefully lowered into the cell housing. The leads are pulled out through one of the side ports for the system and attached to the appropriate connectors. The thermocouple leads are taken and matched with the opposite lead to complete the thermocouple circuit and the thermocouples are connected to the home-built thermocouple amplifier and switch box. For the heating element, the power controller box is connected to horseshoe connectors and the stripped ends of the copper leads from the heating element are placed on top of these horseshoes. These fit into specially made standoffs attached to the side of the cell housing. The plastic standoff ensures that the heater current does not short through the cell housing. The upper anvil is lowered and fixed in place and the rest of the cell assembled.

Equipment used in the Measurement Process Using the setup described above, the measurements were taken using a variety of both home-built and store-bought equipment. The system uses the following store-bought equipment for measurement purposes:

1. Lakeshore Model 370 AC Resistance Bridge: used for the measurement of

sample resistance.

2. Keithley Model 2000 Multimeter with 10 channel switch: used for the measurement of pressure, temperature, voltage drops, and current.

3. Transducer: used to convert applied pressure to a voltage.

4. Keithley Model 2100 Sourcemeter: used to control internal heating element.

5. Stepper Motor: used to automatically increase pressure applied to system.

6. Carver Presses 25 Ton Hydraulic Benchtop Press: used to apply the pressure.

With regards to the home-built equipment, with the assistance of the Physics and Astronomy department's electrical engineer, Bill O'Donnell, the following equipment was developed

1. Stepper Motor Controller: used to control the stepper motor from the computer.

2. Transducer Power Supply and Converter: used to power the pressure transducer and read the current pressure out from the multimeter.

3. Heater Control Box: used to control the power ouput to the heater and read the dissipated current and voltage drop across the heater.

4. Thermocouple Amplifier and Switch Box (TC Amp): used to relay the thermocouples for resistance readings (to the AC bridge) and amplify the signal to measure the needed temperature and voltage drops.

Measurement Process All of the data collected by the system was collected and recorded with the use of a specially built LabVIEW program. This program takes

input parameters (sample dimensions, heater power steps, and pressure increments) from the user and performs the experiments in a semi-automated fashion. The logic process used for this measurement process is as follows:

1. Program takes input parameters and calculates pressure intervals for use in the program.

2. Program increases pressure to first measurement point, specified by user, by turning the stepper motor.

3. The heater power is then increased, in the previously defined steps, with measurements being taken at each step to the maximal value.

4. At each step, the system switches the TC Amp to resistance mode and passes the thermocouple leads through the box to the AC Bridge.

5. After the specified number of readings are taken, an average and standard deviation are computed and stored for later writing to the data file.

6. The TC Amp then switches back to temperature/potential drop mode and measures the temperatures of each thermocouple, the offset for the potential voltage, and the potential drop across the sample for each pair of wires (alumel and chromel) and then writes out all the values for that temperature to the data file.

7. After completing the heater sweep up and down, the system increases to the next pressure setpoint and repeats the process, until the maximum pressure is reached.

The output for this program appears as shown in Figure 14. This lists all of the measured properties, in the order that is listed in the column header. This is then processed using a code written in Mathematica, resulting in data that appears in

Figure 15. The result of this processing creates the plots in the results chapters. In each of these, one measurement set is highlighted.

Sample Length	Sample Width	Sample Thickness		Distance from Heater to Sample	Pressure	Sig Pressure	Alumel Null		Sig Alumel Null	Chromel Null	Sig Chromel Null
0.715	0.230	0.135	0.613	0.250	0.001	-1.010	0.031	-1.041	0.035		
Sourcemeter Output		Resistance		Sig Resistance	Alumel VDiff		Sig Alumel VDiff		Temp B	Sig Temp B	Heater Current
Sig Heater Current		Chromel VDiff		Sig Chromel VDiff	Heater Voltage		Sig Heater Voltage				
0.000	1233.530	0.596	-1.024	0.041	82.957	0.029	-1.102	0.016			
84.902	0.024	28.104	0.018	0.001	0.000						
0.100	1230.376	0.422	-1.076	0.037	82.906	0.028	-1.117	0.053			
84.977	0.032	84.566	0.031	36.086	0.002						
0.200	1229.200	0.353	-1.195	0.046	82.886	0.039	-1.138	0.015			
85.059	0.041	192.849	0.034	103.381	0.002						
0.300	1228.398	0.357	-1.409	0.035	82.846	0.057	-1.175	0.046			
85.545	0.043	365.454	0.024	191.738	0.004						
0.400	1227.782	0.312	-1.569	0.041	82.912	0.037	-1.229	0.041			
85.891	0.050	505.516	0.040	277.800	0.005						
0.500	1227.328	0.309	-1.587	0.033	83.282	0.067	-2.278	0.027			
86.357	0.049	650.412	0.089	366.179	0.006						
0.600	1226.802	0.292	-1.497	0.075	83.815	0.039	-2.302	0.035			

Figure 14 Example of Output for Transport Measurements

Bi2Te3_0.25_CompiledData.txt

Pressure	SigPressure	Average T	Sig Avg T	Delta T	Total	Rho	SigRho	Lambda	SigLambda	Alpha	SigAlpha	ZT	SigZT	Sam Thick	Sam Width	Sam Length	Power	Sig Power
0.25	0.001	292.97168148934	0.14819550937408413	1.5352283753452127														
0.00005343101370629 37	2.3249256000849973e-6	0.00393887183061094																
0.00043369595374883235	3.9616086354892725e-7	-7.563841832620167e-7																
0.00021847589139157135	0.00041793405088759374	0.000135	0.00023	0.000715														
0.0030516486759999996	1.131379358561928e-6																	
0.25	0.001	292.9796998619195	0.19735096378127387	1.5088424921854937														
0.000053379944055944054	2.3226818528064872e-6	0.025883459917184812																
0.002849951473067676	8.232497897104175e-6	-5.645723260483564e-7																
0.014371441886678084	0.0019663338161904323	0.000135	0.00023	0.000715														
0.019936922468999998	3.5360521163184233e-6																	
0.25	0.001	293.0373814450562	0.24969173677614226	1.3727809889302023														
0.000053345115944055936	2.3211676227796955e-6	0.10010765964747184																
0.01102266339921145	0.0000120261242577882 42	-5.011454184367818e-7																
0.007936196760804478	0.0009961220655982064	0.000135	0.00023	0.000715														
0.070071419052	4.828318480465016e-6																	

Figure 15 Example of Results for Transport Measurements

Ambient Pressure Transport Measurements

The theory used for the ambient pressure transport measurements is identical to that used for the high pressure transport measurements. The only major change is in the form of the coupling constant γ. This now takes on a value of

$$\gamma = \frac{1}{5} * \frac{W_{sam} * T_{sam}}{W_{heaterface} * T_{heaterface}} \tag{5.15}$$

with the numerical fraction from the ratio of the applied face of the heater versus the total surface area. A large bar shaped sample is prepared of the sample material and thermocouples are adhered to the ends of one face with a silver based epoxy. This sample is then adhered, with the same epoxy to the flat surface of the resistive heater. The epoxy is annealed in between each of the previous steps for maximal stability and tested after the sample adhesion for electrical contact. The sample setup, with the sample adhered perpendicular to the face of the heater, is placed inside a vacuum oven and connected to the measurement apparatus for the high pressure measurements. The oven is evacuated to a level of 20 inches of mercury ($\approx$ 250 torr). The system is then started and measures the properties in the same fashion used for the high pressure measurements. A picture of the resistive heater inside the oven is shown in Figure 16.

Figure 16 Ambient Pressure Setup for Transport Properties

CHAPTER 6

SYSTEM CALIBRATION TESTS: NICKEL, ALMANDINE GARNET, AND ZINC

This chapter presents the results of three materials used to confirm the capabilities of the system developed and the methods used. The materials were chosen on the availability of reference data and, more specifically, for their thermal conductivity values. The almandine garnet and zinc samples were chosen as specific tests of the measurement theory behind the thermal conductivity and the Nickel sample was chosen as a comprehensive test of the systems abilities. As such, the discussion will begin with the zinc and garnet samples before moving into the nickel sample results.

Zinc Calibrant

The first calibration sample used was zinc. The zinc sample was prepared by taking a piece of bulk zinc and cleaving a piece of it into the appropriate dimensions for the measurement system. It was loaded in the manner described in the previous chapter. For this sample and the garnet sample, the measurement was repeated three times with the results averaged. Zinc was chosen due to the reported ambient value of its thermal conductivity being around 116 W/m-K, with the Steatite thermal conductivity being approximately 2.44 W/m-K. This means that the system would be operating in the unguarded setup mentioned in the previous chapter. The results of the measurement are shown in Figure 17. These results are compared with results reported by Jacobsson *et al.*[45]. In his paper, he reports results for his experiment and work done by Bridgman.

The work reported by Jacobsson and Bridgman covers the pressure range up to 2 GPa. However, the data collected by this system agrees well with the previously reported values and the trend for the thermal conductivity agrees within the error of the measurement.

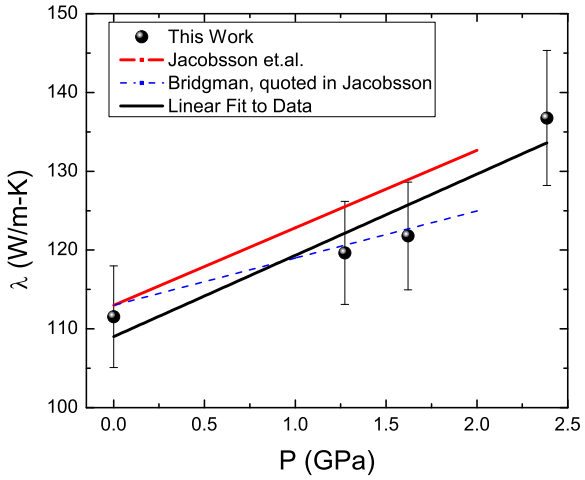

Figure 17 Thermal Conductivity of Zinc

Almandine Garnet Calibrant

The second calibration sample run was almandine garnet. The sample was graciously provided by Dr. Clay Crow of the UNLV Geoscience department. This sample was cut on a diamond saw to acceptable dimensions for the measurement system. In this case, almandine garnet has a thermal conductivity value under ambient conditions being approximately 3.4 W/m-K. Since the thermal conductivity for this sample is nearly the same as the gasket materials, this material can be used to verify the guarded hot wire setup of the system. The results of the measurements on this material are shown in Figure 18. These results are compared with the work of Osako and Ito [46].

In this figure, as with the zinc sample, the errors are determined from statistical variations of the measured quantities. It can be seen that for low thermal conductivity materials, the agreement is reasonably good between the two experiments. It would be expected that the error originating from Osako and Ito's data would be lower than the error resulting from this work, as their experiment involved

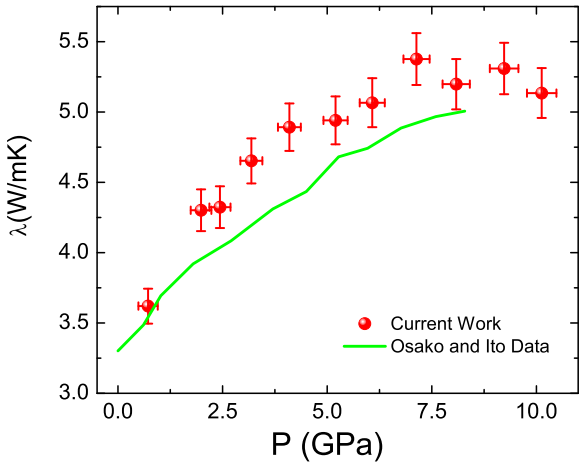

Figure 18 Thermal Conductivity of Almandine Garnet

transient measurements. However, these two samples show that the thermal conductivity measurement setup is capable of reasonably consistent measurements of the thermal conductivity.

Nickel Calibrant

In order to verify that the system as a whole is capable of measuring reasonable values for the material parameters of interest, a nickel calibrant sample was used. The nickel calibrant was obtained from Alfa Aesar with a purity of 99.994 percent. From this, two samples of the appropriate dimensions were cut and the setup prepared with each. For the nickel sample, the heater cycling was tested with a maximal dissipated heater power of approximately 14 W.

It should be noted that the electrical connections for the ambient pressure measurements were made with solder, providing reasonable structural stability, but this caused some problems with the stability of the resistivity measurements. As such, the error bar for the ambient pressure resistivity measurement appear rather large in comparison. The results of these experiments have been compared against

results from Pu [47] and Sundqvist [48] (Resistivity), Ross *et al.* [49] (Thermal Conductivity), and Chandra Sheekar *et al.* [50] (Seebeck Coefficient). Plots comparing the results of these works with the results of this experiment are presented in Figures 19-21.

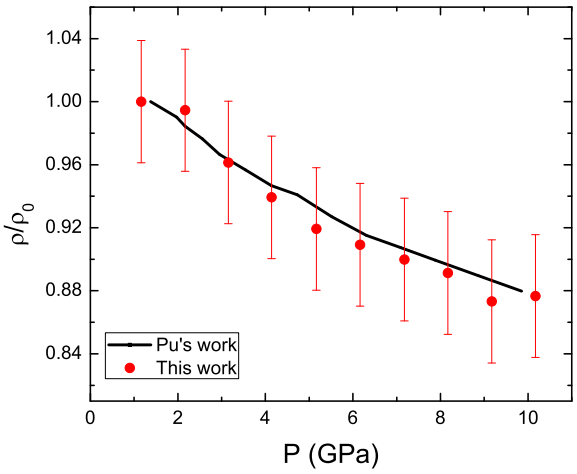

Figure 19 Ni Electrical Resistivity

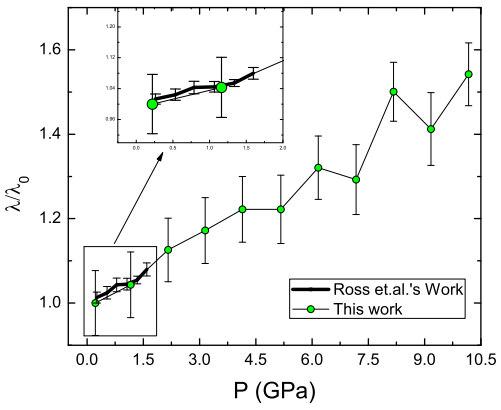

Figure 20 Ni Thermal Conductivity

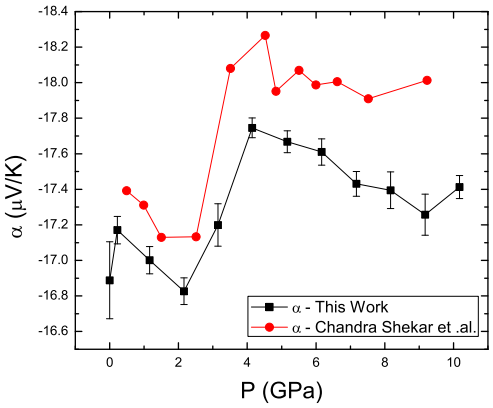

Figure 21 Ni Seebeck Coefficient

As with the previous two samples, the results of this sample show reasonable agreement with reference data. From these measurements, the ambient pressure

Table 4 Ambient Pressure Transport Properties of Nickel

Property	Measured Value	Reference Value
ρ ($\mu\Omega$ - cm)	7.55 (83)	7.237 [48]
λ (W/m-K)	88.5 (70)	70 - 87.5 [52]
α (μV/K)	-16.88 (2)	-17.38 [50]

values were determined to be as shown in Table 4, compared with the previous reference results. In addition to this data, the resistivity data can be used to get an estimate of the Gruneisen parameter of nickel. This can be accomplished in the following manner. As was mentioned in the chapter on electrical properties of materials (Ch. 3), it is expected for metallic substances that equation 3.11 holds. A graphical representation of this is shown in Figure 22. When the fit was performed, statistical errors for the resistivity values were included. From this, it can be obtained that the Gruneisen parameter should be equal to 1.86 (11), which is in good agreement with the results of Bandyopadhyay *et al.* [51].

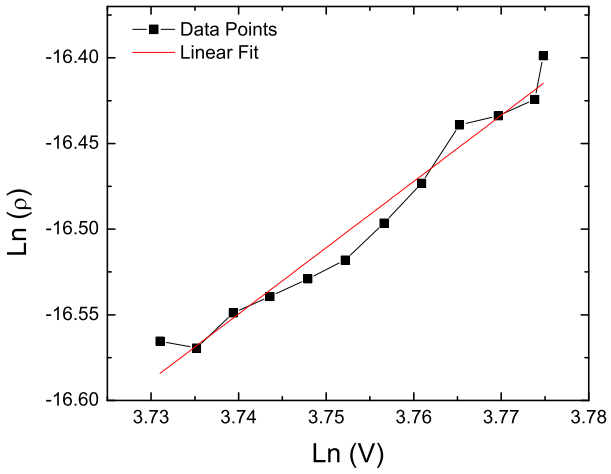

Figure 22 Log-Log plot of Resistance versus Cell Volume for Nickel

CHAPTER 7

SAMPLE RESULTS : BI_2TE_3

In this chapter and the following five, results for the samples measured in this study are presented. This information will be organized in the following manner. First, the heat capacity measurements and fit results will be presented. This will be compared, when available, to reference data. Following this, the x-ray structure measurements will be presented, including ambient values. Finally, the results of the high and ambient pressure transport measurements will be presented and compared with reference data, when available.

In this chapter, the focus will be on the established thermoelectric material Bi_2Te_3. This material has been demonstrated to display the necessary qualities to make it an effective thermoelectric material when doped to specific levels. However, fundamental studies on the undoped material have been rather sparse, leaving some question as to whether the raw material itself is good or if the dopants make it an effective thermoelectric. As such, it is of interest, from both basic theoretical and applied physics standpoints to investigate the material properties without the intentional presence of dopants.

Ambient Pressure Heat Capacity

From the previously described setup for the PPMS system, the heat capacity for Bi_2Te_3 has been measured on a 49.21 mg sample. This measurement was segmented into two temperature regions, one from 2-250 Kelvin and one from 250-350 K, to account for a previously reported anomaly in the heat capacity of the thermal grease used. As reported in a technical release from Quantum Design [53], the heat capacity measured for Apiezon brand N-grease shown a significant anomaly occuring around 280 K. To avoid an adverse effect on the data due to this, the temperature range was divided and the upper temperature range was measured using

Apiezon brand H-grease, which does not show this anomaly.

After collection of the data, the results were then analyzed with a Mathematica program to determine a Debye fit to the data. This fit resulted in a Debye temperature of 141 K $\pm$ 2 K and the curve shown in Figure 23. In this the measured heat capacity at constant pressure was converted to constant volume using the measured bulk modulus, molar volume, and temperature, and thermal expansion data from Taylor [54]. This results clearly shows that, for all of the transport properties of this material, ambient temperature is in the high temperature regime. As such, the theories that depend on this condition are valid.

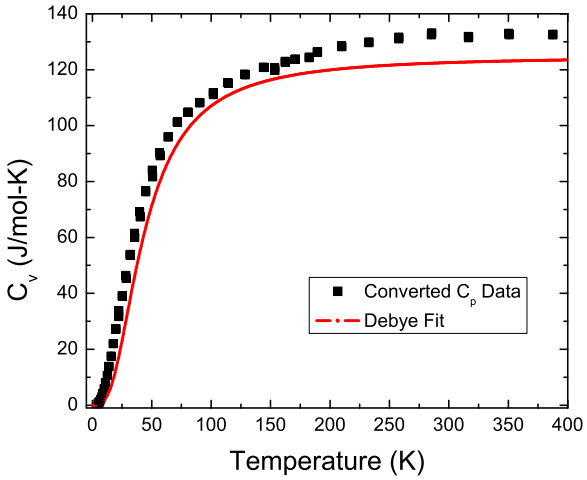

Figure 23 Heat Capacity of Bi_2Te_3

In addition to this, previous results on Bi_2Te_3 have been measured by Gorbachuk *et al.* [3]. A comparison of these results with the measured values show a good agreement over the majority of the temperature region. It is unclear what causes the sudden deviation in Gorbachuk's values occuring around 65 K, but the cause is likely experimental, as no trend has ever been reported for heat capacity with this sudden drop.

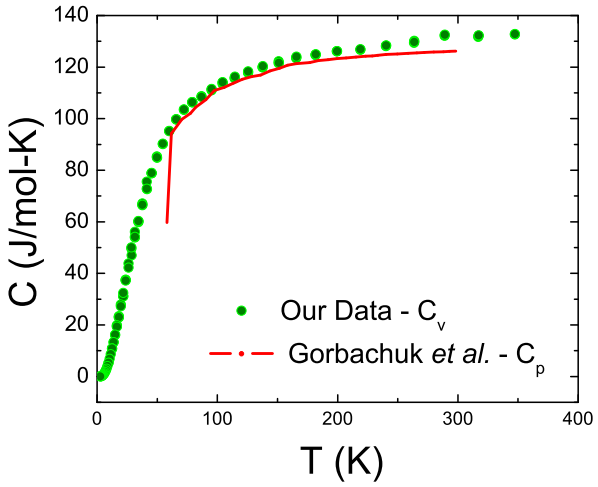

Figure 24 Comparison with Gorbachuk *et al.* Data [3]

Structure Measurements

Ambient Pressure

For use with the high pressure x-ray experiments, the ambient pressure characterization was carried out using facilities in the Geoscience department at UNLV. This characterization produced the diffraction plot shown in Figure 25. By using Jade to analyze this pattern, it was found that the initial unit cell is a rhombohedral structure in class $R\bar{3}m$ and has cell parameters as shown in Table 5. The ambient pressure data has been found to be in good agreement with several temperature related works on this material ([55], [56], [57]).

High Pressure

The high pressure measurements were performed as described in the experimental details chapter. These measurements resulted in the discovery of two phase transitions in the structure of Bi_2Te_3 under pressure. The pressure versus volume data is shown in Figure 26 with the equation of state fits.

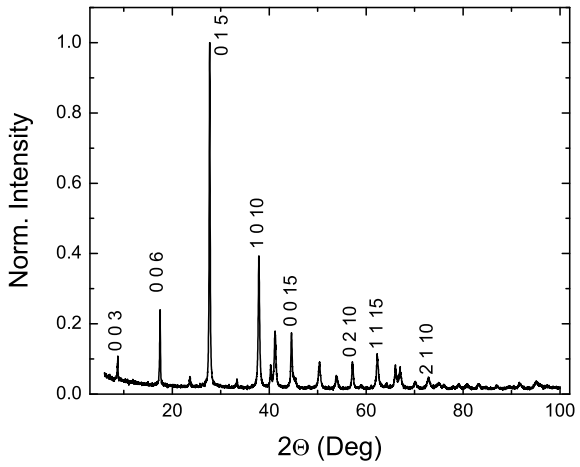

Figure 25 Ambient Pressure Bi_2Te_3 Pattern

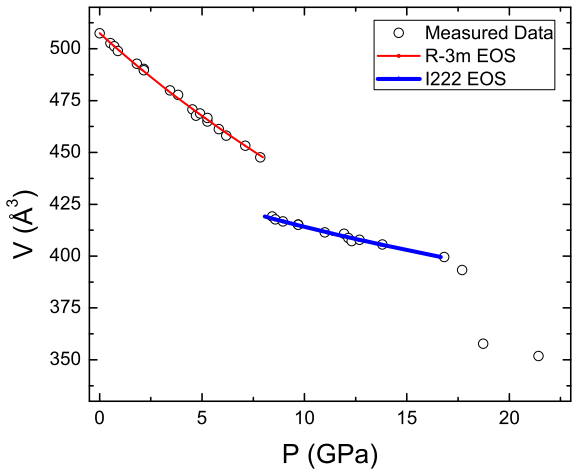

Figure 26 Applied Pressure vs. Cell Volume for Bi_2Te_3

From the results of the measurements, it was determined that the high pressure phase was likely the orthorhombic I222 space group. With the use of EOSFit, the equation of state parameters for both were determined and are shown in Table 5 along with the cell parameter and volume data obtained from Jade. This data was

Table 5 Bi_2Te_3 Structural Parameter Results

Parameter	$R\bar{3}m$	I222
a ($\AA$)	4.3860 (8)	11.66 (1)
b ($\AA$)	4.3860 (8)	4.819 (1)
c ($\AA$)	30.46 (1)	7.467 (1)
V_0 ($\AA^3$)	507.5 (1)	445 (2)
B_0 (GPa)	56.2 (1)	112 (6)
$B_0^{'}$	2.1 (3)	6.01 (63)
Transition Pressure (GPa)	7.8	16

fit using a 3^{rd} order Birch-Murnaghan equation of state fit, which has the form

$$P(V) = \frac{3B_0}{2}((\frac{V_0}{V})^{7/3} + (\frac{V_0}{V})^{5/3})(1 + \frac{3}{4}(B_0^{'} - 4)((\frac{V_0}{V})^{2/3} - 1)). \tag{7.1}$$

In this table, the final row presents the pressure where the next phase of the sample appears. The high pressure data for this sample was measured out to 20 GPa and there is evidence of another phase transition that occurs around 16 GPa. However, there is not enough data taken to obtain anything useful regarding this structure.

For the high pressure work, previous results published by Vereshchagin *et al.* [58] and Khvostantsev *et al.* ([59],[60]) both report a resistive phase transition in the Bi_2Te_3 structure occuring between 6.5 and 8.0 GPa. In these reports, studies on the hydrostaticity of the measurement is not presented, so it is likely that this variation in the transition pressure is due to non-hydrostaticity of the pressure medium. Regardless, the transition pressures reported in these two works agree well with the measured transition pressure from this work. As neither work involved structural determinations of this material, it is impossible to test the agreement at this point that the new structure is truly the I222 structure. However, the transitions have been shown to be reproducible from x-ray work presented by Nakayama *et al.* [61].

Further investigations of the structure can take us to the ETT anomaly analysis, presented in Chapter 3. Using equations 3.16 and 3.17, it becomes possible to identify changes in slope of these state equations. A change in slope has been proposed to be indicative of this type of transition in the material. To determine this, the collected data has been converted and the plot is shown in Figure 27.

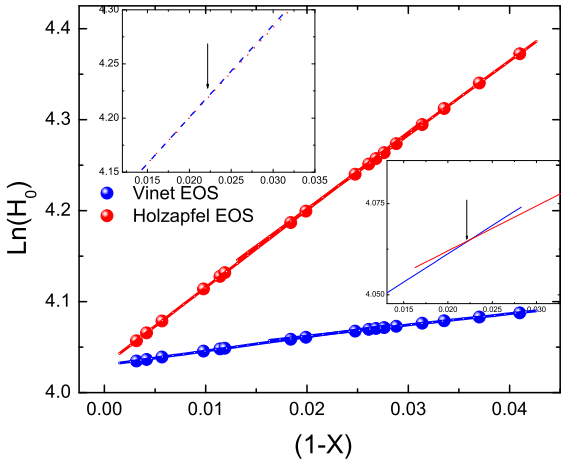

Figure 27 ETT Equation of State Plot for Bi_2Te_3

This figure demonstrates that, for the initial phase of the material, there is a discontinuous slope occuring around $X = 0.0225$, or a pressure of $P \approx 3$ GPa. This particular slope change is more obvious in the Holzapfel equation of state than in the Vinet equation of state and is only slight in both cases. Furthermore, previous measurements by Itskevich *et al.* [62] and theoretical calculations by Larson *et al.* [12] support the existence of this type of discontinuity and the potential for an ETT. The work of Khvostantsev *et al.* [59] also has a measured phase line occuring around this pressure value, as measured in his resistivity work. Nakayama *et al.* [61] has come to the conclusion that there is some change in the electronic interactions of this material as the pressure is increased. They measured that the structure of this material has one bulk modulus value when the applied pressure does not

increase above 2.5 GPa and takes on a completely different value when P is increased above this point. As a result, there is very strong evidence that something occurs in Bi_2Te_3 at this pressure, but further work needs to be done to understand more completely what is occuring.

High Pressure Transport Properties

Using the setup described in the previous chapters, the high pressure resistivity, thermal conductivity, and Seebeck coefficient were measured in the range from ambient to 10 GPa. The results of these measurements are shown in Figures 28 and 29, with the ambient pressure values shown in Table 6.

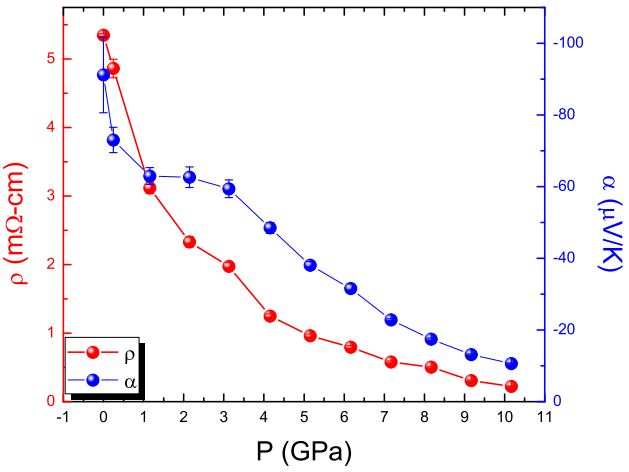

Figure 28 Resistivity and Seebeck Coefficient versus Pressure for Bi_2Te_3

Resistivity For the electrical resistivity, the pressure trend has been compared with results from Vereshchagin[58] and shows a reasonable level of agreement, as shown in Figure 30. In the data measured here, there is a shoulder between 2 and 4 GPa, corresponding reasonably well to the structure anomaly. In addition to this, there is another discontinuity in the resistivity occuring around 8 GPa, with corre-

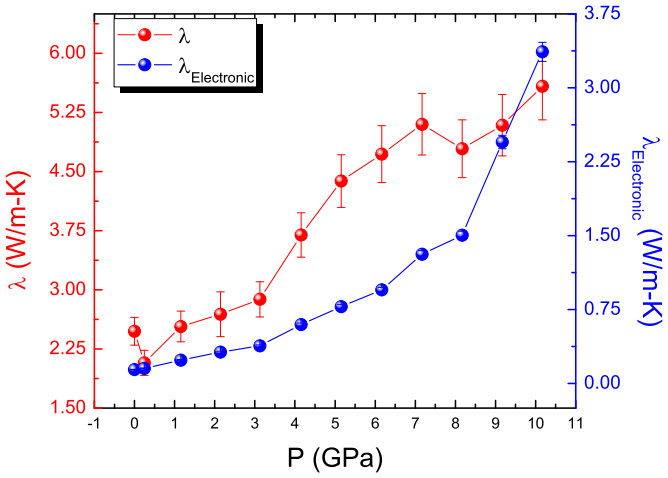

Figure 29 Total and Electronic Thermal Conductivity versus Pressure for Bi_2Te_3

Table 6 Average Ambient Pressure Transport Properties for Bi_2Te_3

Property	Measured Value
ρ (mΩ-cm)	5.35 (2)
λ (W/m-K)	2.47 (17)
α (μV/K)	-91 (10)

lates well with the structural transition found in this work and by Nakayama[61].

Seebeck Coefficient The ambient pressure value measured for the Seebeck coefficient of Bi_2Te_3 has been found to be in good agreement with the values reported previously ([63],[64]). In addition to the anomaly in the resistivity data, the effect of pressure on the Seebeck coefficient of this material shows a rather pronounced shoulder, occuring around the location of the proposed ETT. It should also be noted that there is no evidence in this property of the phase transition around 8 GPa. This suggests that, in Bi_2Te_3, the structural phase transition preseves the ratio of the potential difference to the temperature difference. This can be checked by using the following relation

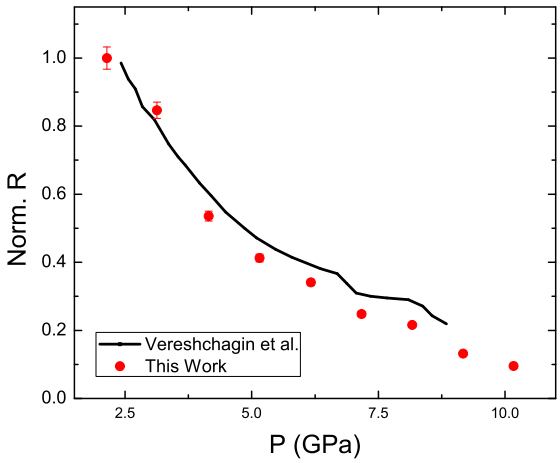

Figure 30 Normalized Resistivity versus Pressure for Bi_2Te_3

$$\alpha \propto \frac{\Delta V}{\Delta T} = \frac{I\rho\lambda}{P} \tag{7.2}$$

where I is the current, P is the heater power, and ρ and λ are the electrical resistivity and thermal conductivity, respectively. A plot of $\rho\lambda$ is shown in Figure 31. As can be seen in this plot, this slope remains unchanged between 7 and 9 GPa. This is a very interesting result, as there is no reason to expect that a structural change in the material will alter the electrical and thermal conductivity is such a way as to leave the Seebeck coefficient unchanged.

Despite these interesting results, the data collected in this work does not agree with the work of Ovsyannikov *et al.* [65]. The results from Ovsyannikov's work show that, for a p-type single crystal, the Seebeck coefficient increases to 2 GPa, with vast swings in the value between 3 GPa and the limit of his experiment (8 GPa). It is unclear at this point what the cause of the discrepancy is, but it is likely due to differences between the properties of the p-type material and the undoped material and possibly due to differences between the pelletized powder sample

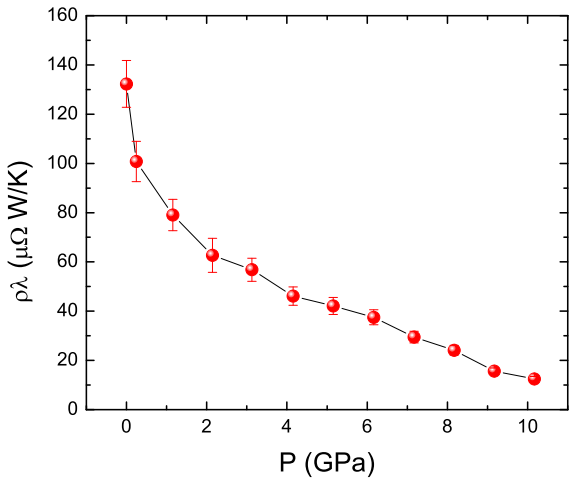

Figure 31 $\rho\lambda$ versus Pressure for Bi_2Te_3

and the single crystal sample. Another possible cause for this is non-hydrostaticity, which has been reported to cause conflicting results. An example of such a conflict can be seen between the results of Vereshchagin[58] and Einaga[66], as both use a multi-anvil apparati with solid pressure media (which is known to be quasi-hydrostatic at best). Regardless of the cause, the fact that a difference is present merits further investigation.

Going beyond this, for a semiconducting material (or even a semimetal), it is possible to gain information regarding the shift in the position of the Fermi energy with pressure from equation 4.11. From this equation, a pressure derivative can be taken, which will relate the pressure slope of the Seebeck coefficient to the pressure slope of the band gap energy. In this case, by band gap energy, the reference is to the position of the Fermi level relative to the bottom of the conduction band. This derivative results in

$$\frac{\partial \Delta E}{\partial P} = -eT\frac{\partial \alpha}{\partial P} \tag{7.3}$$

with e being the fundamental charge, T being the temperature of the system, and Δ E being the band gap energy, as previously defined. This can be altered, by removing the fundamental charge constant, to result in energies in electron volts. By doing this, the result for Bi_2Te_3 is that the Fermi energy shifts towards the conduction band at a rate of 2.22 meV/GPa. As such, the carrier concentration in the material is increasing with pressure. This can be concluded based on the fact that the decreasing distance between the conduction band and the Fermi level will make the thermal energy required to overcome the remainder of the band gap larger.

Thermal Conductivity The thermal conductivity of Bi_2Te_3 with pressure is shown in Figure 29, and has been found to agree well with reports from Goldsmid [67] regarding the ambient pressure value for near intrinsic forms of this material. In this figure, it is easily noted that the total thermal conductivity of this material has a drastic change in slope occuring between 3 and 4 GPa. As with the previous two properties, this corresponds well with the reported occurence of the electronic topological transition and with the measured anomaly in the structure and resistivity. This is interesting as it suggests that the phonon dynamics change in conjunction with the Fermi surface shape for this material. In addition, the structural transition shows a rather pronounced decrease in the thermal conductivity. It is found by converting the electrical resistivity to the electronic thermal conductivity through equation 2.11 that the high pressure phase of Bi_2Te_3 displays strong evidence of a trend towards metallic behavior. As such, it would be of great interest to investigate the second high pressure phase to see if this trend continues.

In addition to this information, it is possible to estimate the lattice thermal conductivity of this material. This is accomplished by subtracting the electronic component of the thermal conductivity from the total thermal conductivity. By doing this, the result is plotted in Figure 32. From this plot, it is seen that the ambi-

ent value appears to be somewhat high, or the phonon relaxation time decreases rapidly under slight stress. From this, the value recovers and shows a slight increase with pressure. If only the slight increase between 1 and 3 GPa is considered, the slope of $ln(\lambda_{lat})$ versus P is found to be 0.102 $\pm$ 0.011, which is in close agreement with the theoretical model of Hofmeister presented in chapter 2 with the numerical constant being 6 ($\frac{\partial ln(\lambda_{lat})}{\partial P} = 0.107$). From this point, the effects of the phase transition on the lattice conductivity is pronounced, as it increases dramatically until the phase transition. From this pressure onward, the value decreases steadily with further application of pressure.

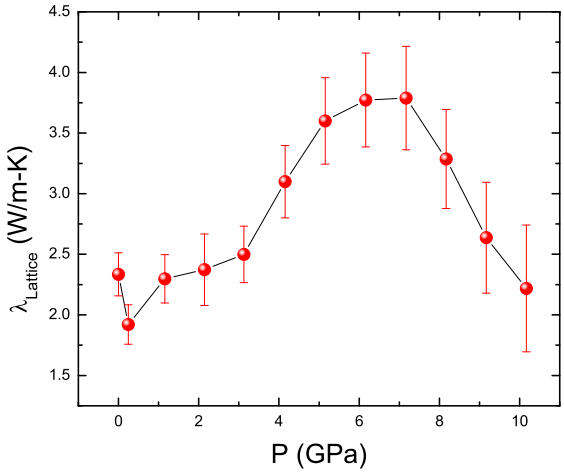

Figure 32 Lattice Thermal Conductivity of Bi_2Te_3

Conclusions

Depsite this occurance, this trend suggests that the higher pressure phases should be expected to become less useful for devices with increasing pressure. This is due to the discussion in the theoretical chapters regarding metallic substances. The lack of an ability to support a substantial potential difference, the

high thermal conductivity, and the trend towards metallic behavior all suggest that the optimal structure for this material is the ambient pressure form, or a negative pressure form. This could be achieved with the addition of atoms to force the lattice further apart than it currently is. From the data taken, the overall trend for the figure of merit parameter, ZT, is shown in Figure 33. It is easily seen in this figure that the ZT for this material decreases from 0-2 GPa. The occurence of the structural anomaly in the material improves the thermoelectric performance, but further increase of the applied pressure destroys this enhancement and makes Bi_2Te_3 a rather ineffective thermoelectric, decreasing the performance by a factor of 10.

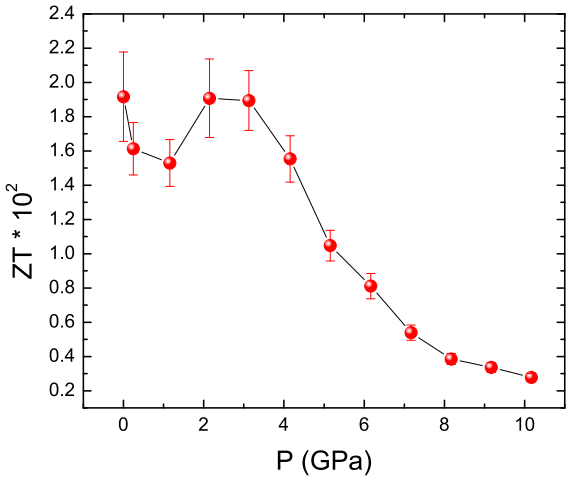

Figure 33 ZT versus Pressure of Bi_2Te_3

It has further been found by Fleurial *et al.* [4] that the effect of the liquidus composition of the melt material has a dramatic effect on the figure of merit of the material. As such, the doping of the material has been demonstrated to have a strong effect on the resulting thermoelectric material. The graph presented in his paper regarding this is shown in Figure 34, with the bottom axis being the liquidus composition of the melt.

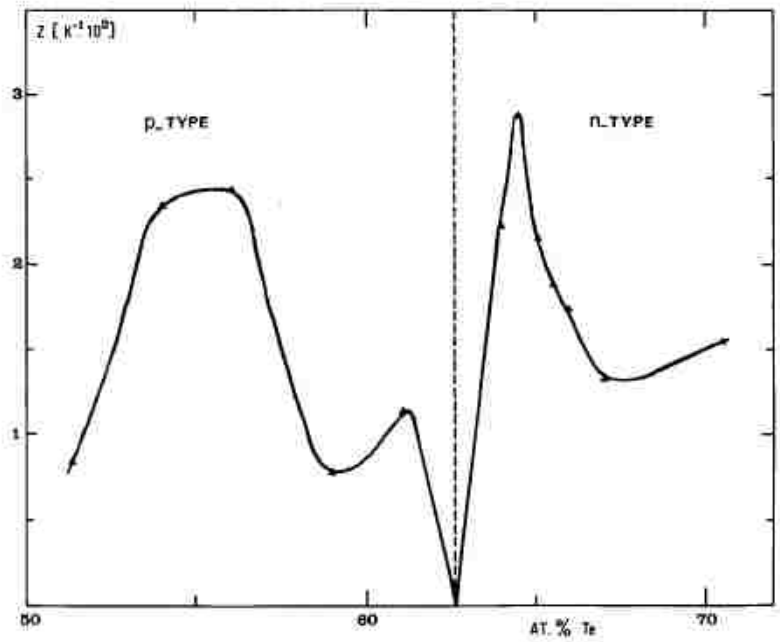

Figure 34 Figure of Merit versus Liquidus Composition [4]

As this graph shows, the doping of the material, whether intentional or not, has drastic effects on the thermoelectric performance of the resultant material. This lends further support to the previous result regarding the measured Seebeck coefficient from this work and that presented by Ovsyannikov *et al.*, with the difference being likely due to the p-type nature of their single crystal. This also shows that a slightly more n-type melt results in a significant improvement in the figure of merit over the undoped sample.

There are several other reports regarding either solid solutions or doped versions of Bi_2Te_3 in various compositions. One of these that holds some particular interest is the report by Zhu *et al.* [5], in which solid solutions of PbTe with this material are investigated. This is of particular interest as PbTe has been shown to demonstrate remarkable thermoelectric properties in the nanoscale form, as reported by Harman *et al.* [9]. The resutls show that alloys of this type have no significant effect on the overall thermal conductivity, but can improve the electri-

cal properties of the composite over PbTe on it own. Further, if the alloying is not done to a large degree, this can result in no significant change to the Seebeck coefficient, creating a material with a ZT that is better than that of undoped Bi_2Te_3.

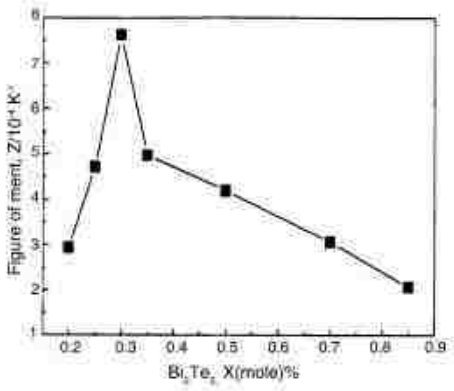

Figure 35 Figure of Merit versus molar percent Bi_2Te_3 [5]

Finally, there has been some interest in doping single crystals of Bi_2Te_3 with Ga [6]. In the work cited, they show that this doping can be used to shift the temperature at which the material performs the best, to higher temperatures. The price of this is that the maximal value at that temperature decreases with the increasing dopant level. To compare these results with the data in this work, it is necessary to use what is called the thermopower of the sample measured here. This property is the Seebeck coefficient divided by the electrical resistivity and results in the plots below, with the data from the reference put in as a function of temperature. The doping levels of the individual samples is shown in Table 7, with the undoped sample being p-type. Some of the samples measured in the reference work are n-type, with the data in the graph being the absolute value relative to the starting value.

It is interesting to note that the undoped sample used in this work exhibits a resistivity close to that of both the p and n-type samples with dopant levels around 0.4 molar percent Ga. However, it is seen easily that the dopant level significantly

Table 7 Doping Level of Bi_2Te_3 with Ga [6]

Sample	molar percent Ga
1	0.00 (p-type)
2	0.31 (p-type)
3	0.34 (p-type)
4	0.41 (n-type)
5	0.46 (n-type)
6	0.70 (n-type)

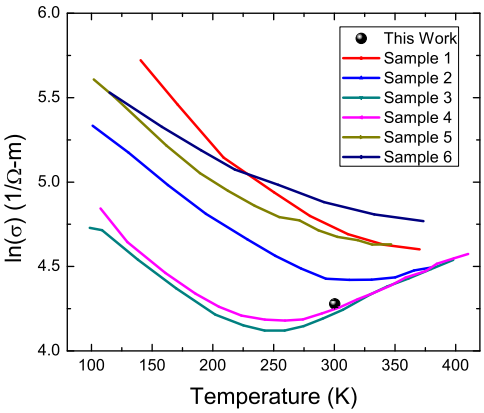

Figure 36 ρ of Bi_2Te_3 [6]

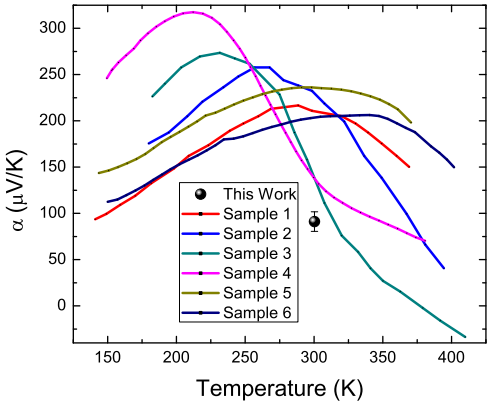

Figure 37 α of Bi_2Te_3 [6]

improves the Seebeck coefficient values over the undoped samples.

CHAPTER 8

SAMPLE RESULTS : SB_2TE_3

In this chapter, the discussion will focus on the results of experiments involving Sb_2Te_3. This material shows specific promise not on its own, but alloyed with other thermoelectric materials. It has been shown experimentally, by Venkatasubramanian *et al.* [68], that thin film alloys between this material and Bi_2Te_3 show strong promise as efficient thermoelectric materials. As such, an investigation of its properties under pressure was performed in an effort to better understand the structure and properties of this material.

Heat Capacity

The heat capacity of Sb_2Te_3 has been measured, using the previously described setup, on a 54 mg sample. This was measured in the range from 4 K to 390K. The resulting data is plotted in Figure 38 with a Debye temperature fit to the data. The fit resulted in an overall Debye temperature of 177.8 $\pm$ 1.5 K. As with Bi_2Te_3, the measured bulk modulus, molar volume, and temperature were used to convert from constant pressure to constant volume heat capacity. As there was no readily available thermal expansion data on this material, it was assumed that the thermal expansion coefficient was the same as that for Bi_2Te_3. While this is likely not the case, it at least provides an estimate for the Debye temperature of this material. This sample also lies in the high temperature regime for theoretical purposes.

Structure Studies

Ambient Pressure

As with Bi_2Te_3, Sb_2Te_3 crystallizes into the $R\bar{3}m$ structure under ambient conditions. The structure was measured and verified using the facilities in the Geo-

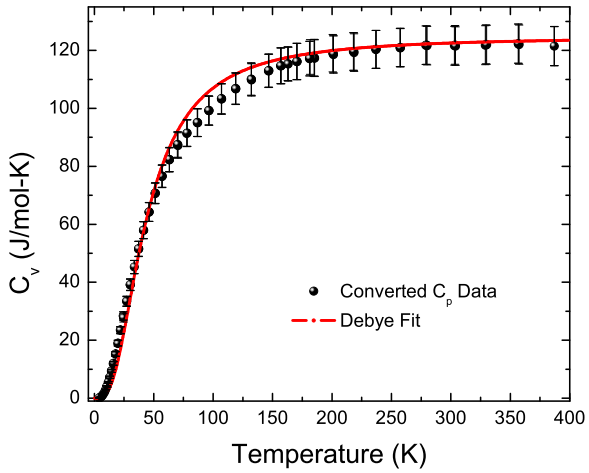

Figure 38 Heat Capacity versus Temperature for Sb_2Te_3

science department at UNLV. The ambient pressure pattern is shown in Figure 39, with the hkl indicies for some of the peaks shown.

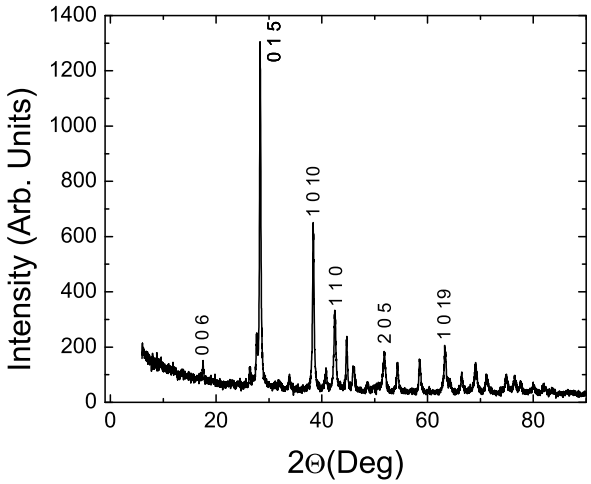

Figure 39 Ambient Pressure Diffraction Pattern for Sb_2Te_3

High Pressure

With the application of pressure to the material, it was found that the ambient pressure structure remains until the pressure exceeds 9.5 GPa. At this point, the structure undergoes a similar transition to that seen previously in Bi_2Te_3. It was found that the orthorhombic high pressure structure remains until 20 GPa, where there is another transition. This second high pressure phase is similar to the second high pressure phase for the Bi sample and was indexed to the orthorhombic Ima2 space group. However, there was not enough data to make a reasonable fit for the equation of state of this material. The pressure-volume data and Birch-Murnaghan equation of state fits are shown in Figure 40. Cell data and fit results are shown in Table 8. It was found with this material that release of pressure returns it to the ambient pressure structure.

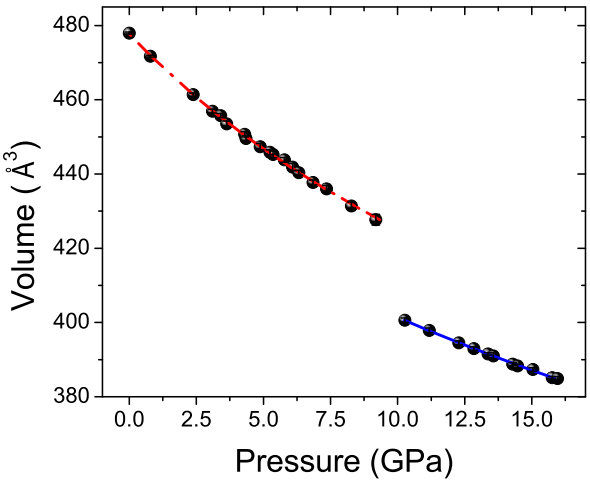

Figure 40 Applied Pressure vs. Cell Volume for Sb_2Te_3

Previous results regarding structural measurements from Sakai *et al.* [69] agree with the change of structure occuring around 9 GPa, but do not fit the structure. There is also evidence of a structure anomaly in this material, as can be seen in Fig-

Table 8 Sb_2Te_3 Structural Parameter Results

Parameter	$R\bar{3}m$	I222
a ($\AA$)	4.265 (1)	3.466 (2)
b ($\AA$)	4.265 (1)	9.436 (5)
c ($\AA$)	30.45 (1)	11.725 (7)
V_0 ($\AA^3$)	479.0 (6)	440.4 (15)
B_0 (GPa)	30.2 (14)	61 (3)
$B_0^{'}$	9.4 (11)	3.4 (4)
Transition Pressure (GPa)	9.5	20

ure 41. The marked point corresponds to a pressure of approximately 2.5 GPa. This is in good agreement with the theoretical results of Larson [30] and of Bartkowiak *et al.* [70]. The resistivity results of Khvostantsev *et al.* [60] also support this anomaly's occurance.

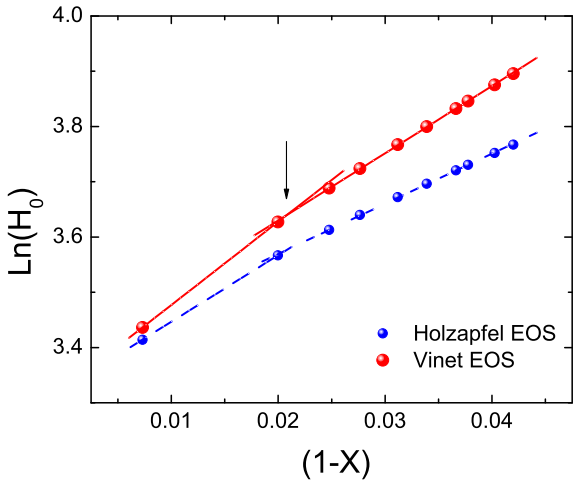

Figure 41 ETT Equation of State Plot for Sb_2Te_3

High Pressure Transport Properties

The results from the high pressure transport experiments are shown in Figures 42 and 43. The ambient pressure results for the transport properties were found to be as shown in Table 9. It was found that these values agree well with previous reports from Sakai *et al.* [69] (Resistivity) and Ibrahim *et al.* [71] (Seebeck Coefficient). The thermal conductivity value was found to agree well with the extrapolated trend from Ismaiylova *et al.* [72].

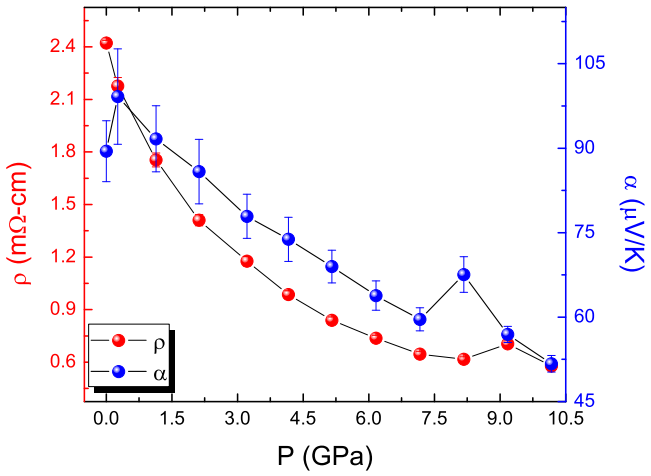

Figure 42 Resistivity and Seebeck Coefficient versus Pressure for Sb_2Te_3

Resistivity The resistivity of this material is shown to decrease is an uniform fashion with applied pressure up to 9 GPa, where the resistivity makes a substantial jump corresponding to the structural phase transition. In the case of this sample, there is no obvious evidence from the resistivity corresponding the the proported ETT for this material. The pressure trend for this material is also found to be consistent with the results of Sakai *et al.* [69], as is shown in Figure 44. It is also found to be consistent with the results of Khvostantsev *et al.* [60].

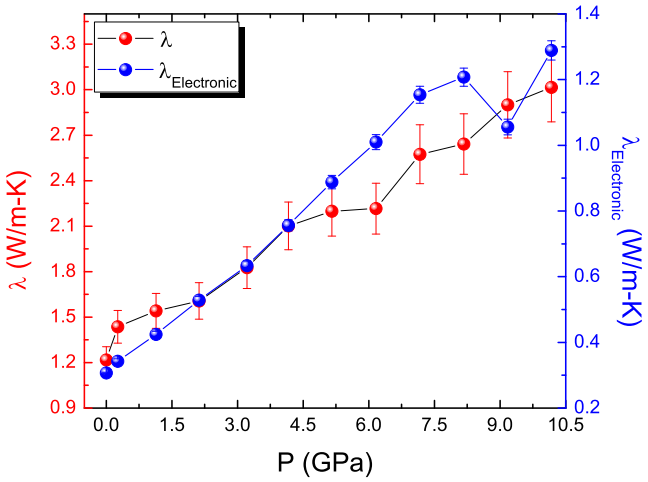

Figure 43 Total and Electronic Thermal Conductivity versus Pressure for Sb_2Te_3

Table 9 Average Ambient Pressure Transport Properties for Sb_2Te_3

Property	Measured Value
ρ (mΩ-cm)	2.42 (1)
λ (W/m-K)	1.22 (8)
α (μV/K)	89.5 (54)

Seebeck Coefficient As is shown in Figure 42, the Seebeck coefficient of Sb_2Te_3 shows some interesting pressure effects. First, the initial upturn in the value of the Seebeck coefficient occuring at low pressures. This particular occurence may be evidence for the ETT theorized for this material. However, it does not correlate with the structural anomaly and occurs at a much lower pressure than supposed by theory. In addition to this, there is a marked change in the Seebeck coefficient occuring at nearly 8 GPa. It is the supposition here that this is due to the structural transition, despite the fact that the structural transition occurs at a slightly higher pressure. It seems plausible the precursors to a structural transition would manifest in the electrical and thermoelectic properties of a material, with the Seebeck

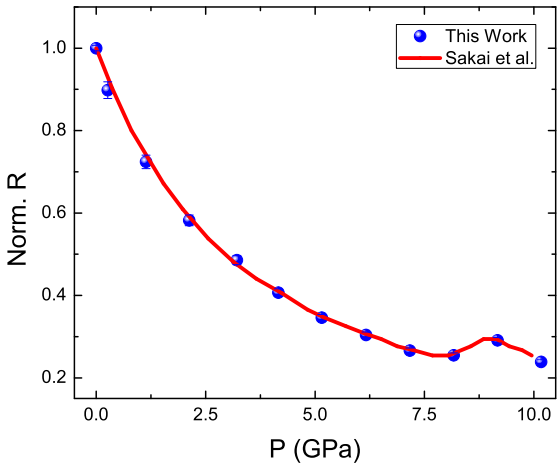

Figure 44 Normalized Resistance versus Pressure

coefficient and resistivity being reasonable indicators. As with Bi_2Te_3, a plot can be made with the resistivity times the thermal conductivity. This plot is shown in Figure 45. As can be seen in the plot, one would expect that the Seebeck coefficient would display interesting behavior at pressures of 0.5 GPa and 9 GPa. While the second point doesn't match exactly with the upturn in the Seebeck coefficient plot, it does agree fairly well with the phase transition. The first point, however, reproduces the initial upturn in the Seebeck coefficient. It is reported, in the theoretical work mentioned previously, that the reason for the interesting low pressure behavior is due to the collapsing of the band gap in this material under the initial pressurization of the material.

As the sign of the Seebeck coefficient is positive, this indicates p-type conduction in the material. In this case, the energy gap defined in Chapter 7 is the distance between the top of the valence band and the Fermi energy, since for p-type materials, the Fermi energy is closer to the valence band. It was found from a fit of the Seebeck coefficient data, that the Fermi energy is moving towards the valence band at a rate of 1.60 meV/GPa below 8 GPa. Once the system passes the structural tran-

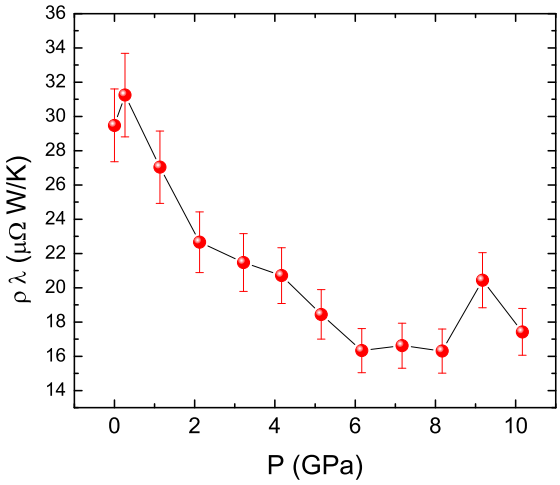

Figure 45 $\rho\lambda$ versus Pressure for Sb_2Te_3

sition effect, the rate increases to 2.49 meV/GPa. In both cases, the decrease of the distance between the valence band and the Fermi energy, along with the decrease in the electrical resistance of the material, suggest a trend towards metallicity.

Thermal Conductivity The thermal conductivity of Sb_2Te_3, as shown in Figure 43, shows no particular discontinuities in the pressure trend. In conjunction with this, the electronic component of the thermal conductivity, calculated using equation 2.11, shows the obvious discontinuity associated with the phase transition. This suggests that the phonon structure of the material compensates for the changes in the electronic structure at the phase transition. In addition, the similarity between the slope of the electronic thermal and total thermal conductivities suggests that this material is trending towards metallic behavior. As such, it would be expected that the second high pressure phase would likely become metallic.

As with Bi_2Te_3, the lattice component of the thermal conductivity was computed for this material and is shown in Figure 46. It was found that the lattice shows an increasing level of thermal conduction with pressure. In addition,

there is no obvious change correlating with the phase transition, suggesting that the phonon structure is unaffected by the transition. This material was found to show a slope for $ln(\lambda_{lat})$ versus P of 0.076 $\pm$ 0.004 W/m-K-GPa, which is less than Hofmeister's [22] theory with a theoretical value of between 0.133 (n=4) and 0.199 (n=6), where n is a numerical constant with no set value (although theorized to be either 4 or 6).

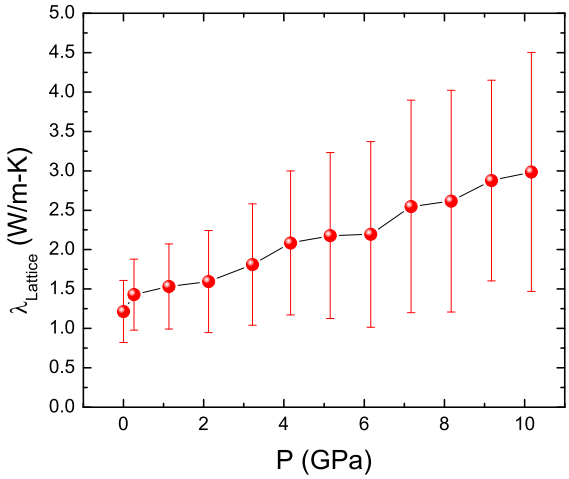

Figure 46 Lattice Thermal Conductivity of Sb_2Te_3

Conclusions

From the results on this sample, it is easily seen that, as with Bi_2Te_3, the ambient pressure structure has the better thermoelectric potential than the higher pressure phase. This is clearly demonstrated on inspection of the plot of ZT versus pressure in Figure 47. In contrast with the results from Bi_2Te_3, Sb_2Te_3 shows some initial improvement while compression is still in the low pressure region of this experiment. This would suggest that the optimal properties for this material would be realized with a slightly smaller structure than the ambient pressure structure has. In addi-

tion, the initial evidence of the phase transition in the Seebeck coefficient causes an obvious anomaly in the ZT parameter, returning the transitioning structure to an efficiency nearly that of the slightly strained structure.

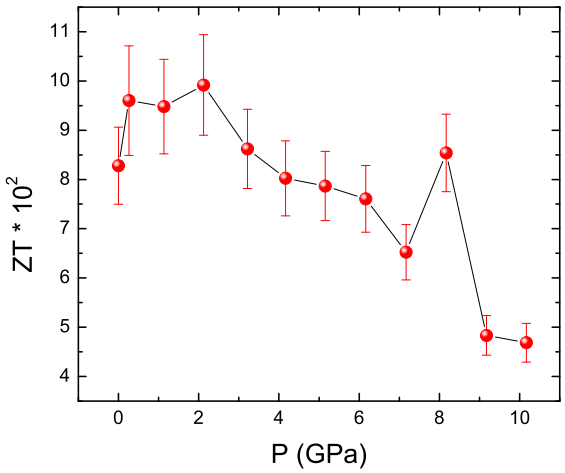

Figure 47 ZT versus Pressure of Sb_2Te_3

CHAPTER 9

SAMPLE RESULTS : BISBTE$_3$

In this chapter, the discussion turns to a solid solution between the previous two materials. It has been reported in several places that solid solutions of these two materials show improved thermoelectric performance over the individual compounds. As such, it was deemed important to investigate the structure and transport properties of the solid solution to further quantify the lattice and electron dynamics in these materials.

Sample Synthesis

The material prepared and used for this sample was created by using a 50:50 ratio of Bi_2Te_3:Sb_2Te_3 mixed in an agate mortar and pestle until finely ground. The material was then pelletized and reacted at 850 degrees C for 2 days, then annealed at 550 degrees C for 6 days. Another batch of the powder was prepared in the same manner and mechanically ball milled for 9 hours. It was found that the ball milled material resulted in a better end sample than the solid state reaction did. As a result, the ball-milled material has been used for all subsequent experimental procedures.

Heat Capacity

The heat capacity of this material was measured in the temperature range from 2 to 390 K, using the method described in the previous chapters. The results for this sample are shown in Figure 48, with a Debye temperature of 224.4 ± 2.4 K. Although the Debye temperature is only 60 K below ambient, this is still enough for the assumption that the material is in the high temperature limit for the purposes of the transport experiments. As with Sb_2Te_3, there was no thermal expansion data available to convert from constant pressure to constant volume heat capac-

ity. It was assumed that the thermal expansion values of Bi_2Te_3 should be roughly applicable to this sample also.

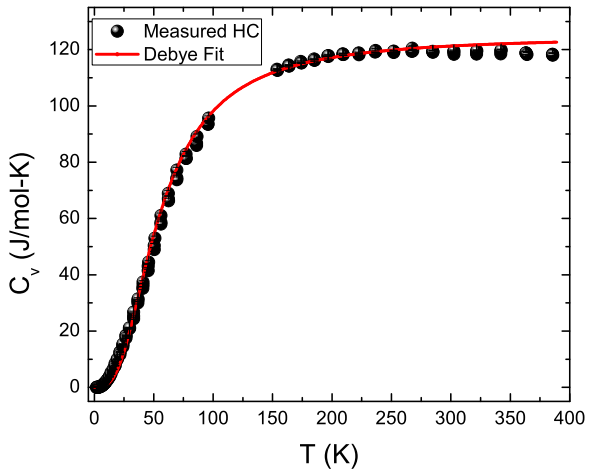

Figure 48 Heat Capacity of $BiSbTe_3$

Structural Characteristics

Ambient Structure

The ambient pressure structure for this material was found to be the hexagonal space group $R\bar{3}m$ (166), with cell parameters as presented in Table 10. The ambient pressure pattern with peak indices is shown in Figure 49. This pattern was found to match reference patterns [73] available in the x-ray software.

In the heat capacity section of this chapter and the previous one, it was assumed that the thermal expansion data for Bi_2Te_3 would be applicable to both samples. This can be justified in part through the use of Vegard's law. As can be seen in Figure 50, there exists a linear relationship between the unit cell volume and the fractional percentage of Sb_2Te_3 (or the Bi sample), which makes Vegard's law valid for this group of samples. It is therefore possible to assume that the thermal expan-

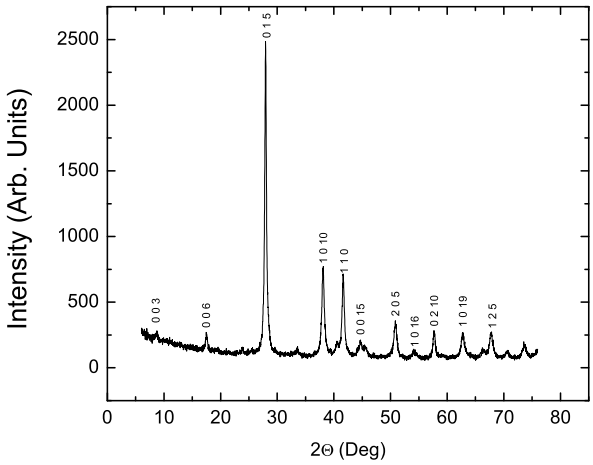

Figure 49 $BiSbTe_3$ Ambient Diffraction Pattern

sion coefficient for the solid solution and the antimony variant would be similar to that for the bismuth sample, although the numerical value is likely different.

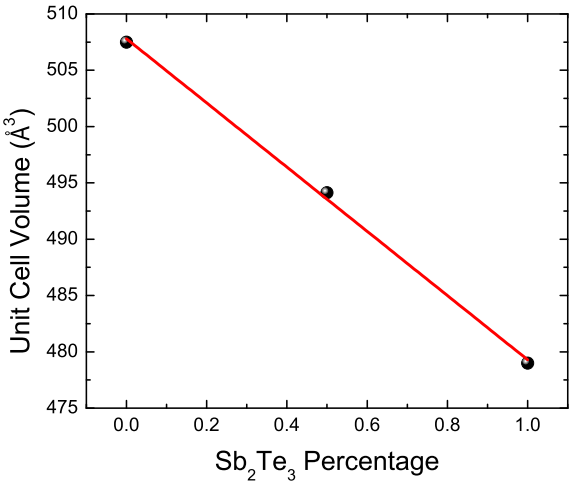

Figure 50 Cell Volume versus Sb_2Te_3 concentration

Table 10 $BiSbTe_3$ Structural Parameter Results

Parameter	$R\bar{3}m$	I222
a ($\AA$)	4.333 (3)	11.581 (17)
b ($\AA$)	————	4.787 (7)
c ($\AA$)	30.38 (1)	7.498 (15)
V_0 ($\AA^3$)	494.14 (58)	441.06 (97)
B_0 (GPa)	56 (2)	100.6 (29)
$B_0^{'}$	5.27 (84)	6.15 (31)
Transition Pressure (GPa)	7.3	————

High Pressure Structure

It was found under compression that this material transforms, as the two parent compounds do, to an orthorhombic structure, with the best fit being the I222 space group. This was determined to occur at around 7.3 GPa. The limit for the experimental study done here was 18 GPa and it was found that the high pressure I222 structure remained until the limit of the experiment. It is not unreasonable to expect that the transition seen in the parent compounds would occur with this material also. The equation of state fits were done to a Birch-Murnaghan equation of state, with the initial unit cell parameters and the fitted parameters presented in Table 10. A plot of the measured data and the equation of state fits is shown in Figure 51.

It is interesting to note that the evidence present in the previous two samples regarding an ETT does not appear in this material. This can be seen on inspection of Figure 52. The lines can be fit directly to the equations of state without any obvious change in slope, suggesting that there is no change in the Fermi surface of this material with increasing pressure.

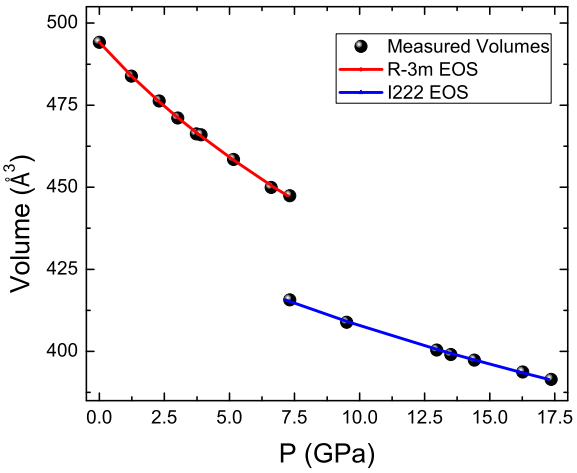

Figure 51 Applied Pressure vs. Cell Volume for $BiSbTe_3$

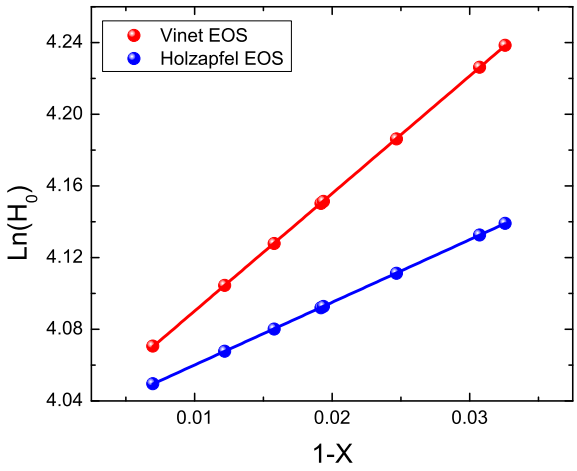

Figure 52 ETT Equation of State Plot for $BiSbTe_3$

High Pressure Transport Properties

The results of the high pressure transport measurements are shown in Figures 53 and 54. The measured ambient pressure values are reported in Table 11. These values have been compared with references and show good agreement with Kul-

bachinskii *et al.* [7] and Jeon *et al.* [74] for the Seebeck coefficient and the resistivity. The reported thermal conductivities vary between 0.99 W/m-K (Kulbachinskii) and 1.7 W/m-K (Jeon). The discrepancy between the values is reported to be strongly related to growth conditions of the material, as reported by Cosgrove *et al.* [75]. Regardless, the measured value here is in the range of values reported previously.

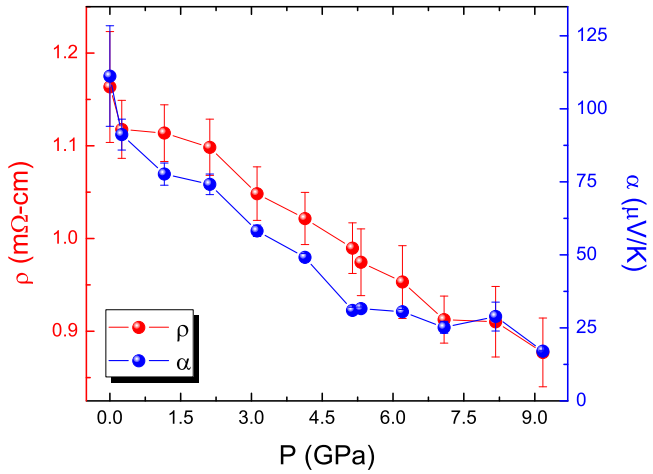

Figure 53 Resistivity and Seebeck Coefficient versus Pressure of $BiSbTe_3$

Resistivity It can be seen, in Figure 53, that the measured resistivity for this material is found to decrease in a nearly linear fashion with pressure. Unfortunately, there are no references to verify this trend, as this appears to be the first time that this material's transport properties have been measured as a function of pressure. It is interesting to note that the structural phase transition does present some evidence in the resistivity, with a temporary halt on the decrease of the resistivity between 7 and 8 GPa. The cause of the initial drop in the resistivity is unknown at this point, but is likely due to contact effects in the ambient setup.

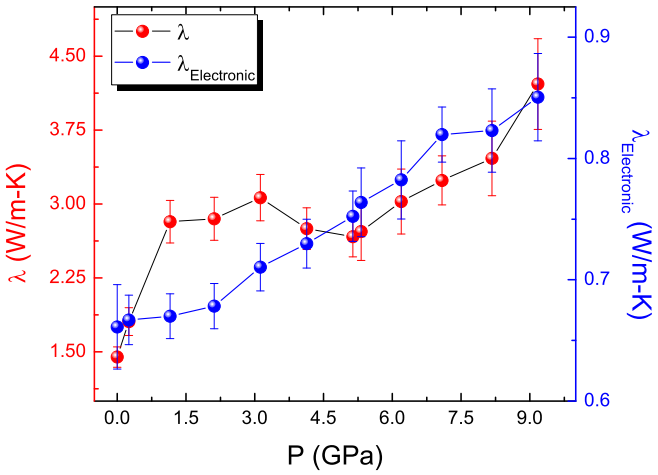

Figure 54 Total and Electronic Thermal Conductivity versus Pressure of $BiSbTe_3$

Table 11 Average Ambient Pressure Transport Properties for $BiSbTe_3$

Property	Measured Value
ρ (mΩ-cm)	1.16 (5)
λ (W/m-K)	1.45 (10)
α (μV/K)	111 (17)

Seebeck Coefficient Evidence of the high pressure structural transition is more prominent in the Seebeck coefficient results, in Figure 53. Inspection of this figure shows three interesting features. First, between ambient and 2 GPa, the trend of the Seebeck coefficient is curved more than the regon between 2 and 5 GPa. The turnaround point is interesting as it corresponds to no particular occurance in the structure of the material, but does correspond to the change in slope of the resistivity. Further, it can be seen that the shoulder in the Seebeck coefficient should be expected, on the basis discussed in the previous chapters, from the trend for the resistivity times the thermal conductivity. It is clearly seen in this plot, Figure 55, that there is a clear jump in the trend for this parameter from 0 - 2 GPa, with a cor-

responding decrease in the value to a minimum around 5 GPa. The second point occurs at 5 GPa, where this property shows a plateau. This is possibly caused by the beginnings of the structure change at 9 GPa, but seems a little too much of a stretch. It is more likely that the changes in this material cause this plateau, as the material does not seem to get significantly worse as a thermoelement with increasing pressure and the thermal conductivity shows a similar trend. Finally, there is a slight jump in this properties trend between 7 and 8 GPa, correlating well with the strcture transition.

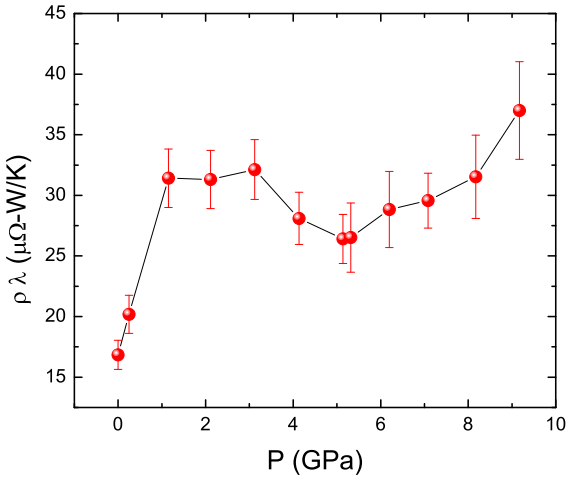

Figure 55 $\rho\lambda$ versus Pressure of $BiSbTe_3$

As with the previous sample, the sign of the Seebeck coefficient here indicates p-type conduction. Further, the effect of pressure on the distance between the valence band and the Fermi energy has been found to decrease at a rate of 3.19 meV/GPa. With the distance between these being 38.5 meV[7] at room pressure, it is likely that the high pressure phases will be found to be metallic. The cross over point for this, assuming the trend continues, would be at nearly 11 GPa.

Thermal Conductivity The thermal conductivity can be seen to shown only slight evidence of the high pressure phase transition, with the change in the pressure trend from 8 to 9 GPa. Of greater interest is the rapid increase at low pressure, occuring prior to 1.5 GPa, followed by the decrease at 4 GPa. It is unclear what the cause for this occurance is at this point. However, the fact that this trend occurs in the total thermal conductivity and not in the electronic suggests that the phonon structure of the material is altered in such a way as to reduce the scattering of phonons. This would suggest that the relaxation time, or the mean free path for the phonons increases dramatically with a small applied pressure.

As with the other samples, the lattice component of the thermal conductivity has been calculated from the measured results and is shown in Figure 56. In this figure, the trend shown in the total thermal conductivity is seen quite clearly. As this shows some interesting phonon dynamics, a fit to the low pressure data is likely to be of no particular use. These results show some interesting and dramatic evidence that has yet to be explained by the current models available.

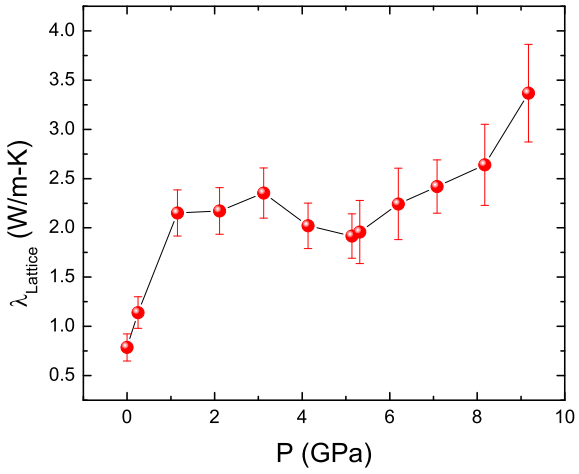

Figure 56 Lattice Thermal Conductivity of $BiSbTe_3$

As with Bi_2Te_3, the effectiveness of this material as a thermoelectric decreases with pressure. Evidence of the thermoelectric feasibility of this material can be seen in Figure 57. However, the interesting physics of the system under pressure merits further investigation of the material properties. The changes in the structure obviously lead to interesting phonon dynamics in the system, as was seen in the thermal conductivity results. This would be beneficial to investigate further. Overall, the high pressure structure of this and the parent materials have demonstrated themselves to become less effective as thermoelectric materials with applied pressure.

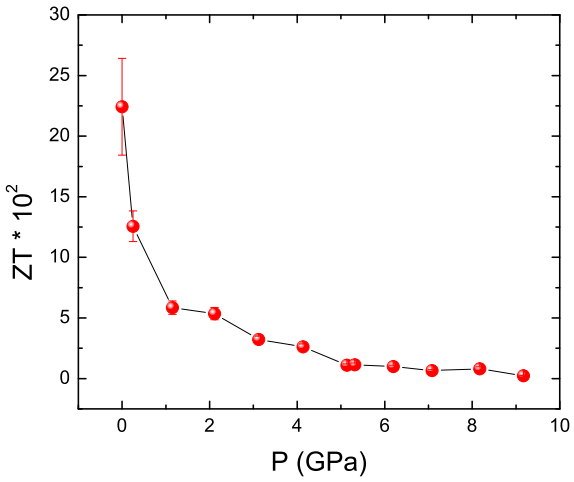

Figure 57 ZT versus Pressure of $BiSbTe_3$

The results of this experiment can be compared with the results from work by Kulbachinskii *et al.* [7], which studied a p-type version of this material doped with gallium. In their work, it is shown that the doping of this material with gallium results in a factor of nearly two increase in the ZT parameter. In addition to this, it can be seen that the p-type doping of $BiSbTe_3$ without any additional dopants

results in a slightly improved ZT for this material. At 300 K, their work measures a ZT for the Ga free sample of nearly 0.4, compared with the 0.225 measured for the undoped version used in this work. As such, it is obvious that doping can be used to greatly improve the effectiveness of this material as a thermoelectric.

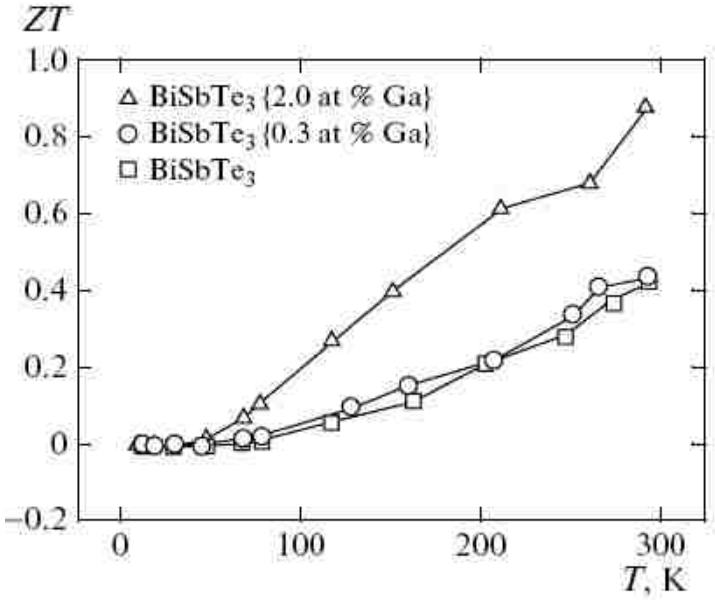

Figure 58 ZT versus Temperature for Doped $BiSbTe_3$[7]

CHAPTER 10

SAMPLE RESULTS : INTE

InTe is a slightly layered compound, where the effects of the weaker bonds between layers is present, but to a lesser degree than in other materials, such as GaTe. This material was chosen due to previous studies regarding similar compounds, In_2Te_3 and the gallium variant of this, as reported by Kurosaki [31]. These materials were demonstrated in Kurosaki's paper to be close to the theoretical limit for the lattice component of the thermal conductivity. This would be a significant result if present in the 1:1 compounds. As such, this material, the gallium variant, and the solid solution between the two will be investigated here.

Heat Capacity

As with the other samples, a pellet of InTe was prepared and cut to the appropriate dimensions, with mass 32.23 mg, for measurement of heat capacity. The heat capacity of this sample was measured in the range from 1.8 K to 300 K, with the resulting data being processed using the Mathematica code previously mentioned. From this fit, it was determined that the Debye temperature for this material was 162 ± 2 K. As with the previous samples, measured values were used for all but the thermal expansion coefficient. In this case, the only available value for the thermal expansion coefficient comes from the Landolt-Bornstein database of materials [76].

Structure Results

Ambient Pressure

InTe crystallizes in the ambient pressure tetragonal structure of space group I4/mcm. The initial unit cell parameters have been verified against data available in the Landolt-Bornstein database[77] and are presented in Table 12. The ambient

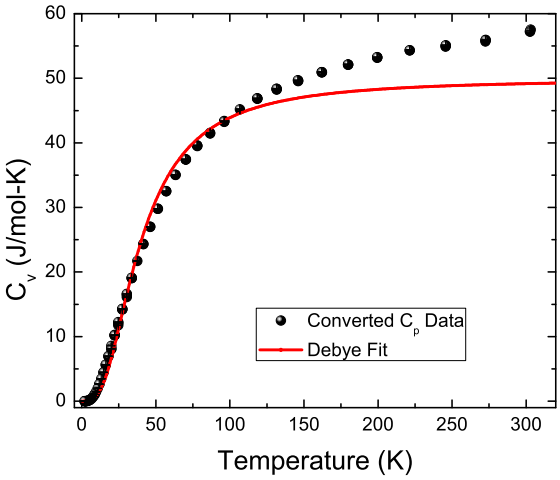

Figure 59 Heat Capacity for InTe

pressure x-ray pattern is shown in Figure 61 with selected peaks marked with their hkl values. A diagram of the ambient pressure structure is shown in Figure 60.

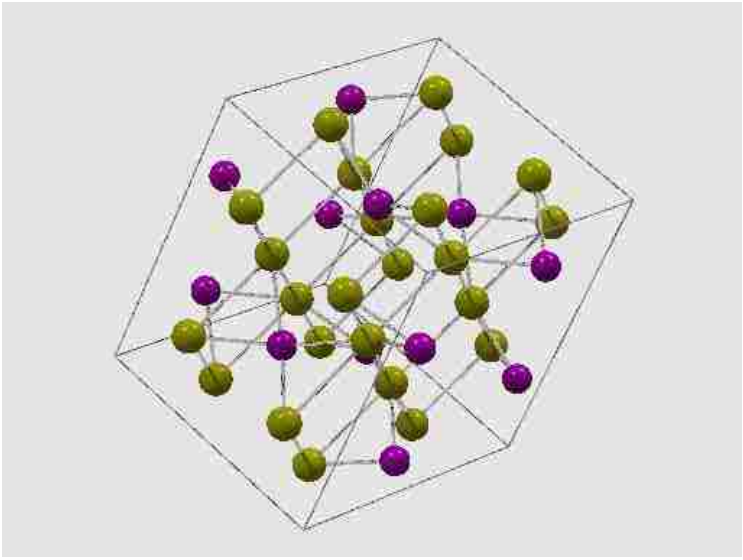

Figure 60 Ambient Structure of InTe (Yellow = In, Purple = Te)

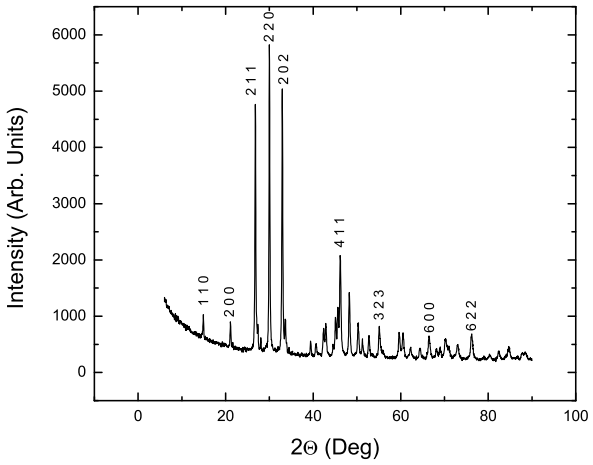

Figure 61 Ambient Pressure X-ray Pattern for InTe

High Pressure

Upon compression, the ambient structure remains until 6.1 GPa, when the structure transforms to a high pressure cubic structure of space group $Fm\bar{3}m$ (225). This structure remains until 13.5 GPa, when the structure transforms to a primitive cubic cell of space croup $Pm\bar{3}m$ (221), which remains until the limit of the experiment (17 GPa). Although there were too few data points taken on the second high pressure structure, equation of state fits have been performed on the ambient and first high pressure phase, resulting in the data presented in Table 12. The equation of state fits and the data taken are shown in Figure 62.

The data obtained here was compared to previous data taken by Chattopadhyay [8]. In their study, they found that the initial phase remained until around 5 GPa, and the second phase remained until about 15 GPa. The results from their data fits present the data shown in Table 13. As can be seen, the data they obtained for the initial phase disagrees rather strongly with the data taken in this study. This can likely be attributed to the fact that, upon inspection of the volume versus pres-

sure fit presented in their paper, there are only three data points available to them for fitting the initial phase, which will yield rather poor statistics for any attempted fit.

Table 12 InTe Structural Parameter Results

Parameter	I4/mcm	$Fm\bar{3}m$
a ($\AA$)	8.436 (2)	5.969 (3)
c ($\AA$)	7.126 (3)	————
V_0 ($\AA^3$)	507.29 (33)	229.73 (8)
B_0 (GPa)	28.68 (54)	66.69 (50)
$B_0^{'}$	4.18 (27)	4.09 (12)
Transition Pressure (GPa)	6.1	13.5

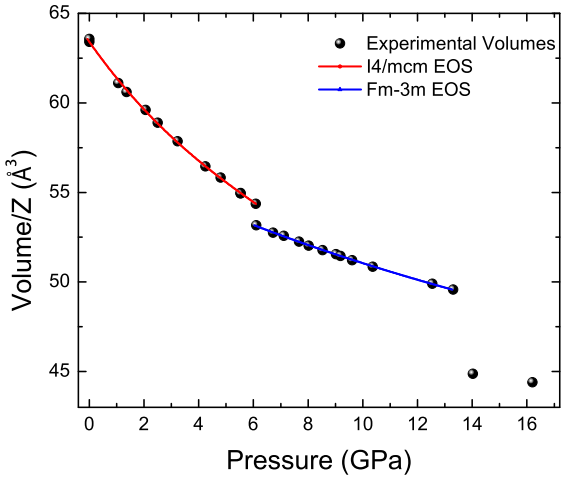

Figure 62 Applied Pressure vs. Cell Volume for InTe

The second phase transition point and bulk modulus agree. However, a discrepancy is again seen in the pressure derivative of the bulk modulus. This is likely due to the fact that the authors were using a first-order Birch equation of state, which fixes the value of this pressure derivative to a specified value. In ad-

Table 13 InTe Structural Parameter Results from Chattopadhyay[8]

Parameter	I4/mcm	$Fm\bar{3}m$	$Pm\bar{3}m$
B_0 (GPa)	46.5 (5)	69.7 (11)	90.2 (25)
B_0'	2.3	2.2	2.3
Transition Pressure (GPa)	5	15	

dition to this, the authors also obtained the second high pressure structure, and as their experiment went to 34 GPa, were able to obtain values for this high pressure phase's bulk modulus and pressure derivative. As the previous values are likely off for the pressure derivative, this sample should be investigated further in the high pressure regime to attempt a better fit of the high pressure data.

In addition to this, there is no evidence from the structure data that this material undergoes an ETT while in the ambient structure. A plot of the pertinent equations of state is shown in Figure 63. It is clear in this figure that the data can be fit to a single line for the entirety of the region plotted.

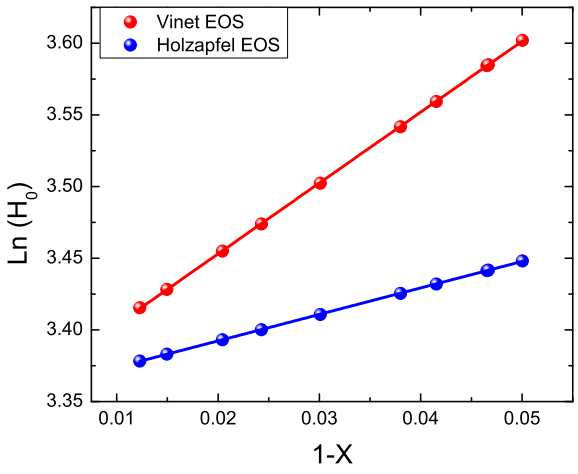

Figure 63 ETT Equation of State Plot for InTe

High Pressure Transport Properties

The results of the high pressure transport measurements are shown in Figures 64 and 65. The measured ambient pressure values are reported in Table 14. These values have been compared with references and show good agreement with Parlak *et al.* [78] (Resistivity) and Spitzer *et al.* [79] (Thermal Conductivity) under ambient conditions. In Spitzers report, the thermal conductivity is presented as between 1.7 [80]and 0.6 W/m-K, although it is not explained in his paper why the discrepancy arises. Unfortuantely, the referenced paper for the latter result was unpublished at the time that Spitzer published his work. In addition, Guseinov *et al.* [80] does not describe the measurement system used for the former value. Regardless, the measured value here is in the range of values reported previously.

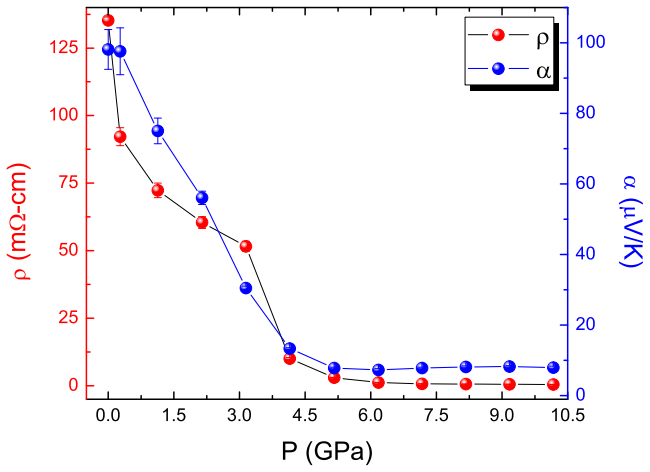

Figure 64 Resistivity and Seebeck Coefficient versus Pressure of InTe

Resistivity The resistivity for InTe is seen, with pressure, to decrease dramatically in the range from 0 to 4 GPa. At 4 GPa, the resistivity makes a sudden discontinuous drop, suggesting the onset of the structural phase transition. The

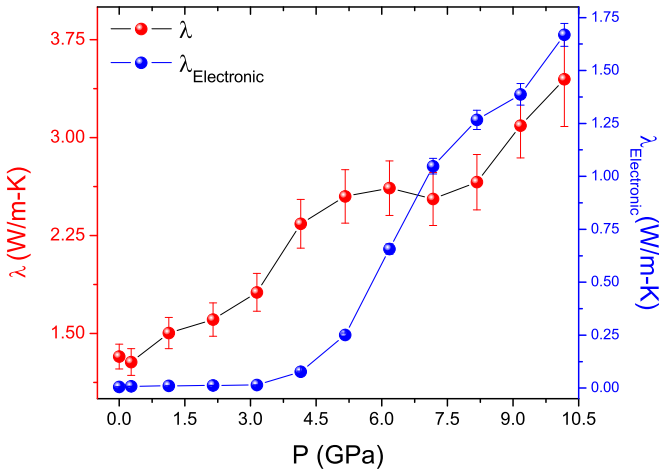

Figure 65 Total and Electronic Thermal Conductivity versus Pressure of InTe

Table 14 Average Ambient Pressure Transport Properties for InTe

Property	Measured Value
ρ (mΩ-m)	1.35 (1)
λ (W/m-K)	1.32 (9)
α (μV/K)	98 (6)

structural phase transition has been reported to result in a metallic high pressure phase of the material by Chattopadhyay *et al.* [8].

Seebeck Coefficient In contrast with the resistivity, the Seebeck coefficient does not show any dramatic evidence of the structural phase transition. It does, however, agree with the supposition of a metallic high pressure phase. Since the Seebeck coefficient drops to around 10 μV/K, which is near the values of transition metals. This suggests that the electronic structure becomes more like the transition metals, such as Ni, but with a strong contribution to the conduction from electrons. This is demonstrated by the sign of the Seebeck coefficient, as electrons produce a positive coefficient and holes will produce a negative coefficient. As with the pre-

vious samples, the product of the electrical resistivity and thermal conductivity can give evidence to where anomalies can be expected in the Seebeck coefficient. The plot of this is shown in Figure 66.

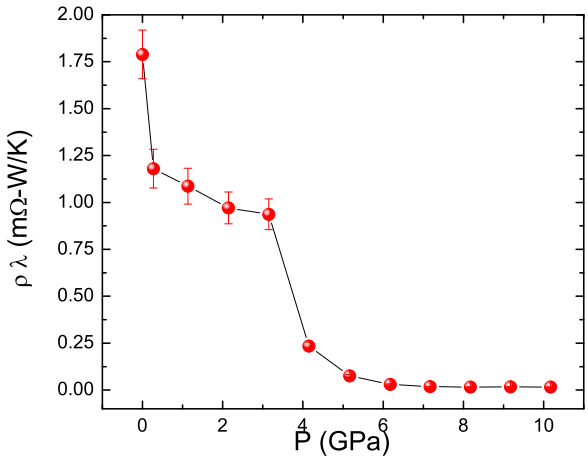

Figure 66 $\rho\lambda$ versus Pressure of InTe

It is interesting to note that the sharp drop present in ρ does not seem to effect the trend of the Seebeck coefficient in this case. This would suggest that the phonon structure is compensating for the changes in the electrical structure. As such, the coupling between the two is obviously stronger in this case than with some of the other samples studied here and elsewhere. In addition to this information, the slope of the Seebeck coefficient suggests that the distance between the valence band and the Fermi level is decreasing at a rate of 6.22 meV/GPa.

Thermal Conductivity For the thermal conductivity of this material, the measured total thermal conductivity and the electronic component, from equation 2.11, are shown in Figure 65. It is seen in this plot that the overall thermal conduction increases steadily until 3 GPa. At this point, there appears to be a change in the phonon dynamic of the system causing a rapid rise, relative to the previous rate.

There is evidence present in this figure of the high pressure phase transition, as the trend for the thermal conductivity turns over and briefly decreases between 6-7 GPa. It is possible that this change is due to the transition of the system from semi-conductive behavior to metallic behavior, as the computed electronic component has rapidly risen to a sizeable fraction of the overall thermal conduction.

The lattice thermal conductivity for this material, shown in Figure 67, shows some interesting dynamics also. The phase transition is obvious in the lattice conductivity again, with a sharp drop on the reorientation of the structure. A linear fit was done on $ln(\lambda_{lat})$ versus P in the range from 0 to 4 GPa, with the resulting slope being 0.165 $\pm$ 0.016 W/m-K-GPa. From Hofmeister's [22] theory, the value of the slope for this material should be between 0.139 (n=4) and 0.209 (n=6). This material's value lies somewhere in the intermediate range, but shows reasonable agreement with the theory.

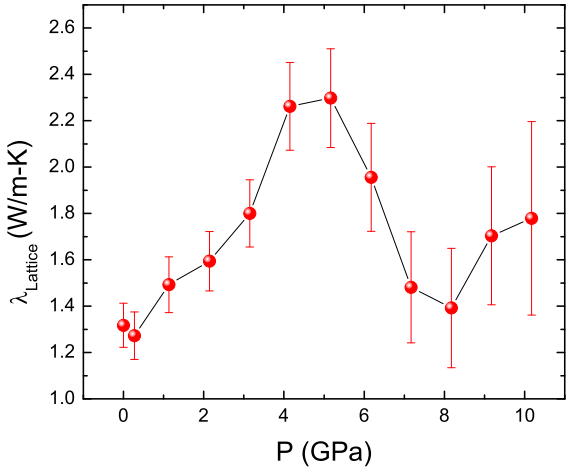

Figure 67 Lattice Thermal Conductivity of InTe

Despite the decrease of the Seebeck Coefficient and the increase in the thermal conductivity, the drop in the resistivity has, for this material, shown to compensate enough to produce a slight increase in the ZT parameter for this material at low pressures. What is of greater interest here is the relative stability of the ZT parameter once the high pressure metallic phase is reached. As can be seen in Figure 68, the phase transition appears to result in the minimum value for the ZT parameter in the measured pressure range. It is interesting that the dynamics of this structural phase transition appear to cause the extreme reduction in the thermoelectric ability of this material. Regardless of the thermoelectric efficiency of this material, it would be useful to further investigate the properties in an attempt to understand the interesting dynamics present with increasing pressure.

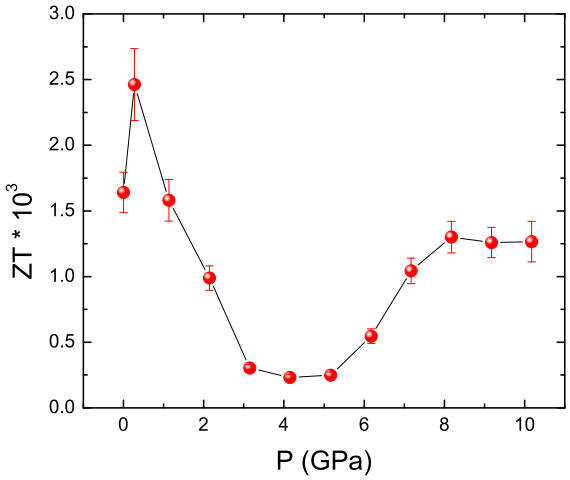

Figure 68 ZT versus Pressure of InTe

CHAPTER 11

SAMPLE RESULTS : GATE

As has already been mentioned, the study of this sample is driven by the remarkably low lattice thermal conductivity reported previously in the 2:3 compounds of these elements. It was further noted that the Gallium variant exhibited the lower of the two thermal conductivities. This would initally suggest that the Gallium variant of the 1:1 compounds would also exhibit the more interesting properties in the pair. This is also considered to be true to the more extreme level of layering present in this material over the previous one. As such, this chapter will discuss the various measurements made on this sample and discuss the results.

Ambient Pressure Heat Capacity

A small amount, of mass 18.32 mg, of the sample was pelletized and prepared in the manner described in the experimental details section for a heat capacity measurement. This measurement was performed in the temperature range from 1.8 K to 300 K. The results of a simple Debye model fit resulted in a Debye temperature of 240 $\pm$ 3 K. The thermal expansion data used to convert to constant volume heat capacity was obtained from the Landolt-Bornstein database [77]. In addition, this plot shows a Debye fit using the Debye temperature reported in work by Aydinli *et al.* [81] (Θ_D = 265 K).

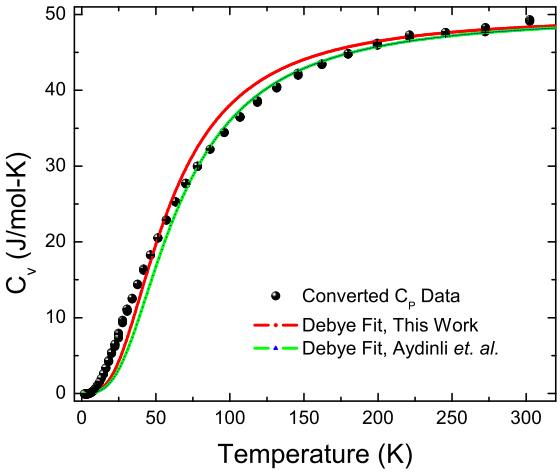

Figure 69 Heat Capacity and Basic fits for GaTe

Structure Results

Ambient Pressure

The GaTe sample was prepared by the synthesis method described in the experimental details chapter. The resulting sample proved to be the reported [76] monoclinic structure, B2/m (12), with the cell parameters reported in Table 15. The cell parameters were refined using reference data from [76] and MDI's Jade. A representation of the unit cell structure is shown in Figure 70. In this figure, the red atoms are the tellurium and the green are the gallium atoms.

High Pressure

The high pressure structure of GaTe was probed in the pressure range from ambient to 18 GPa. The initial structure, reported above, was found to remain until around 7 GPa, where the x-ray patterns began to degrade in quality. From 7 GPa until 15 GPa, the measured structure remained in an intermediate state, to which no consistent structure could be ascribed. At 15 GPa, the structure became

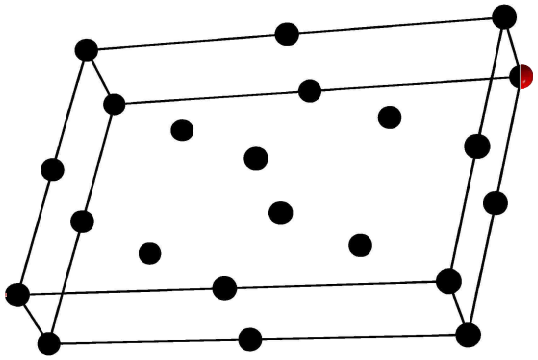

Figure 70 Ambient Structure for GaTe (Green = Ga, Red = Te)

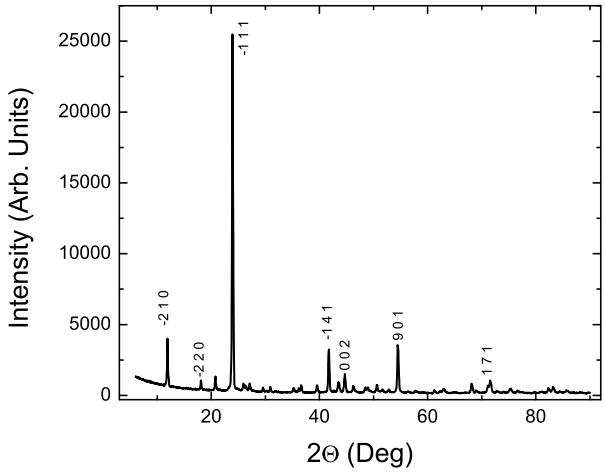

Figure 71 Ambient Pattern for GaTe

a cubic structure with a few possibilities for the resulting space group. For the purposes of this experiment, the structure was fit using the group $Fm\bar{3}m$ (225). With decompression, the high pressure cubic structure remains until around 3 GPa, where the diffraction patterns become amorphous with very low or nonexistent diffraction intensities.

The data on this sample for both the ambient and high pressure phase are presented in Table 15. The equations of state and measured data are shown in Figure

Table 15 GaTe Structural Parameter Results

Parameter	B2/m	$Fm\bar{3}m$
a ($\AA$)	17.228 (8)	5.502 (7)
b ($\AA$)	10.391 (4)	————
c ($\AA$)	4.036 (2)	————
γ (Deg)	104.63 (3)	————
V_0 ($\AA^3$)	698.94 (42)	204.4 (14)
B_0 (GPa)	36.13 (37)	43.0 (23)
B_0'	4.45 (12)	5.41 (61)
Transition Pressure (GPa)	7.05	N/A

72. In this figure, the red points are obtained upon decompression, with the red and blue lines representing the equation of state fits to the data, resulting from EOSFit.

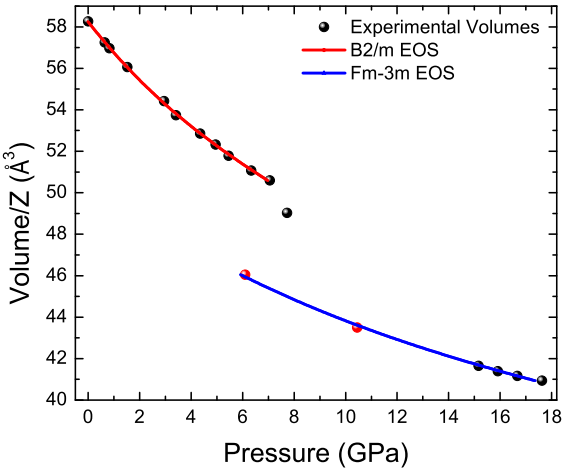

Figure 72 Applied Pressure vs. Cell Volume for GaTe (Red = Decompression))

In comparing this with previous works at high pressure on this material, it was found by Schwarz *et al.* [82] that the sample used for his study transformed from the ambient monoclinic to a high pressure cubic structure at approximately 10 GPa. His report also mentions that they were unable to index the patterns in

the range from 8 to 10 GPa, which does correspond to the data taken in this experiment. However, the region for which the data taken here is unindexable extends to approximately 15 GPa. In addition, the values obtained for this sample's bulk modulus agrees well with both values quoted in Schwarz's paper. The pressure derivative of the bulk modulus measured here is somewhat less than the data they reported, which could be due to the difference between the equation of state used in each case, as they fitted using a third order Murnaghan equation of state. The values measured for this high pressure phase differ somewhat, with the reported value for the bulk modulus being 60 GPa, as opposed to the 43 GPa measured here. It is also peculiar in this case as the transitions for this sample result in a higher degree of symmetry, whereas it is more typical in high pressure studies for materials to become less symmetric with pressure.

In contrast with the structure results from InTe, GaTe does show evidence of a topological transition in the structure, occuring at nearly 1.1 GPa. This can be seen clearly in Figure 73.

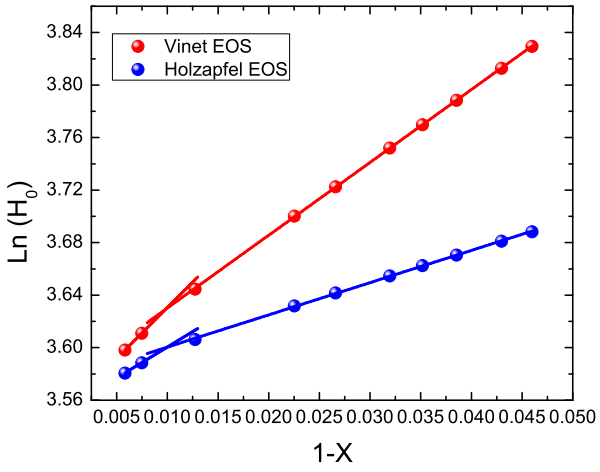

Figure 73 ETT Equation of State Plot for GaTe

High Pressure Transport Properties

The results of the high pressure transport measurements are shown in Figures 74 and 75. The measured ambient pressure values are reported in Table 16. These values have been checked against literature values and found to agree well with previous reports from Al-Ghamdi *et al.* [83] (Seebeck Coefficient), Mancini *et al.* [84], Manfredotti *et al.* [85], and Milne *et al.* [86] (Resistivity), and Spitzer *et al.* [79] (Thermal Conductivity). In the thermal conductivity, Spitzer lists values for both the parallel and perpendicular directions to the c axis, with the corresponding thermal conductivities being 1.4 W/m-K and 8.7 W/m-K. The anisotropy in this property is prononuced and, in this case, the measured ambient value is closer to the parallel direction. It is unclear at this point why the pelletized sample would exhibit a thermal conductivity more similar to that along the c-axis, but it does seem to suggest some interesting interactions present in the material used for this study.

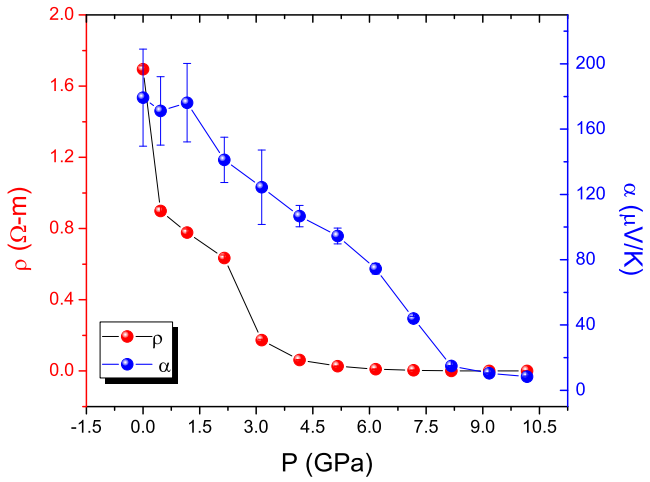

Figure 74 Resistivity and Seebeck Coefficient versus Pressure of GaTe

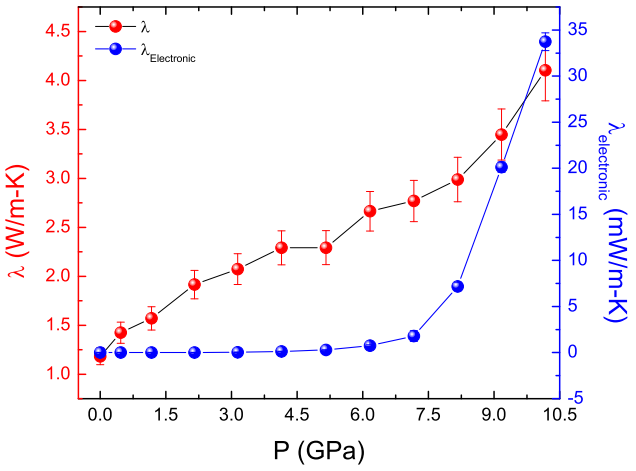

Figure 75 Total and Electronic Thermal Conductivity versus Pressure of GaTe

Table 16 Average Ambient Pressure Transport Properties for GaTe

Property	Measured Value
ρ (Ω-m)	1.69 (1)
λ (W/m-K)	1.18 (8)
α (μV/K)	179 (30)

Resistivity The resistivity for GaTe with pressure shows similar trends to that from InTe, with a sharp decrease occuring at around 4 GPa, with a steep drop with the inital application of pressure. In both cases, there is no structure transition that corresponds with this. It is postulated by Schwarz *et al.* [82], based on reflectivity data, that the loss of structure and the high pressure cubic phase result in a metallic material. This is supported by the resistivity data taken here.

Seebeck Coefficient For the Seebeck coefficient, the initial pressurization of the material shows little effect. With increasing pressure, the decreasing trend correlates well with the decrease in the electrical resistivity of the material. The change in slope of the Seebeck coefficient upon the transition to the mixed phase suggests,

in correlation with the results from InTe, that this material exhibits a similarity with the transition metals in the high pressure phase. An inspection of the plot of the product of the resistivity and thermal conductivity show that this material would be expected to display anomalies in the Seebeck coefficient between 2 and 3 GPa and under the inital pressurization. Although it is not a rapid decrease in the Seebeck coefficient, the inital plateau of this parameter with pressure does correlate with this, as does the beginning of the decrease with pressure at 3 GPa.

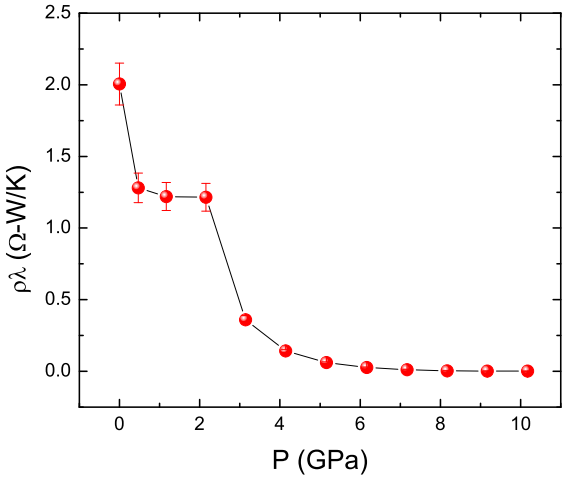

Figure 76 $\rho\lambda$ versus Pressure of GaTe

It is particularly interesting that the plateau at low pressures does correlate well with the anomaly presented earlier in the ETT plot for this material. Further, the trend for GaTe with pressure would suggest that the distance between the valence band and the Fermi level is decreasing at a rate of 5.5 meV/GPa. This makes the sudden decrease in the resistivity at 3 GPa even more interesting, as this suggests that the structure transition may be driven by changes in the band structure of the material, in a similar manner to InTe.

Thermal Conductivity The thermal conductivity of this material shows no remarkable features, but increases with pressure up to 8 GPa, where the slope of the increase changes. This increase in slope corresonds well with the increase in the electronic thermal conductivity (as calculated from equation 2.11). This would suggest that, as with InTe, the high pressure phase will exhibit metallic properties. Further, the lack of significant features in the thermal conductivity suggests that the phonon structure of this material is either undergoing a continuous change, as opposed to an abrupt change at the structure transition, or is not effected at all by the increasing pressure (aside from the increase in relaxation time).

The lattice component of the thermal conductivity for this material shows no obvious jumps or drops corresponding to the structure transition in this material, as shown in Figure 77. The log plot of λ_{lat} versus P shows a dramatic slope change at 2 GPa, which prevents fitting a single line to all the data. For the data points below the slope change, it was found that the rate of increase was 0.198 ± 0.022 W/m-K-GPa. Above 2 GPa, the slope was found to become 0.089 ± 0.007 W/m-K-GPa. From Hofmeister's[22] theory, this material would be expected to show a slope between 0.111 and 0.166 W/m-K/GPa. As such, this material shows a slightly larger trend than would be expected from the theory below 2 GPa, and a slightly smaller one above. This could be due to the reported anisotropy in the thermal conductivity or is possibly caused by the layering of the structure, but the exact cause will require further investigation.

Conclusions

It can be seen quite clearly from the previous results that GaTe is not expected to be a useful thermoelectric material. This is further emphasized by the plot of ZT versus pressure in Figure 78. However, it is interesting to note that, in contrast with the previous samples, the ZT increases in this material on compression until

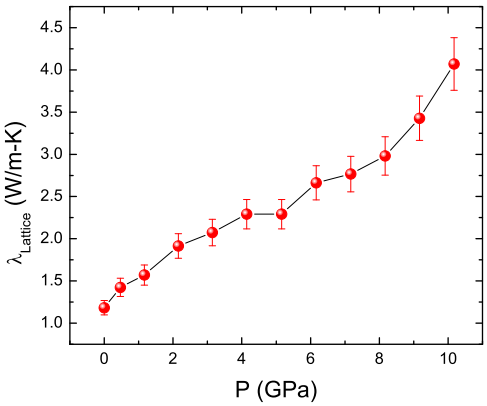

Figure 77 Lattice Thermal Conductivity of GaTe

the ambient structure is lost, with a factor of nearly 14 increase in the efficiency of this material. As such, it is plausible to conclude that structures that exhibit a mixed phase structure might be considered to be more effective thermoelectric materials. Despite this, the efficiency of GaTe as a thermoelectric is 3 orders of magnitude below that of Bi_2Te_3.

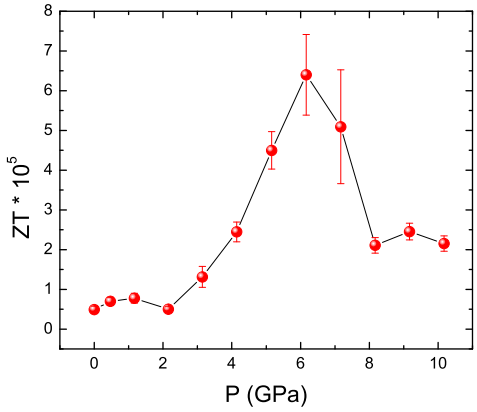

Figure 78 ZT versus Pressure of GaTe

CHAPTER 12

SAMPLE RESULTS : $INGATE_2$

The final sample studied in this work is the solid solution between the previous two materials. As the two parent compounds exhibit interesting transport dynamics, it would be expected that this material should also exhibit some interesting behavior with the application of pressure. In addition to this, this sample is the least investigated of all the materials presented in this document, with no pressure studies being performed at all. As such, this study makes the first time that this material has been investigated in this much depth.

Ambient Pressure Heat Capacity

A sample of mass 30.40 mg was prepared and measured using the PPMS system, as described in the experimental details section. This sample was measured in the range from 1.8 K to 300 K , with the data then processed using the aforementioned Mathematica code. This data produced a fit with a Debye temperature of 173 ± 2 K. In this case, this is a very rough estimate as there is no available thermal expansion data for this sample, so the fit was performed to the constant pressure heat capacity.

Structure Determination

Ambient Pressure

This material was synthesized using the procedure described in the experimental details chapter, with the resulting sample found to be the reported tetragonal structure, I4/mcm (140), with the cell parameters reported in Table 17. The cell parameters were refined using reference data from Deiseroth *et al.* [87] and MDI's Jade [32]. A representation of the unit cell structure is shown in Figure 80. In this

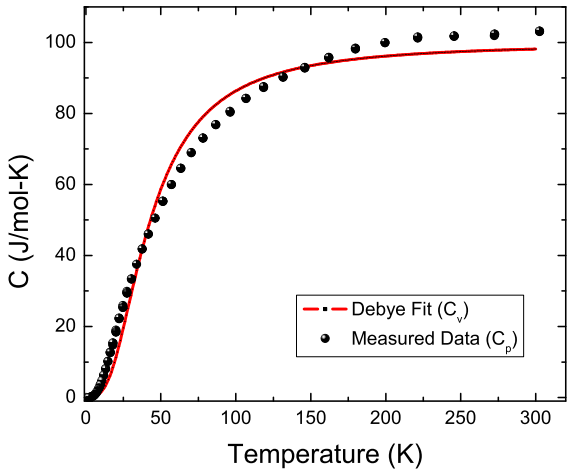

Figure 79 Heat Capacity and Basic fits for $InGaTe_2$

figure, the purple atoms are the tellurium, green is gallium, and yellow is indium. For this material, Vegard's law cannot be applied due to the structural difference between the two parent compounds.

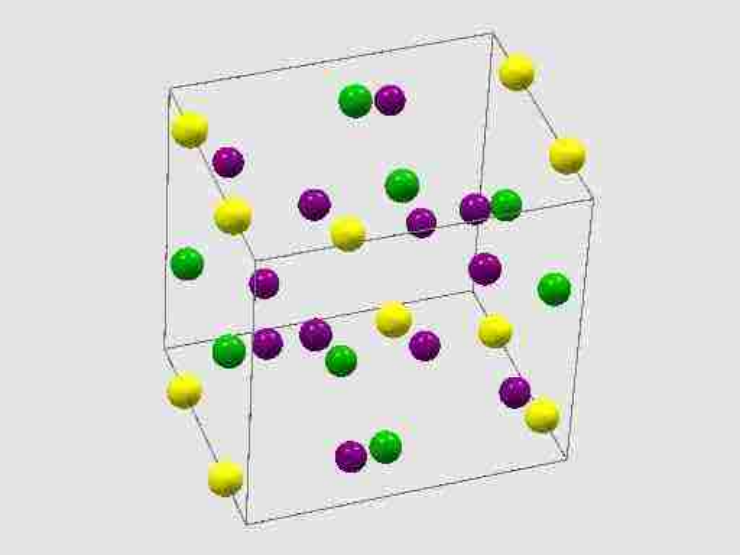

Figure 80 Ambient Structure for $InGaTe_2$ (Yellow=In, Green=Ga, Purple=Te)

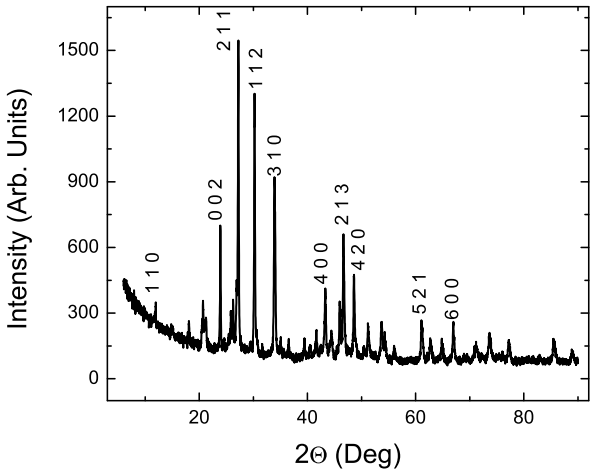

Figure 81 Ambient Pattern for $InGaTe_2$

High Pressure

For the high pressure structure, the sample retained its ambient pressure structure up to 9.5 GPa. At this point the sample undergoes a relatively quick transition to a slightly different tetragonal structure, of space group I4cm (108). This structure retains the original formula units per unit cell and remains until 13 GPa. The structure then changes to a new high pressure monoclinic phase of space group P21/c [b-unique] (14), which remains until the limit of the experiment performed. A summary of the results of the equation of state fits for this sample are presented in Table 17 with the equations of state plotted along with the data in Figure 82. No comparison of this data with previous work can be done as, at the time of writing, there is no published work available for comparison with.

In contrast with the parent material InTe, this solid solution exhibits structural behavior more akin to the GaTe compound, suggesting that the dynamics involving Ga dominate the material. This can be seen in the plots relating to the ETT's, as presented for the previous materials. In this material, it is easily seen that the

Table 17 $InGaTe_2$ Structural Parameter Results

Parameter	I4/mcm	I4cm	P21/c (b-unique)
a ($\AA$)	8.391 (1)	7.618 (3)	6.73 (4)
b ($\AA$)	————	————	3.575 (5)
c ($\AA$)	6.854 (2)	6.566 (4)	5.36 (2)
β (Deg)	————	————	137.54 (24)
V_0 ($\AA^3$)	483.01 (57)	457.3 (13)	111.36 (18)
B_0 (GPa)	23.97 (56)	35.7 (12)	46.33 (53)
B_0'	4.28 (22)	4.03 (29)	2.01 (5)
Transition Pressure (GPa)	9.46	13.11	————

equations of state, shown in Figure 83, suggest that there is an anomaly occuring at $\approx$ 1.5 GPa.

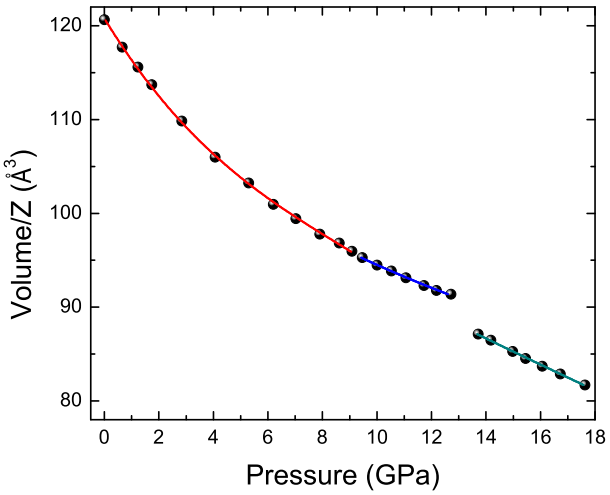

Figure 82 Applied Pressure vs. Cell Volume for $InGaTe_2$

High Pressure Transport Properties

The results of the high pressure transport measurements are shown in Figures 84 and 85. The measured ambient pressure values are reported in Table 18. These

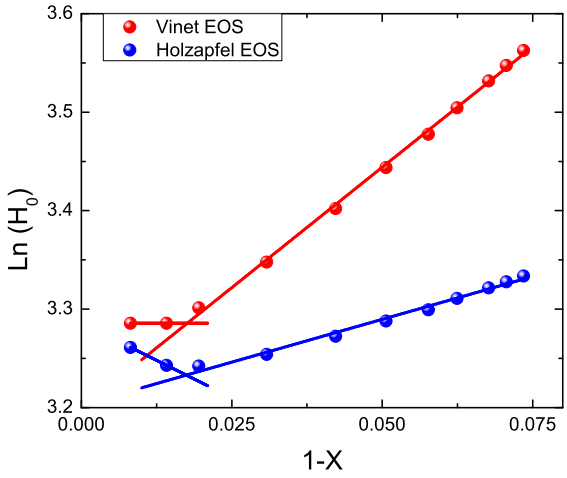

Figure 83 ETT Equation of State Plot for $InGaTe_2$

values have been found to be in good agreement with Gojaev *et al.* [88] (Resistivity) and Guseinov *et al.* [89] (Thermal Conductivity) under ambient conditions.

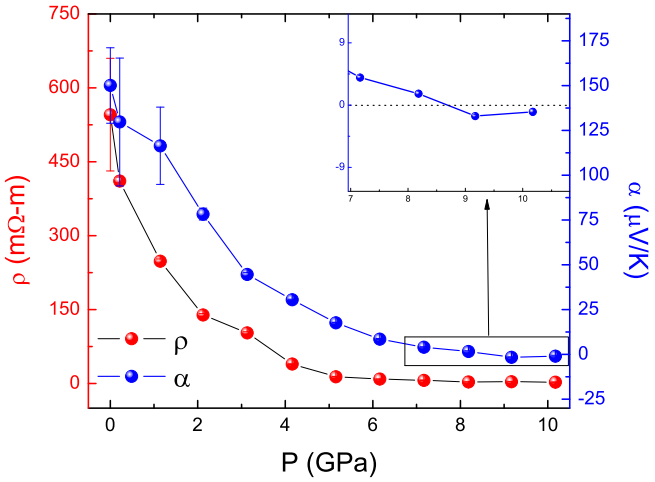

Figure 84 Resistivity and Seebeck Coefficient versus Pressure of $InGaTe_2$

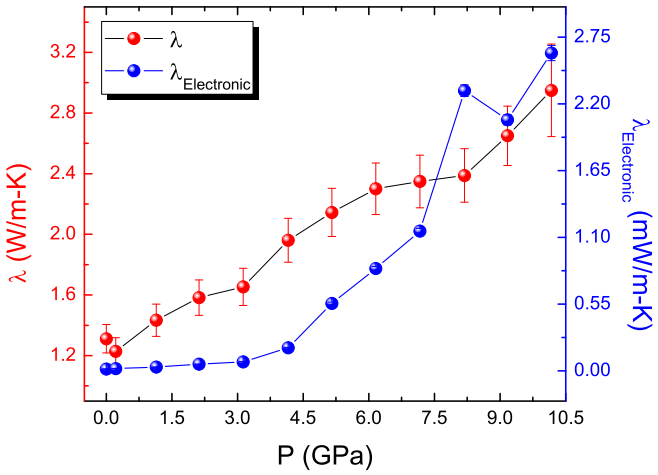

Figure 85 Total and Electronic Thermal Conductivity versus Pressure of $InGaTe_2$

Table 18 Average Ambient Pressure Transport Properties for $InGaTe_2$

Property	Measured Value
ρ (Ω-m)	0.54 (11)
λ (W/m-K)	1.31 (9)
α (μV/K)	150 (21)

Resistivity The resistivity, as measured here, displays a rather large error on the ambient value of the resistivity. This is possibly due to contact issues between the thermocouple, the conducting epoxy used to make the connection, and the sample. This effect was found to be unrelated to any specific type of epoxy, as the usual silver epoxy used with the previous samples was replaced with a graphitic conductive paste for the second sample. This did not change the magnitude of the variation in the resistance of this material. It is also possible that there is some grain boundary effect in this material that could cause this. Further work will need to be done on this material to determine what the cause of this is.

The pressure trend for this material shows a small shoulder in the resistivity

occuring at 3 GPa. It is possible that this could be due to the structure anomaly, but this is unclear at this point. There is evidence of the structural transition occuring, which is more evident in the electronic component of the thermal conductivity, discussed below.

Seebeck Coefficient The Seebeck coefficient for this material shows a downward trend, in addition to the sign change for the 9 and 10 GPa data points. This would correspond to a change in majority carrier in the system from electrons to holes. However, the magnitude of the negative value is very small (-0.9 μV/K @ 10 GPa). This suggests that the effect of pressure on this materials is actually forcing the Fermi surface to cross the boundary between increasing area and decreasing area, as discussed in the theoretical chapter on this property. This is of particular interest, as there are not many reports of materials undergoing this change in the Seebeck coefficient with pressure.

In contrast with the parent materials, this material does not show any peculiarities in the plot of the product of electrical resistivity with thermal conductivity besides the shoulder at 3 GPa. Since this shows no anomalies, this would suggest either that changes in the other transport properties compensate for each other, or that there is not a significant alteration in either one. The plot of this quantity is shown in Figure 86.

As with GaTe, the slight discontinuity in this property of the material correlates well with the anomaly in the ETT plot in the previous section. This is particularly interesting, as there is no obvious change in the resistivity of the material that correlates with this. From the slope of the Seebeck coefficient, it can be found that the distance between the Fermi energy and the valence band in this material is expected to decrease at a rate of 8.39 meV/GPa for pressures below 3 GPa and 2.12 meV/GPa for pressures above 3 GPa.

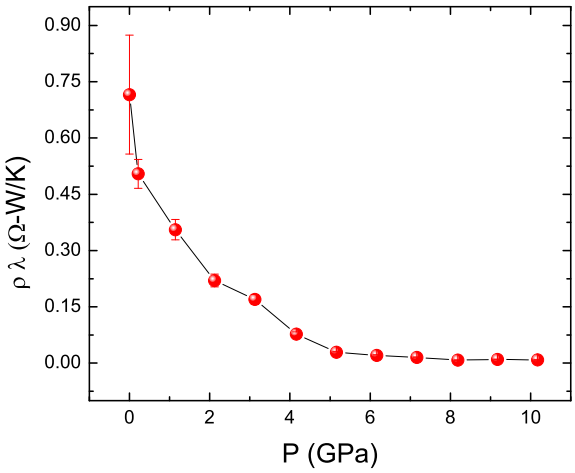

Figure 86 $\rho\lambda$ versus Pressure of $InGaTe_2$

Thermal Conductivity The plot of the thermal conductivity, shown in Figure 85, demonstrates that the phonon structure of this material is not undergoing any significant changes due to the phase transition at 9 GPa. Due to the similarity between the ambient phase and the high pressure phase, an obvious transition between the two structures was not expected to appear in the trend of this property. It is interesting to note in the electronic thermal conductivity, as calculated from equation 2.11, that the electronic structure of this material shows a small change in the trend occuring at 9 GPa, corresponding to this structure transition. This is of particular interest as this pressure is also where the Seebeck coefficient changes sign. Although there is not a dramatic change in the resistivity at this point, the transition shows direct evidence on the electronic structure through the electronic thermal conductivity. As this feature corresponds to the majority carrier becoming holes over electrons, it is interesting to see that the holes initially conduct less heat than the electrons do.

As with the previous results, the lattice component of the thermal conductivity for $InGaTe_2$ shows a greater resemblance to GaTe than to InTe, as shown in Figure

87. Although it is possible that there is a slope change correlating with the structure transition present here, the change would be so minute that it is nearly impossible to see, except at the very highest pressure measured. As such, the phonon dynamics appear to be unaffected by the structure transition, showing a linear trend to the highest pressure. From this trend, the slope of the log plot was found to be 0.076 ± 0.005 W/m-K-GPa. From Hofmeister's [22] theory, the slope for this material should be in the range from 0.167 (n=4) to 0.250 (n=6) W/m-K-GPa. Thus, this sample shows lattice pressure trends similar to InTe, with the measured trend being about half of the theoretical approximation. This is in contrast to the previous properties, which show the strong influence of the Gallium present in the structure.

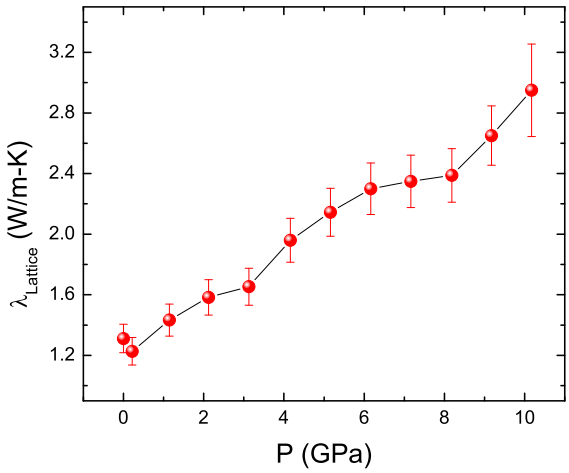

Figure 87 Lattice Thermal Conductivity for $InGaTe_2$

Conclusions

As can be seen in Figure 88, the ZT parameter show that this material is not a useful thermoelectric. However, the shoulder in the Seebeck coefficient at 3 GPa

is seen to create a maxima in the thermoelectric performance. As this could be an electronic topological transition, it would be of particular use to investigate this phenomena further to learn if it can be used to improve the performance of thermoelectrics with a higher ZT parameter. It is also unclear why the ZT parameter plateaus between 3 and 5 GPa.

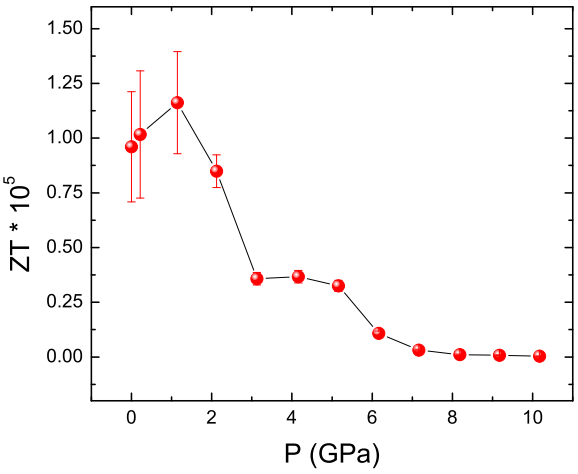

Figure 88 ZT versus Pressure of $InGaTe_2$

CHAPTER 13

CONCLUSIONS

One of the original goals of this work was to establish a measurement system for the determination of material transport properties under pressure. This was to include the high pressure measurement of electrical resistivity, thermal conductivity, and Seebeck coefficient, so that the results could be compared to structure results obtained from other experiments. The result of this is the measurement system described in the previous chapters. The development, testing, and use of the system described herein has revealed its ability to quantify the desired material properties in the pressure range from ambient to 10 GPa. This was checked with calibration samples of zinc, almandine garnet, and nickel, with the results being in good agreement with previously published results.

The measurement of material transport properties under pressure has proven to be a useful, if under applied, tool for studying the dynamics of a system with small changes in structure. As such, the system developed has been used to measure the transport properties of several potential and established thermoelectric materials. This effort to test these materials under pressure is driven by a fundamental need for better information regarding the changes of material properties with changes in structure. This correlation will likely assist in the development and understanding of thermoelectric materials on a more fundamental level and provide the necessary basis to predict what materials will likely show better properties.

This study began with the investigation of the established thermoelectric materials, of the form A_2Te_3 (A = Bi, Sb, $Bi_{0.5}Sb_{0.5}$). This study showed that, for these materials, the application of pressure results in two structure changes. The first transforms the inital $R\overline{3}m$ structure to the orthorhombic structure I222. In addition to the structure change, there is an anomaly present in particular forms of the

equation of state for the parent compounds around 3 GPa. This particular anomaly is consistent with previous reports regarding electronic topological transitions in these materials. The solid solution sample, in constrast, does not exhibit evidence of this anomaly. When compared with the transport measurement results, there were some interesting features.

In Bi_2Te_3, the resistivity decreased steadily with the increase of pressure, with slight evidence of the structure transition. The thermal conductivity shows evidence of the structure change also, as exhibited by the decrease in this parameter at 8 GPa. The Seebeck coefficient, on the other hand, shows no direct evidence of the structure change, but does respond to the anomaly present in the structure at 3 GPa. In addition to this, conversion of the resistivity to the electronic component of the thermal conductivity results in a dramatic increase in the theoretical contribution of electrons to the thermal conduction. Rising by a factor of nearly 7 over this pressure range, this indicated strongly that this material was tending towards metallic behavior with the applied pressure.

In Sb_2Te_3, the resistivity shows a steady downward trend until 9 GPa, when there was a sharp rise in the value of the resistivity, corresponding to the structure change. The thermal conductivity was, however, unchanged by the structure transition. The Seebeck coefficient also shows evidence of the transition, in a more drastic manner. As such, the structure change in this material is likely driven not by lattice dynamics, but by the electronic structure of the material. As with the previous sample, this material shows evidence of a trend towards metallic behavior, but the trend is not quite as fast as that present in the Bi sample, with the magnitude of the increase of the electronic component of the thermal conductivity changing by a factor of 6.

The solid solution shows the least drastic response to the applied pressure of all three of these materials. The resistivity and Seebeck coefficient both show nearly

linear trends with applied pressure. The Seebeck coefficient does show a slight increase corresponding to the measured structural transition. The thermal conductivity shows a rapid rise with applied pressure in the beginning of the pressure graph. With further increases in pressure, the thermal condcutivity is found to decrease slightly and then recover a linear trend until the structure changes at 9 GPa. In this case, the linear decrease in the resistivity suggests that this material remains semiconducting over the entirety of the pressure range and shows no particular signature of a metallic high pressure phase, in contrast with the previous two samples.

From these established materials, the study moved into samples that have a lack of high pressure reference data. These materials, of the from ATe (A = Ga, In, $Ga_{0.5}In_{0.5}$), are of particular interest due to the low dimensionality of the crystal structures. The layered nature of the material is currently considered to be one of the interesting and useful properties for potential thermoelectric materials. The structure measurements for these three materials were presented and shown to be different for each one. In GaTe, the ambient monoclinic B2/m structure was found to enter an unindexible mixed phase at 7 GPa. This relaxed at 15 GPa into a cubic $Fm\overline{3}m$ structure that remained until the limit of the experiment. In InTe, the ambient tetragonal I4/mcm structure was found to remain until 6 GPa, where it transitions to the same cubic structure as GaTe. There is further evidence that this material transitions again at 15 GPa to a primitive version of the previous cubic structure. The solid solution was found to transform from the ambient tetragonal I4/mcm structure to a slightly different tetragonal structure at 8 GPa. This structure remained until 13 GPa, where the system transformed to a monoclinic P21/c structure.

For InTe, the resistivity was found to decrease rapidly until 3 GPa. At this point, the resistivity made a sudden drop and continued to decrease with applied

pressure. The Seebeck coefficient exhibited a linear trend with applied pressure, only deviating above 5 GPa, where the slope became nearly zero. The thermal conductivity was found to increase linearly with pressure until the region of the phase transition, where the trend plateaued and decreased slightly before a rapid upturn. All of this evidence supports previous claims, by Chattopadhyay *et al.* [8], that the first high pressure phase of this material is metallic.

For GaTe, there is evidence, as with Bi_2Te_3 and Sb_2Te_3, of an anomaly in some of the equations of state associated with topological transitions. This was found to occur at nearly 1 GPa. The resistivity showed a rather rapid drop with applied pressure, similar to InTe, and a corresponding drop at 3 GPa. The Seebeck coefficient exhibited an initial plateau with pressure until the previously mentioned anomaly, when the trend became linear and downward until 8 GPa, where it levelled out. The thermal conductivity was found to linearly increase, with the slope changing slightly at the transition to the mixed phase at 8 GPa, where the slope increased. This evidence would support a similar claim to that made for InTe, with the high pressure mixed phase exhibiting metallic tendencies. This is especially pronounced in the electronic thermal conductivity with the increase by a factor of nearly 35 upon transition to the mixed phase.

Finally, the results for $InGaTe_2$ exhibit some of the most interesting information. The anomaly present in GaTe was found to be present in this material also. This occurance appeared at approximately 1.5 GPa, only slightly higher than GaTe. This correlated well with the Seebeck coefficient results, which show a slight decrease until the 2 GPa data point, where the trend shows a rapid decrease in this parameter. The resistivity also shows this dramatic decrease in the electrical resistance with pressure. The thermal conductivity, on the other hand, shows no evidence of the phase transitions present in this material, with the increasing trend being almost completely linear. In contrast with this, the converted electronic thermal

conductivity shows a marked decrease occuring at the phase transition pressure, in addition to a large increase in the contribution from electrons/holes. This, again, suggests a trend towards metallicity, but the first high pressure phase appears to still remain as a semiconductor. In addition to this, $InGaTe_2$ was found to be the only material that exhibited a Seebeck coefficient that changed sign with pressure, suggesting a change in the Fermi surface of the material. In addition to the information presented so far, it was found that the lattice component of the thermal conductivity for all of these samples followed a trend roughly similar to that theorized by Hofmeister and others [22].

Despite these interesting changes, it was found that the application of pressure did not significantly improve the performance of any of these materials. Although pressure has demonstrated that the high pressure forms of these materials are not effective as thermoelectrics on their own, the information gained from this study may help to further understand the fundamental parameters of these material. As such, further measurements are planned on materials that are reported to be effective thermoelectric materials under ambient conditions, doped versions of these materials and others, and improvement of the measurement capabilities of this system, along with inclusion of new measured quantities. From this, it may be possible in the future to learn enough about these and other materials to improve the current theories and assist in the prediction of the properties of materials as of yet unstudied.

REFERENCES

[1] N. Davies, Prospects for energy savings in heating system components, Technical report, Boiler Savelec, 2005.

[2] J. Ziman, *Electrons and Phonons: The Theory of Transport Phenomena in Soids*, Oxford at the Clarendon Press, 1967.

[3] N. Gorbachuk, A. Bolgar, V. Sidorko, and L. Goncharuk, Powder Metallurgy and Metal Ceramics **43** (2004).

[4] J. Fleurial, L. Gailliard, R. Triboulet, H. Scherrer, and S. Scherrer, Journal of the Physics and Chemistry of Solids **49** (1988).

[5] P. Zhu et al., Journal of Alloys and Compounds **420** (2006).

[6] J. Navratil, P. Lostak, and J. Horak, Crystal Research and Technology **26** (1991).

[7] V. Kulbachinskii, V. Kytin, and P. Tarasov, Journal of Experimental and Theoretical Physics **110**, 4 (2010).

[8] T. Chattopadhyay, R. Santandrea, and H. v. Schnering, Journal of Physics and Chemistry of Solids **46** (1985).

[9] T. Harman, P. Taylor, M. Walsh, and B. LaForge, Science **297** (2002).

[10] G. Wang and T. Cagin, Physical Review B **76**, 075201 (2007).

[11] A. Garg et al., Journal of Physics: Condensed Matter **14** (2002).

[12] P. Larson, Physical Review B **68** (2003).

[13] B. Chen, C. Uher, L. Iordanidis, and M. Kanatzidis, Chemistry of Materials **9** (1997).

[14] D.-Y. Chung et al., Journal of the American Chemical Society **126** (2004).

[15] V. Shchennikov and S. Ovsyannikov, Physica Status Solidi B **244** (2007).

[16] C. Kittel, *Introduction to Solid State Physics*, John Wiley and Sons, 1996.

[17] N. Ashcroft and J. Mermin, *Solid State Physics*, Holt, Reinhart, and Winston, 1976.

[18] G. Nolas, J. Sharp, and H. Goldsmid, *Thermoelectrics: Basic Principles and New Materials Developments*, Springer Verlag, 2001.

[19] D. Rowe, *CRC Handbook of Thermoelectric Materials*, CRC Press, 1995.

[20] T. Tritt, *Thermal Conductivity: Theory, Properties, and Applications*, Klewer Academic/Plenum Publishing, 2004.

[21] A. Lawson, *Effect of Hydrostatic Pressure on Resistivity of Metals*, Progress in Metal Physics, Interscience Publishers, Inc., 1955.

[22] A. Hofmeister, Proceedings of the National Academy of Sciences **104**, 6 (2007).

[23] M. Roufosse and P. Klemens, Physical Review B **7**, 8 (1973).

[24] J. Dugdale and D. Gugan, Proceedings of the Royal Society of London. Series A, Mathematical and Physical Sciences **241** (1957).

[25] A. Hofmeister and H. Mao, Proceedings of the National Academy of Sciences **99**, 559 (2002).

[26] J. Kamal and D. Tewari, Physica Status Solidi A **2** (1970).

[27] B. Suleiman, S. Gustafsson, and A. Lunden, International Journal of Thermophysics **18**, 11 (1997).

[28] D. Novikov, M. Katsnelson, J. Yu, A. Postnikov, and A. Freeman, Physical Review B **54** (1996).

[29] N. C. Shekar, D. Polvani, J. Meng, and J. Badding, Physica B **358** (2005).

[30] P. Larson, Physical Review B **74** (2006).

[31] K. Kurosaki et al., Applied Physics Letters **93** (2008).

[32] M. Data, Jade : Xrd pattern processing, identification, and quantification, 2006.

[33] H. Mao, J. Xu, and P. Bell, Journal of Geophysical Research **91** (1986).

[34] A. Hammersley, Fit2d: Image plate conversion software, 2005.

[35] D. Dunstan, Review of Scientific Instruments **60** (1989).

[36] D. Kuhlmann-Wilsdorf, B. Cai, and R. Nelson, Journal of Materials Research **6** (1991).

[37] M. Yousuf and K. Rajan, Pramana **18** (1982).

[38] V. Bean et al., Physica **139** (1986).

[39] D. McWhan, P. Montgomery, H. Stromberg, and G. Jura, Journal of Physics and Chemistry **67** (1963).

[40] G. Peggs, *High Pressure Measurement Techniques*, Applied Science Publishers, 1983.

[41] D. Polvani, J. Meng, M. Hasegawa, and J. Badding, Review of Scientific Instruments **70** (1999).

[42] R. Bentley, *Theory and Practice of Thermoelectric Thermometry*, volume 3, Springer-Verlag, 1998.

[43] T. P. Wang, C. D. Starr, and N. Brown, Acta Metallurgica **14**, 649 (1966).

[44] F. Bundy, Journal of Applied Physics **32** (1961).

[45] P. Jacobsson and B. Sundqvist, International Journal of Thermophysics **9** (1988).

[46] M. Osako and E. Ito, Simultaneous thermal diffusivity and thermal conductivity measurements of mantle materials up to 10 gpa, Technical report, Okayama University, 1997.

[47] F. Pu, Physics Letters A **157**, 151 (1991).

[48] B. Sundqvist, Physical Review B **38**, 12283 (1988).

[49] R. G. Ross, P. Andersson, B. Sundqvist, and G. Backstrom, Reports on Progress in Physics **47**, 1347 (1984).

[50] N. V. Chandra Shekar, J. F. Meng, D. A. Polvani, and J. V. Badding, Solid State Communications **116**, 443 (2000).

[51] J. Bandyopadhyay and K. P. Gupta, Cryogenics **17**, 345 (1977).

[52] R. W. Powell, R. P. Tye, and M. J. Hickman, International Journal of Heat and Mass Transfer **8**, 679 (1965).

[53] Heat capacity application note 1085-152 : Non-smooth specific heat between 200 k and 300 k due to anomalous specific heat of apiezon n-grease, Technical report, Quantum Design, 2002.

[54] K. Taylor, British Journal of Applied Physics **12** (1961).

[55] Y. Feutelais, B. Legendre, N. Rodier, and V. Agafonov, Materials Research Bulletin **28** (1993).

[56] M. Francombe, British Journal of Applied Physics **9** (1958).

[57] S. Nakajima, Journal of Physics and Chemistry of Solids **24**, 479 (1963).

[58] L. Vereshchagin, E. Atabaeva, and N. Bendeliani, Soviet Physics-Solid State **13** (1972).

[59] L. Khvostantsev, A. Orlov, N. Abrikosow, T. Svechnikova, and S. Chizhevskaya, Physics of Statistical Solids A **71** (1982).

[60] L. Khvostantsev, A. Orlov, N. Abrikosov, and L. Ivanova, Physica Status Solidi A **89** (1985).

[61] A. Nakayama et al., High Pressure Research **29**, 5 (2009).

[62] E. Itskevich, L. Kashirskaya, and V. Kraidenov, Semiconductors **31** (1997).

[63] S. Ovsyannikov and V. Shchennikov, Chemistry of Materials **22**, 12 (2010).

[64] Y. Zhao, J. Dyck, B. Hernandez, and C. Burdn, Journal of Physics and Chemistry C **114**, 7 (2010).

[65] S. Ovsyannikov et al., Journal of Applied Physics **104**, 5 (2008).

[66] M. Einaga et al., Journal of Physics: Conference Series **215**, 5 (2010).

[67] H. Goldsmid, Proceedings of the Physical Society **69**, 203 (1956).

[68] R. Venkatasubramanian, E. Siivola, T. Colpitts, and B. O'Quinn, Nature **413** (2001).

[69] N. Sakai, T. Kajiwara, K. Takemura, S. Minomura, and Y. Fujii, Solid State Communications **40** (1981).

[70] M. Bartkowiak and G. Mahan, Procedings of the 18^{th} International Conference on Thermoelectrics , 713 (1999).

[71] M. Ibrahim, M. Wakkad, E. Shokr, and H. A. El-Ghani, Applied Physics A **52**, 5 (1991).

[72] R. Ismaiylova, I. Bakhtiyraly, and D. S. Abdinov, Inorganic Materials **45**, 4 (2009).

[73] C. Desai and S. Dhar, Philosophical Magazine Letters **80**, 6 (2000).

[74] H.-W. Jeon, H.-P. Ha, D.-B. Hyun, and J.-D. Shim, Journal of Physics and Chemistry of Solids **52**, 579 (1991).

[75] G. J. Cosgrove, J. P. McHugh, and W. A. Tiller, Journal of Applied Physics **32**, 621 (1961).

[76] O. Madelung, U. Rossler, and M. Schulz, *Gallium Telluride: Crystal Structure, Lattice Parameters, and Thermal Expansion*, volume 41C of *Landolt-Bornstein - Group III Condensed Matter*, Springer-Verlag, 1998.

[77] O. Madelung, U. Rssler, and M. Schulz, *Indium Telluride: Crystal Structure, Lattice Parameters, and Thermal Expansion*, volume 41C of *Landolt-Bornstein - Group III Condensed Matter*, Springer-Verlag, 1998.

[78] M. Parlak, C. Ercelebi, I. Gunal, H. Ozkan, and N. M. Gasanly, Crystal Research and Technology **31**, 673 (1996).

[79] D. P. Spitzer, Journal of Physics and Chemistry of Solids **31**, 19 (1970).

[80] G. D. Guseinov, A. I. Rasulov, E. M. Kerimova, and M. Z. Ismailov, Physica Status Solidi **19**, K7 (1967).

[81] A. Aydinli, N. Gasanly, A. Uka, and H. Efeoglu, Crystal Research and Technology **37**, 1303 (2002).

[82] U. Schwarz, K. Syassen, and R. Kniep, Journal of Alloys and Compounds **224**, 212 (1995).

[83] A. Al-Ghamdi, Journal of Thermal Analysis and Calorimetry **94**, 597 (2008).

[84] A. Mancini, C. Manfredotti, A. Rizzo, and G. Micocci, Journal of Crystal Growth **21** (1974).

[85] C. Manfredotti, R. Murri, A. Rizzo, L. Vasanelli, and G. Micocci, Physica Status Solidi A **29** (1975).

[86] W. Milne and J. Anderson, Journal of Physics D: Applied Physics **6** (1973).

[87] H. Deiseroth, D. Muller, and H. Hahn, Zeitschrift fur anorganische und allgemeine Chemie **525**, 163 (1985).

[88] E. Gojaev, K. Gyulmamedov, A. Ibragimova, and A. Movsumov, Inorganic Materials **46**, 353 (2010).

[89] G. D. Guseinov et al., Physics Letters A **33**, 421 (1970).

VITA

Graduate College
University of Nevada, Las Vegas

Matthew K. Jacobsen

Degrees:
Bachelor of Science, Physics, 2004
Oregon State University

Masters of Science, Physics, 2007
University of Nevada, Las Vegas

Publications:

Jacobsen, M.K., Kumar, R.S., Cao, G., Neumeier, J.J., and Cornelius, A.L. *High pressure structural studies on $SrRuO_3$*. Journal of Physics and Chemistry of Solids **69**, 2237 (2008).

Cornelius, A.L., Kumar, R.S., **Jacobsen, M.K.**, Bauer, E.D., Sarrao, S., and Fisk, Z. *Magnetic oredering in UCu_2Si_2 at high pressure*. Physica B-Condensed Matter **403**, 940 (2008).

Jacobsen, M.K., Kumar, R.S., Cornelius, A.L., Sinogeiken, S.V., and Nicol, M.F. *High pressure X-ray diffraction studies of $Bi_{2-x}Sb_xTe_3$ ($x = 0, 1, 2$)*. AIP Conference Procedings **955**, 171 (2007).

Hamlin, J.J., Deemyad, S., Schilling, J.S., **Jacobsen, M.K.**, Kumar, R.S., Cornelius, A.L., Cao, G., and Neumeier, J.J. *AC Susceptibility studies of the weak itinerant ferromagnet $SrRuO_3$*. Physical Review B **76**, 014432 (2007).

Dissertation Title: Measurement System for High Pressure Characterizations of Materials

Dissertation Committee:
Committee Chairperson: Andrew Cornelius, Ph.D.
Committee Member: Lon Spight, Ph.D.
Committee Member: Tao Pang, Ph.D.
Graduate Faculty Representative: Clemens Heske, Dr. rer. nat.